Rechargeable Magnesium/Oxygen Batteries:

Reaction Mechanisms and Their Dependence on Electrolyte Composition

by

Gulin Vardar

A dissertation submitted in partial fulfillment

of the requirements for the degree of

Doctor of Philosophy

(Materials Science and Engineering)

in the University of Michigan

2016

Doctoral Committee:

Associate Professor Donald J. Siegel, Co-chair

Associate Professor Charles W. Monroe, Co-chair

Associate Professor Bart M. Bartlett

Associate Professor Pierre F. P. Poudeu

Associate Professor Jeff S. Sakamoto

Acknowledgements

I would like to sincerely thank Professor Charles Monroe and Professor Donald Siegel for allowing me to work on this exciting project. Dr. Alice Sleightholme has been a great mentor and I am very grateful to her advice on experimental electrochemistry.

Our collaboration on electrolytes with Dr. Emily Nelson and Prof. Bart Bartlett was integral to the progress of this research and I want to truly thank Emily for always being so accommodating and friendly.

I would like to thank Dr. Hidehiko Hiramatsu and Junichi Naruse from DENSO Japan for their kindness and their efforts in making sure my internship on Mg/O_2 batteries in Japan was a success and a pleasure.

I would like to express my gratitude to the Monroe research group and Siegel research group for helping me with experiments and being such good friends.

Dr. Haiping Sun and Dr. Kai Sun from the Michigan Center for Materials Characterization have tirelessly trained me on many characterization instruments. Dr. Jerry (Zhongrui) Li from Central Campus Electron Microbeam Analysis Laboratory has been extremely helpful with Auger electron spectroscopy measurements. Zi Li in the Chemistry Department has been of tremendous help in collecting Raman spectroscopy measurements. Dr. Travis Thompson from the Mechanical Engineering Department has mentored the instrumentation and analysis for the electrochemical impedance spectroscopy measurements and I am grateful for his advice.

Table of Contents

List of Tables

List of Abbreviations

ACN	acetonitrile
BF_4	tetrafluoroborate
BH_4	borohydride
BMIM	(1-butyl,3-methyl)imidazoleum
CV	cyclic voltammogram
DEME	N,N-diethyl-N-methyl(2-methoxyethyl)-ammonium
DME	dimethoxyethane
EtMgCl	ethyl magnesium chloride
FSI	bis(fluorosulfonyl)imide
MeMgBr	methyl magnesium bromide
Tf_2N	bis(trifluoromethanesulfonyl)imide
TfO	trifluoromethanesulfonate
THF	tetrahydrofuran
PP13	N-methyl-N-propylpiperidinium

Abstract

Rechargeable Magnesium/Oxygen Batteries:
Reaction Mechanisms and Their Dependence on Electrolyte Composition

Chairs: Donald J. Siegel and Charles W. Monroe

Electrochemical energy storage devices that are robust, energy-dense, and cheap will accelerate the commercialization of electric vehicles. Magnesium/oxygen (Mg/O_2) batteries are a promising system with the potential for very high energy densities. Furthermore, a rechargeable Mg/O_2 battery could be a cheaper and potentially safer alternative to the lithium (Li)-ion batteries currently in use. The goal of this thesis is to explore candidate magnesium electrolytes for use in Mg/O_2 batteries, and to assess the reaction mechanisms and performance of Mg/O_2 cells that employ these electrolytes.

We first consider electrolytes based on ionic liquids (ILs), which are attractive electrolytes for batteries because they are nonflammable and nonvolatile. The electrochemistry of Mg salts in room-temperature ionic liquids (ILs) was studied using plating/stripping

voltammetry. Borohydride (BH_4^-), trifluoromethane-sulfonate (TfO^-), and bis(trifluoromethane-sulfonyl)imide (Tf_2N^-) salts of Mg were investigated. Three ILs were considered: l-n-butyl-3-methylimidazolium (BMIM)-Tf_2N, n-methyl-n-propylpiperidinium (PP13)-Tf_2N, and n,n-diethyl-n-methyl(2-methoxyethyl)-ammonium ($DEME^+$) tetrafluoroborate (BF_4^-). Salts and ILs were combined to produce binary solutions in which the anions werestructurally similar or identical, if possible. Contrary to some prior reports, no salt/IL combination appeared to facilitate reversible Mg plating. In solutions containing $BMIM^+$, oxidative activity near 0.8 V vs Mg/Mg^{2+} is likely associated with the BMIM cation, rather than Mg stripping. The absence of voltammetric signatures of Mg plating from ILs with Tf_2N^- and BF_4^- suggests that strong Mg/anion Coulombic attraction inhibits electrodeposition. Cosolvent additions to $Mg(Tf_2N)_2$/PP13-Tf_2N were explored but did not result in enhanced plating/stripping activity. The results highlight the need for IL solvents or cosolvent systems that promote Mg^{2+} dissociation.

We next describe a room-temperature, non-aqueous, reversible Mg/O_2 cell using a modified Grignard electrolyte. Although the cell exhibits low capacity, its discharge product is a faceted, transparent solid that can be recharged with fair efficiency. Electrochemical, microscopic, and spectroscopic analyses reveal characteristics that distinguish Mg/O_2 chemistry from its alkali-metal/O_2 analogues. The open-circuit voltage is 2.0 V, lower than the ~2.9 V expected for direct electrochemical formation of MgO_x. Discharge generates a mixed phase primarily comprising crystalline MgO, with a substantial minority of amorphous MgO_2. The low voltage and two-phase product are consistent with a multi-step discharge reaction in which a superoxide-ion (O_2^-) intermediate forms at ~2 V vs. Mg/Mg^{2+}. Chemical precipitation and disproportionation subsequently produce MgO_2 and MgO, but do not contribute to the cell's electrical energy output. During charging, MgO_2 decomposes preferentially. Bypassing the multi-

step mechanism in favor of direct electrochemical MgO_x formation would raise the discharge potential and, consequently, the energy density.

The performance of the preceding modified-Grignard-based cell is then compared with one based on an all-inorganic magnesium aluminum chloride complex (MACC) electrolyte. The precursor MACC solution is conditioned using choronoamperometry, a method which is shown to be capable of quickly conditioning large quantities of electrolyte. Mg/O_2 cells based on the MACC electrolyte exhibited higher discharge capacities than those based on the modified Grignard electrolyte. The discharge product of the former system was found to be an inhomogeneous mixture of $MgCl_2$ and $Mg(ClO_4)_2$. However, rechargeability was limited. Electrochemical impedance spectroscopy measurements were used to identify that film formation on the Mg anode is main source of impedance in Mg/O_2 cells.

This research shows that the performance of Mg-based batteries is highly sensitive to the type of electrolyte used. For example, our results demonstrate that Mg electrolytes containing Tf_2N^- and BF_4^- anions do not promote reversible Mg electrochemistry due to the lack of dissociation between the Mg^{2+} cation and the anions. Moreover, the different behavior of Mg/O_2 cells based on either a modified Grignard or MACC electrolyte can be related to evolution of Mg/electrolyte interface in the presence of O_2 and the electrolyte's conductivity. For future work, it would be useful to develop halogen-free electrolytes to produce discharge products free of halogens which are chemically stable in the presence of O_2.

Chapter 1 Introduction

1.1 Batteries for Transportation

Transportation currently accounts for a third of US annual primary energy consumption and greenhouse gas emissions.[1] One of the main strategies to reduce greenhouse gas (GHG) emissions is to improve vehicle fuel efficiency by using advanced technologies such as hybrid vehicles and electric vehicles.[2] Even when the GHG emissions associated with electricity production are taken into account, a plug-in hybrid vehicle can emit 50% less GHGs than a standard gasoline-powered vehicle.[3] Widespread electrification of vehicles could help the transportation sector meet, and possibly exceed, the near-future carbon emissions standards.[4-5]

Figure 1.1 shows the projected market share for new vehicle sales for conventional (gasoline-powered), hybrid (gasoline-powered with electric motor on board) and plug-in hybrid (allowing for extended, all-electric diriving range) vehicles.[6] The market share for plug-in hybrid vehicles is projected to grow significantly in the next decade. As the demand for plug-in hybrid vehicles grows, it is anticipated that battery technologies will come under increasing pressure to improve reliability, energy density and cost.
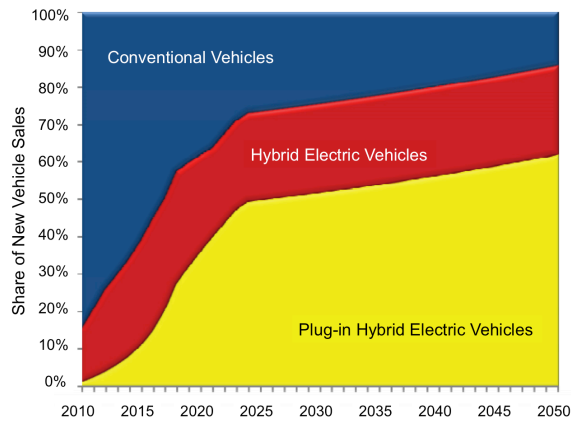
Figure 1.1 Projected new car market share for medium PHEV penetration scenario (as outlined in Electric Power Research Institute's report)[6] for conventional vehicles, hybrid electric vehicles and plug-in hybrid electric vehicles.

1.2 Beyond Li-ion technologies

As part of the "EV Everywhere" challenge, the Department of Energy has set aggressive targets for battery energy density.[5] Currently, volumetric and gravimetric energy densities for the batteries used in electric cars are in the range of 80-100 Wh/kg and 200 Wh/L. These are approaching the highest theoretical energy densities for Li-ion chemistries (567 Wh/kg and 1901Wh/L). The Department of Energy's target for volumetric and gravimetric energy densities for electric car batteries are 250 Wh/kg and 400 Wh/L, respectively.[5] In order to reach these target energy densities, other battery chemistries with higher theoretical energy densities need to be explored.

Currently, most hybrid and electrified vehicles use Li-ion batteries. These batteries suffer from high cost, modest energy density, limited cycle life, and the use of flammable and volatile electrolytes.[7] Li-ion batteries operate by shuttling Li ions between two intercalation electrodes, typically comprising a carbon-based anode, and a transition metal-oxide cathode. In contrast, so-

called "beyond-Li-ion" batteries have the capability to deliver gravimetric and volumetric energy densities that vastly exceed Li-ion batteries.[8] Electric vehicles using higher-energy-density batteries could have longer vehicle ranges, which would make these vehicles more attractive to consumers and potentially minimize GHG emissions.[9]
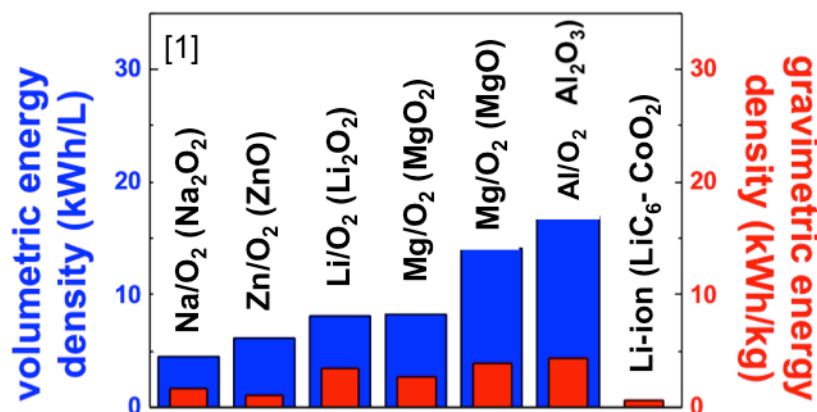
Figure 1.2 Theoretical volumetric and gravimetric energy densities for metal/O_2 and Li-ion battery chemistries. For metal/O_2 chemistries, the compound in paranthesis indicates the discharge product.[10]

Among the "beyond-Li-ion" candidates, metal/O_2 (or "metal-air") batteries offer some of the highest theoretical volumetric and gravimetric energy densities, which are compared to a typical Li-ion chemistry in Figure 1.2.[11] Metal/O_2 batteries utilize the electrochemical reaction between a metal such as lithium, sodium or zinc and a strong gaseous oxidizer (oxygen). Although non-reversible chemistries such as zinc/air were commercialized in the 1990s,[12] recent years have seen a renewed interest in developing rechargeable metal/O_2 batteries with alkali-metal (Li, Na, K, *etc*.) and alkali-earth-metal (Mg, Ca, *etc*.) anodes. These chemistries offer

extremely high theoretical energy densities, coupled with the possibility for reversiblility. Multivalent alkali-earth-metal anodes have the additional advantage of contributing two electrons per metal ion, potentially yielding even higher gravimetric energy densities. For example, the gravimetric energy density for a Mg/O_2 battery, 3.9 kWh/kg, can theoretically out-perform that of a Li/O_2 battery, 3.4 kWh/kg.

In addition to higher energy densities, magnesium also has advantages related to safety, cost, and environment impact. Catastrophic failures of Li-ion batteries often owe to Li dendrite formation and/or the combustion of flammable solvents. The Mg electrode is reportedly less prone to dendrite formation.[13] The possibility of using non-flammable solvents in Mg batteries is explored in Chapter 2. Regarding cost, as of December 2015, the cost for magnesium metal was $1.99/kg, whereas lithium metal costs $200/kg.[14] These prices reflect the higher abundance of magnesium versus lithium. Furthermore, the prevalence of magnesium as a structural material has resulted in the creation of a magnesium recycling technologies. The potential to recycle magnesium will reduce the environmental impact of magnesium use in batteries.

Metal/air batteries consist of a metal negative electrode (an anode during disharge) and a gas-breathing positive electrode (cathode) with either an aqueous or nonqueous electrolyte.[11, 15] There are several examples of metal-air chemistries where the reactant (O_2) is harvested from air, such as zinc/air.[16-17] However, metal/air batteries that use air as the O_2 source are generally not electrochemically reversible due to degradatory effects of the water vapor, carbon dioxide, or nitrogen in typical air. Very recent advances in Li/O_2 techonology do suggest that controlled amounts of water in the electrolyte may enhance battery performance, which could open the way to use air instead of pure O_2 in metal/O_2 batteries,[18] but this is a topic of some dispute. For metal/air batteries, replacement of a degraded metal anode with a fresh metal anode is the only option for extended battery use (in combination with a scheme to regenerate spent anodes with

an external thermochemical process, this could be called 'mechanical recharging').[19-20] Alternatively, the electrolyte in contact with the Mg anode could be water-based (as in the aqueous Mg/air battery).[21-22] In the case of aqueous Mg/air batteries, the Mg anode surface corrodes as the discharge reaction progresses and the Mg anode also needs to be mechanically recharged.[19, 23]

The term 'metal/air' is sometimes casually used to refer to metal/O_2 batteries, in which the gas feed is a pure O_2 source free of water vapor or nitrogen. Metal/O_2 batteries that use non-aqueous electrolytes have the most potential to be electrochemically rechargeable and therefore this thesis focuses on non-aqueous Mg/O_2 technology instead of aqueous.

1.3 Mg electrolytes

Electrolytes for Li-ion batteries have been the focus of intense research for the last two decades due of the large impact of electrolytes on battery performance.[24] Li-ion battery electrolytes usually consists of a mixture of non-aqueous organic solvents (for example, 60:40 propylene carbone:ethylene carbonate) and a simple Li salt such as $LiPF_6$ or $LiTf_2N$. Ratios of organic solvents, additives, Li salt concentration have been optimized to achieve better battery performance.[24] Interestingly, for Mg, electrolytes that consist of a non-aqueous organic solvent and a simple Mg salt do not appear to promote reversible electrochemistry.[25] Therefore, new strategies are needed for electrolytes that are capable of reversible plating and stripping on Mg negative electrodes, and which allow for reversible insertion/extraction from positive electrode intercalation hosts.

The first report of reversible Mg deposition and dissolution from non-aqueous solvents was published in a paper by Gregory *et al*. in 1990.[26] In this paper, a number of organic Mg salts

that resemble Grignard reagents were characterized in terms of conductivity and electrodeposition of pure Mg from these electrolytes were demonstrated. Grignard reagents have the formula RMgX, where R is alkyl or aryl group and X is a halogen. Furthermore, cycling of a cell containing a Mg metal anode with an intercalation cathode (Co_3O_4) was reported. The degree of ionicity in the Mg electrolyte was reported to control the efficiency of Mg electrodeposition.

After Gregory's discovery of a working Mg-ion cell, there was increased interest in identifying improved electrolytes and cathode materials that allow for higher cell voltages and longer-term cyclability.[27-31] Research in the late 1990s converged on Grignard reagents in organic solvents as candidates for high-efficiency Mg-ion batteries. Aurbach *et al*. and Liebenow *et al*. concurrently reported that Grignard reagents dissolved in THF achieved <99% coulombic efficiency on noble metal electrodes.[25, 31-32] Subsequent electrolyte studies revealed that addition of Lewis acids to Grignard reagents in organic solvents increase the electrolyte's oxidative stability significantly.[33-38] In addition, the compatibility of the organohaloaluminate (Grignard reagents reacted with Lewis acids containing Al) electrolytes with a Chevrel-phase cathode (Mo_3S_4) was demonstrated over 600 cycles.[33] Several compositions of the organohaloaluminate electrolyte were subsequently studied; the reaction of PhMgCl and $AlCl_3$ was found to produce the highest coulombic efficiency and oxidative stability.[39-40] Different compositions of organohaloaluminate electrolytes were studied by several researcher groups and found to be robust systems for reversible Mg deposition.[41-42]

Unfortunately, the oxidative stability of the Mg^{2+} electrolytes discussed so far was not suitable for use with high-voltage cathodes. Consequently, several reports focused on improving the oxidative stability of the organohaloaluminate electrolytes. It was reported that reacting HMDSMgCl with $AlCl_3$ produced an electrolyte that has an oxidative stability higher than 3V vs. Mg/Mg^{2+}.[43-44] Furthermore, a solid Mg anode was parired with with a sulphur cathode to

demonstrate a Mg/S battery based on the HMDSMgCl:AlCl$_3$ electrolyte.[43] Other researchers

focused on replacing the AlCl$_3$ with boron-based species to achieve oxidative stabilities as high

as 3.5 V vs. Mg/Mg^{2+}.[45-47] Borohydride-based electrolytes are also another interesting class of

electrolytes due to the lack of halides that can cause corrosion.[48-49] Iterations on the borohydride-

based electrolytes have enabled oxidative stabilities that are as high as 3V vs. Mg/Mg^{2+}.[50]

Modification of the ligands of Grignard reagents can also have important effects on the

properties of the electrolyte. A series of R-Mg-Cl salts with ligands including 4-methoxy-

phenolate (MPMC), phenolate (PMC), 4-methyl-phenolate (MePMC), 4-tert-butyl-phenolate

(BPMC), 4-(trifluoromethyl)-phenolate (FMPMC), pentafluorophenolate (PFPMC) were

synthesized.[51] Modified ligands such as the (FMPMC)$_2$-AlCl$_3$/THF and (PFPMC)$_2$-AlCl$_3$/THF

solutions were reported to exhibit oxiditave stabilities at least 400mV above the previously

published phenolate electrolytes.[51] A similar approach by Wang *et al*. has produced electrolytes

that are reported to be stable with air such as 2-tert-butyl-4-methyl-phenolate magnesium

chloride (BMPMC)-AlCl$_3$/THF.[52]

Nelson *et al*. has reported a modified Grignard electrolyte consisting of PhMgCl reacting

with Al(OPh)$_3$ in THF.[53] The oxidative stability of this electrolyte surpassed all other reported

cases (> 4 V vs. Mg/Mg^{2+}) and the coulombic efficiency for Mg deposition was >99%. This

electrolyte was used in the Mg/O$_2$ battery experiments reported in Chapter III.

1.4 Non-aqueous Mg/O$_2$ batteries

Non-aqueous Mg/O$_2$ batteries are a relatively recent addition to the metal/O$_2$ battery

research field. The first report of a non-aqueous Mg/O$_2$ battery was published in 2013,[54] and

used a Mg metal anode. The electrolytic solution consisted of Mg(ClO$_4$)$_2$ salt and DMSO

solvent. The cathode was carbon sandwiched between platinum mesh grids. The battery was found to be rechargeable only through the addition of a redox mediator (iodine) to the electrolyte; a gravimetric capacity of 2131 mAh/$g_{cathode}$ was reported for the first cycle. The experiments were performed at an elevated temperature of 60°C.

Another report on non-aqueous Mg/O_2 batteries was conducted by Toyota Central Research & Development Laboratories.[55] In that study an anion complex such as TEMPO was shown to facilitate chemical decomposition of the presumed MgO discahrge product at an elevated temperature of 60°C. A radical polymer called PTMA was synthesized by the radical polymerization of 2,2,6,6-tetramethylpiperidine methacrylate monomer with 2,2'-azobisisobutyronitrile, followed by oxidation with 3-chloroperoxybenzoic acid. The inclusion of PTMA in the carbon cathode along with the TEMPO anion on the electrolyte enabled a rechargeable Mg/O_2 cell (using an ionic liquid electrolyte) with a gravimetric capacity of 737 mAh/$g_{cathode}$ for the first cycle.

In these studies the discharge and recharge process relied upon the presense of a redox mediator such as iodine or the TEMPO anion complex. It was also assumed that the discharge product was MgO, although little evidence to support the presence of MgO as the sole discharge product was presented. Furthermore, the chemistry of the discharge product can be dependent on the chemistry of the electrolyte and additives in the electrolyte[18] and therefore should be characterized for each type of electrolyte.

The preceding discussion suggests that a metal/O_2 battery based on a Mg anode could offer a very attractive alternative to current electrochemical energy storage technologies. This disseration explores in detail the prospects for rechargeable Mg/O_2 batteries by characterizing the performance and properties of this chemistry with several experimental techniques. This investigation begins in Chapter II, where we report on the electrochemistry of magnesium salts

in ionic liquids as candidates for secondary Mg batteries. In Chapter III a rechargeable, room-temperature Mg/O_2 battery using a modified Grignard electrolyte is reported, along with a detailed description of the discharge and recharge pathways. In contrast, in Chapter IV, an alternative, all-inorganic electrolyte was used in the same Mg/O_2 cells. Limitations on rechargeability were explored for this system based on impedence measurements. Finally, in Chapter V, we briefly discuss potential future work that could be undertaken to improve the performance of Mg/O_2 batteries.

Chapter 2 Electrochemistry of Magnesium Electrolytes in Ionic Liquids for Secondary

Batteries

2.1 Introduction

ILs are ideal candidates for electrolytes in battery applications due to their low flammability and volatility.[56-59] ILs are ionic compounds that are liquid at room temperature and therefore have high ionic conductivity (~10mS/cm).[58] They also exhibit high thermal stability and wide electrochemical windows.[60] The drawbacks for ILs are their relatively high viscosity[58] and higher cost compared to organic solvents.[61]

ILs have been studied for Li-ion applications[62-63] and Li metal can be reversibly deposited with high coulombic efficiency using $Li(Tf_2N)$ in $PP13$-Tf_2N[64]. High energy density systems such as Li/O_2 and Li/S have also been explored with IL electrolytes.[65-68] However, the research into using ILs as solvents for Mg-based electrochemistry has been limited and there are problems with reproducibility reported in literature.

First mention of reversible deposition and dissolution of Mg in ionic liquids was reported with 1M $Mg(TfO)_2$ in $BMIM$-BF_4.[69-71] Then, another IL ($PP13$-Tf_2N) with 1M $Mg(TfO)_2$ was also reported to enable reversible Mg deposition dissolution.[72] Finally, a mixture of these two ILs ($PP13$-Tf_2N and $BMIM$-BF_4) was used to cycle a symmetric Mg/Mg cell for over 200 cycles.[73] A

year later, Amir *et al.* reported that they were not able to reproduce the reversible Mg deposition with $Mg(TfO)_2$ in BMIM-BF_4.[74] Cheek *et al.* also published a study with several combinations of Mg salts and ILs and reported no reversible Mg deposition at room temperature.[75] Interestingly, it was found that Mg co-deposition was possible in a mixture of $Mg(Tf_2N)_2$ and $LiTf_2N$ in DEME-Tf_2N but not in $Mg(Tf_2N)_2$ only in the same IL.[76]

In a seminal paper, Gregory *et al.* showed that one can electrodeposit Mg reversibly from solutions of Grignard reagents, and suggested that the low partial charge on Mg in the Grignard molecule facilitates desolvation of Mg at the interface where plating occurs.[26] Moreover, it was postulated that simple salts in which the Mg ion has a high charge density (*e.g.*, highly ionic compounds such as $MgCl_2$ or $Mg(ClO_4)_2$) are less likely to promote Mg plating due to the strong coulombic attraction between ions in the formula unit, which prevents dissociation in solution to produce solvated mobile Mg^{2+}.[26] Addition of Al-based Lewis acids to Grignard reagents has resulted in improved oxidative stability, while maintaining highly reversible Mg plating, which will be discussed in Chapter 3.[25-26, 36, 40] Addition of Lewis acids promotes the formation of ionic Mg-containing Grignard-complexes that dissociate readily, increasing ionic conductivity while maintaining a low partial charge on Mg in the complex cation.[40, 77] Recently, solutions of simple Mg salts combined with Al-based Lewis acids were shown to reversibly deposit and dissolve Mg, which will be discussed in Chapter 4.[44, 78] Strong Lewis acids enable Mg dissociation when added to Mg-salt solutions due to their strong electron-withdrawing nature, which presumably overcomes the coulomb force that prevents the dissociation of anions from Mg^{2+}.[78]

Therefore, another approach to using ILs as solvents for Mg batteries has been to use Grignard reagents dissolved in THF as the Mg source in the electrolyte. For example, EtMgCl dissolved in THF was added to the IL (DEME-Tf_2N) and reversible Mg deposition was observed.[79] Additionally, a binary IL system that contains DEME-Tf_2N and DEME-FSI was

examined and, using MeMgBr/THF as the Mg source, was able to achieve 90% coulombic efficiency.[80] Optimization of the cation structure of ILs was also reported to improve the deposition characteristics with MeMgBr/THF.[81] However, the presence of THF, an organic solvent with high flammability and volatility, still makes these mixed electrolytes susceptible to safery risks. Same can be said for adding ACN and DME to IL solvents to facilitate Mg deposition.[82]

In this chapter, we have explored the effects of IL anion and cation on Mg electrochemistry in ILs in a systematic study.

2.2 Experimental Methods

2.2.1 Electrolytes

Structures of the ILs and Mg salts investigated and their relevant physical properties are provided in Tables 2.1 and 2.2, respectively. BMIM$^+$, PP13$^+$, and DEME$^+$ were chosen to represent the imidazolium, piperidinium, and tetra-alkylammonium families of IL cations, respectively. ILs containing these cations paired with Tf$_2$N$^-$ or BF$_4^-$ anions were used as solvents, which included BMIM-Tf$_2$N (99%, < 50ppm H$_2$O, Sigma Aldrich, U.S.), PP13-Tf$_2$N (99%, < 50ppm H$_2$O, Iolitec, U.S.), and DEME-BF$_4$ (99%, < 230ppm H$_2$O, Iolitec, U.S.). BMIM-Tf$_2$N and PP13-Tf$_2$N were used as received from the supplier. Because DEME-BF$_4$ had relatively higher water levels, DEME-BF$_4$ was stored over molecular sieves (3Å, Fisher Scientific, USA) for at least 2 days before use to remove residual water. All ILs were handled and stored under an Ar atmosphere in an Omnilab glovebox (Vacuum Atmospheres, USA) with O$_2$ levels below 1 ppm and H$_2$O levels below 0.5 ppm.

Table 2.1 Formulae and structures of the ionic liquids and Mg salts tested in this work.

Ionic liquids	Mg salts
BMIM-Tf$_2$N	Mg(Tf$_2$N)$_2$

PP13-Tf$_2$N   Mg(TfO)$_2$

DEME-BF$_4$ Mg(BH$_4$)$_2$
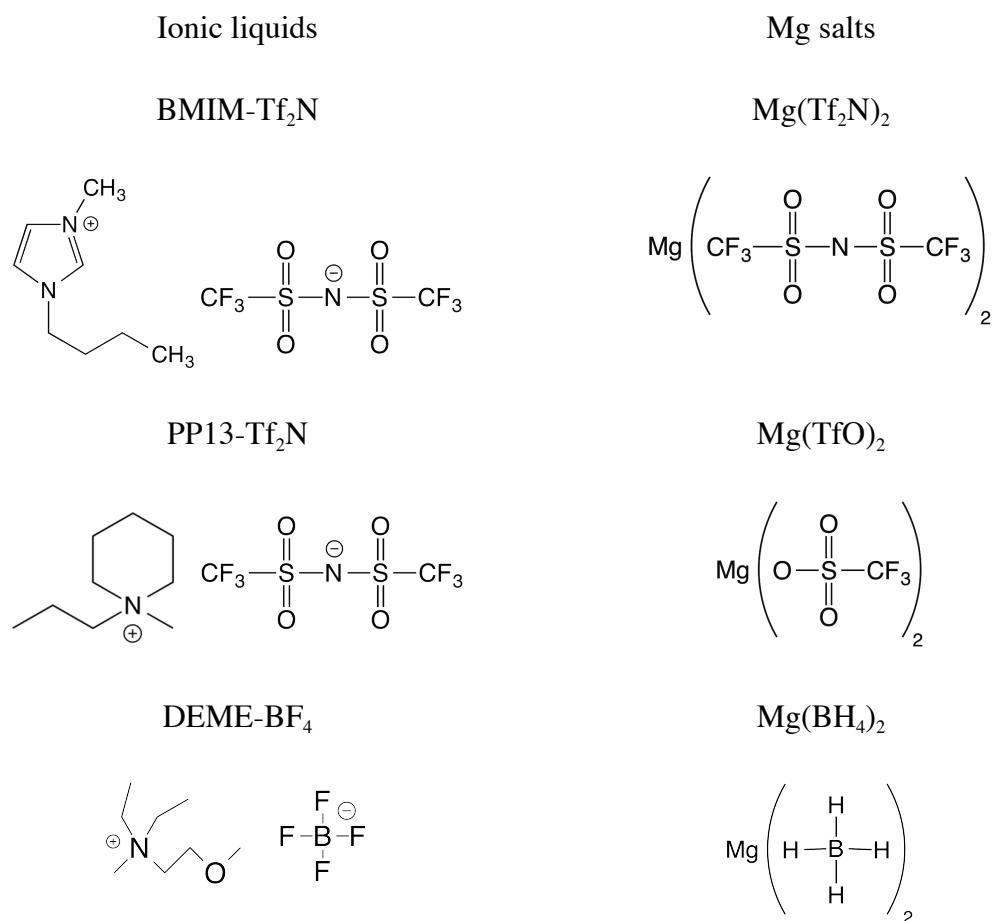
Table 2.2 Relevant physical properties of ILs and organic solvents used in this study.

IL or solvent	Melting point (K)	Density (g/cm^3)	Viscosity (mPa.s)	Conductivity (mS.cm^{-1})
BMIM-Tf$_2$N	289 [83]	1.42 [84]	45 [84]	3.9 [83]
PP13-Tf$_2$N	281 [85]	1.43 [85]	129 [86]	1.5 [85]
DEME-BF$_4$	318 [87]	1.18 [87]	1200 [87]	4.8 [87]
DME	229 [88]	0.86 [88]	0.455 [88]	~0
ACN	254 [88]	0.79 [88]	0.369 [88]	~0

Three Mg salts were considered: $Mg(BH_4)_2$, (95%, Sigma-Aldrich, U.S.), $Mg(TfO)_2$ (98%, Strem Chemicals, U.S.), and $Mg(Tf_2N)_2$ (97%, Strem Chemicals, U.S.). These salts were dissolved in the various ILs by stirring with a PTFE-coated magnetic stir-bar for 1 hour at room temperature. Solvents DME (99.5%, Sigma Aldrich, U.S.) and ACN (99.5%, Sigma Aldrich, U.S.) were stored over molecular sieves (3Å, Fisher Scientific, USA) in the glovebox for at least 5 days before use to ensure dehydration. To isolate the effect of the IL cation on voltammetric response, $Mg(Tf_2N)_2$ was dissolved in two ILs with Tf_2N as the anion, BMIM-Tf_2N and PP13-Tf_2N. In addition, $Mg(TfO)_2$ was dissolved in PP13-TF2N to reproduce a composition examined in a previous report.[72]

The $Mg(BH_4)$/DME system was prepared to confirm that reversible plating and stripping of Mg could be obtained from the simple salt when dissolved in an ethereal solvent.[48] To probe the voltammetric response of $Mg(BH_4)_2$ in IL solvents, solutions of $Mg(BH_4)_2$ in PP13-Tf_2N and DEME-BF_4 were prepared. Finally, co-solvent effects were investigated by mixing DME or ACN with the $Mg(Tf_2N)_2$/PP13-Tf_2N solution.

2.2.2 Working Electrode Preparation

The working electrodes were 50 μm diameter disk microelectrodes, produced in the laboratory by flame-sealing metal wires in soda-lime-glass capillary tubes; Pt (99.997%, Alfa Aesar, U.S.), Au (99.998%, Alfa Aesar, U.S.), W (99.95%, Alfa Aesar, U.S.), Ag (99.997%, Alfa Aesar, U.S.) and Cu (99.999%, Alfa Aesar, U.S.) microelectrodes were produced. The microelectrodes were polished prior to each experiment with a slurry of 0.05 μm alumina particles (Buehler, USA) in 18 MΩ ultrapure water. All microelectrodes were air-dried for 24 hours and exposed to vacuum in the glovebox antechamber for 30 min before each use. In each

IL-solvated binary electrolyte, Pt, Au, and W microelectrodes were used to test whether the working-electrode material affected the electrochemistry. The choice of working electrode did not significantly affect the observed voltammetric response in any experiment, so only data obtained with Pt electrodes are reported here. In addition, Ag and Cu microelectrodes were also used in attempts to reproduce data from previous studies[72, 82] in which those metals were employed as working electrodes.

2.2.3 Electrochemical Measurements

Cyclic voltammetry measurements were carried out in the Omnilab glovebox under an Ar atmosphere at room temperature using an Autolab PGSTAT302N potentiostat (Metrohm, Netherlands). A standard unstirred three-electrode electrochemical cell was used, in which the reference compartment was connected to the working compartment by a Luggin capillary, and the counter compartment was separated from the working compartment by a glass frit. Counter and reference electrodes respectively comprised Mg foil (99%, Goodfellow, U.S.) and Mg wire (99%, Goodfellow, U.S.). Exterior surfaces of the Mg electrodes were removed mechanically in the glovebox prior to each experiment, by scraping their surfaces with stainless steel scissors to expose shiny sub-surfaces.

For all the solutions tested, the voltage window for voltammetry was initially chosen to range from –1 to 1 V vs. Mg/Mg^{2+}. The voltage window was increased by 0.25 V increments separately in the negative or positive directions until reductive or oxidative instability was observed. In each case, the voltammetric response of the Mg-salt/IL solution was compared to that of the neat IL, to deduce whether observed redox activity could be attributed to the Mg salt.

2.3 Results and Discussion

2.3.1 Electrolytes containing Tf$_2$N

Figure 2.1 shows CVs of neat BMIM-Tf$_2$N and 10mM Mg(Tf$_2$N)$_2$ in BMIM-Tf$_2$N on Pt.
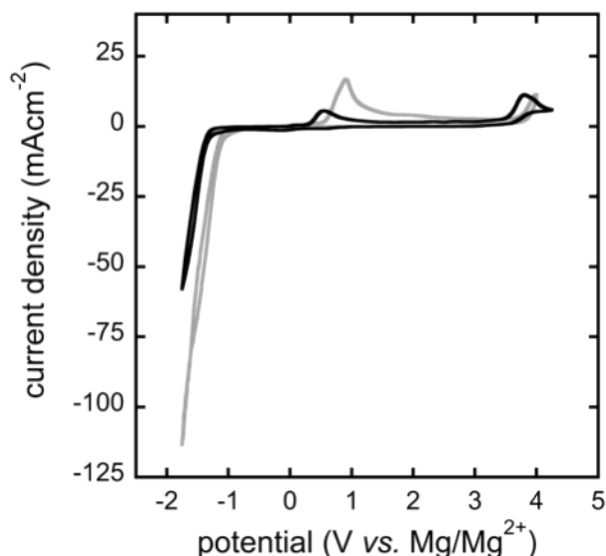
Figure 2.1 Cyclic voltammograms of neat BMIM-Tf$_2$N (light gray) and 10 mM
Mg(Tf$_2$N)$_2$ in BMIM-Tf$_2$N (black) on a 50 μm diameter Pt working electrode at room
temperature; scan rate 100 mV s^{-1}.

The observed electrochemical stability window of 4.6 V agrees with prior reports.[58] For

the 10mM Mg(Tf$_2$N)$_2$ solution, no appreciable cathodic current was observed between 0 V and –

1 V vs. Mg/Mg^{2+}, indicating that Mg plating is inhibited in the Mg/BMIM/Tf$_2$N system. An

increase in cathodic current below –1 V vs. Mg/Mg^{2+} is observed in the CV of the neat IL, as

well as in that of the Mg-salt/IL solution; this voltammetric signature thus appears to arise from

solvent reduction, rather than Mg^{2+} reduction. An oxidation peak near 0.8 V *vs*. Mg/Mg^{2+} appears

in both the presence and absence of the Mg salt, although it shifts to a lower potential when Mg

is present. This peak has been attributed to Mg stripping in the past,[70, 89] but it has also been

observed in previous electrochemical studies using BMIM-BF$_4$,[69, 74] strongly suggesting that the

redox signature arises from BMIM$^+$ oxidation, or from oxidation of BMIM$^+$ reaction products or impurities. As seen in Figure 2.2, the peak height and peak position are stable as a function of cycle number.
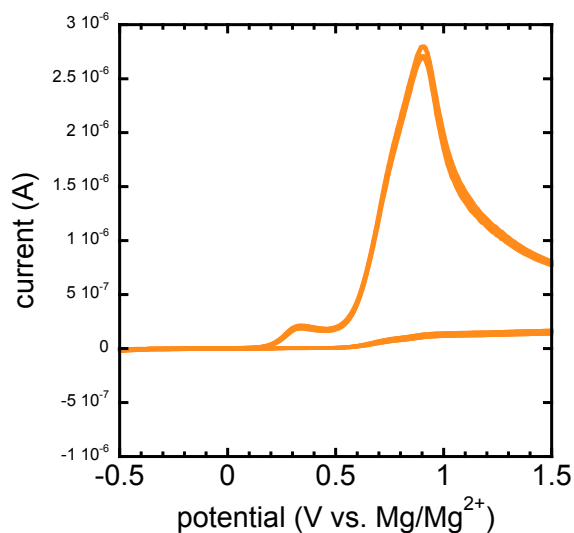
Figure 2.2 Cyclic voltammograms of 10 mM Mg(Tf$_2$N)$_2$ in BMIM-Tf$_2$N on a 50 μm diameter Pt working electrode at room temperature; scan rate 100 mV s^{-1}. Data from three consecutive cycles are overlayed to illustrate the stability of the peak position and height. (Although the data are the same as the data from Figure 2.1, the abscissa and ordinate are magnified to illustrate the peaks more clearly.)

Furthermore, the oxidation peak is still present when the voltage window is constrained between –1 and 3 V vs. Mg/Mg^{2+} but peak height increases as the voltage window is widened in the negative direction, suggesting that it is an oxidation peak that is coupled to reduction reactions below –1 V vs. Mg/Mg^{2+}. This coupling is illustrated in Figure 2.3.

17
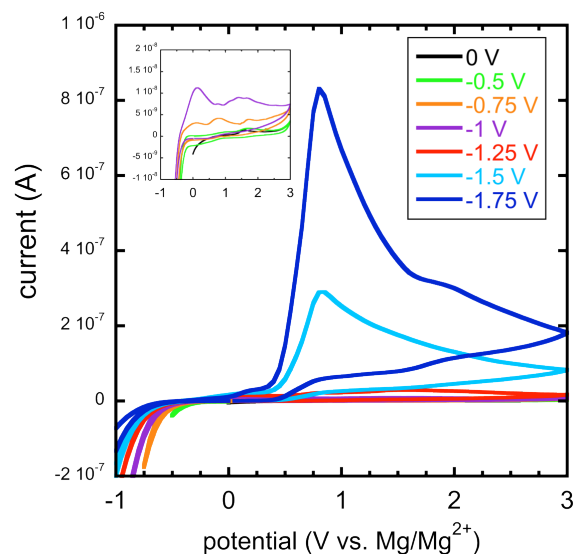
Figure 2.3 Cyclic voltammograms of 10 mM Mg(Tf$_2$N)$_2$ in BMIM-Tf$_2$N as a function of the negative voltage limit of the potential window (identified in the legend), with a positive voltage limit of 3V vs. Mg/Mg^{2+}. Experiments were performed on a 50 μm diameter Pt working electrode at room temperature at a scan rate of 100 mVs^{-1}. The inset has a magnified ordinate axis to provide a clearer representation of voltammograms with lower current levels (–1V, –0.75V, –0.5V and 0V negative voltage limits).

Whether or not they illustrate Mg stripping, these data suggest that BMIM-containing ILs are not useful for Mg electrolytes because they exhibit appreciable redox activity in the voltage range where Mg stripping is expected to occur.

Figure 2.4 shows a CV of neat PP13-Tf$_2$N, which, similar to BMIM-Tf$_2$N, has a wide window of electrochemical stability. The use of PP13$^+$ in this case, along with the absence of redox activity, further supports the hypothesis that the anodic peak observed near 0.8 V vs. Mg/Mg^{2+} in the BMIM-Tf$_2$N CV arises from reactions correlated to the presence of BMIM$^+$.
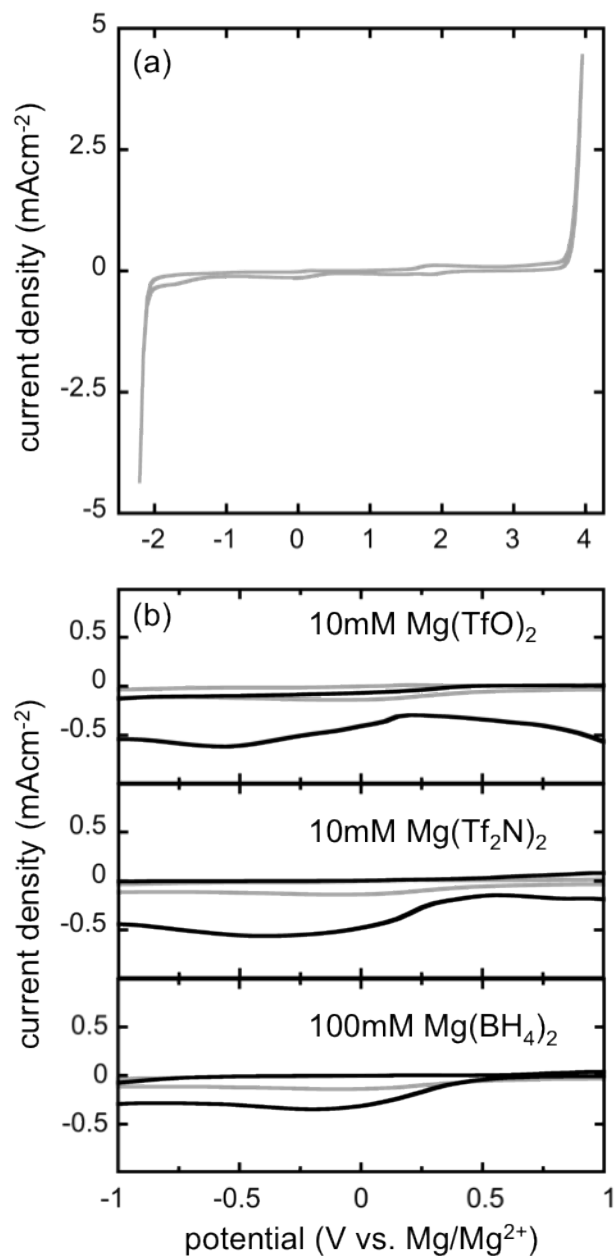
Figure 2.4 Cyclic voltammograms of (a) neat PP13-Tf$_2$N; and (b) Mg salts in PP13-TF$_2$N (black) compared to neat PP13-TF$_2$N (gray), using 50 μm diameter Pt electrodes at room temperature; scan rate 100 mV s^{-1}. Similar voltage windows were used in all cases.

As previously described, NuLi *et al*. reported reversible Mg plating and stripping in PP13-Tf$_2$N with Mg(TfO)$_2$ as the Mg-ion source[72] over a narrow window of –0.5 V to 0.5 V *vs*. Mg/Mg^{2+}. Figure 2.4(b) shows CVs on Pt electrodes for three Mg salts dissolved in PP13-Tf$_2$N

across a wider potential range (the figure details the –1 V to 1 V *vs*. Mg/Mg^{2+} range from CVs gathered across –2.25 V to 4 V *vs*. Mg/Mg^{2+}). The CV for 10 mM Mg(TfO)$_2$ in PP13-Tf$_2$N shows no evidence of Mg plating or stripping. Since the working electrode for the previous report was a Ag plate[72] (and not a Pt microelectrode, as used here), the CV experiments for 1 M Mg(TfO)$_2$ in PP13-Tf$_2$N were repeated with a Ag microelectrode and analyzed in the voltage range of –0.5 V to 0.5 V *vs*. Mg/Mg^{2+}. No significant change in the voltammetric response was detected when the Ag microelectrode was substituted for Pt and the voltage window was narrowed. The CV of 10 mM Mg(Tf$_2$N)$_2$ in PP13-Tf$_2$N shows no redox activity corresponding to Mg plating and stripping, similar to CV for Mg(TfO)$_2$. The CV for 100 mM Mg(BH$_4$)$_2$ in PP13-Tf$_2$N, much like those of the other Mg salts in PP13-Tf$_2$N, also shows no clear evidence of Mg plating or stripping. (In contrast, the previous observation[48] that reversible Mg plating and stripping could be obtained from a solution of Mg(BH$_4$)$_2$ in DME was confirmed.)

The absence of significant Mg redox activity in the Mg(BH$_4$)$_2$/PP13-Tf$_2$N system suggests that Tf$_2$N$^-$ may play a role in blocking Mg plating. This hypothesis is supported by the observation that neither PP13-Tf$_2$N nor BMIM-Tf$_2$N supports Mg electrochemistry. One possible explanation for the absence of Mg plating/stripping in the presence of TF$_2$N$^-$ could be the formation of a passivating film on the electrode surface by anion adsorption or reaction (chemical or electrochemical).[25] Alternatively, plating could be inhibited due to the failure of dissolved Mg(Tf$_2$N)$_2$ to dissociate.

The limited propensity for dissociation of Mg^{2+} from Tf$_2$N$^-$ has been discussed in several computational and experimental prior reports.[82, 90-92] Note, however, that Kakibe *et al*. and Yoshimoto *et al*. have observed reversible Mg plating on Au and Ni with solutions of Grignard reagents in ILs containing Tf$_2$N$^-$.[79-81] Therefore, Mg can be reversibly deposited in the presence of Tf$_2$N$^-$ if Mg is present in the form of a Grignard complex. These results appear to be consistent

with Gregory's hypothesis that the low partial charge on Mg enables the electrochemical removal of Mg from the Grignard molecule.[26] It is possible that Grignard reagents chemically remove a passivation layer that naturally exists on the electrode surface, allowing Mg plating. But when viewed in light of the independence of electrode material, the lack of plating in the systems studied here more likely results from strong association of Mg^{2+} and Tf_2N^- within dissolved $Mg(Tf_2N)_2$ formula units, rather than passivation.

2.3.2 Effect of Co-solvent Addition

In a recent study Kitada *et al*. reported the effects of adding diglyme to a mixture of $Mg(Tf_2N)_2$ and PP13-Tf_2N. They found that CVs of co-solvent systems demonstrated anodic peaks at ~1.3V *vs*. Mg/Mg^{2+}, possibly corresponding to Mg stripping.[82] On the basis of these observations, it was hypothesized that the incorporation into ILs of more polar co-solvents, of which ACN is an extreme example, could lower the solvation energies of the Mg^{2+} and Tf_2N^- ions, promoting dissociation of the $Mg(Tf_2N)_2$ salt.
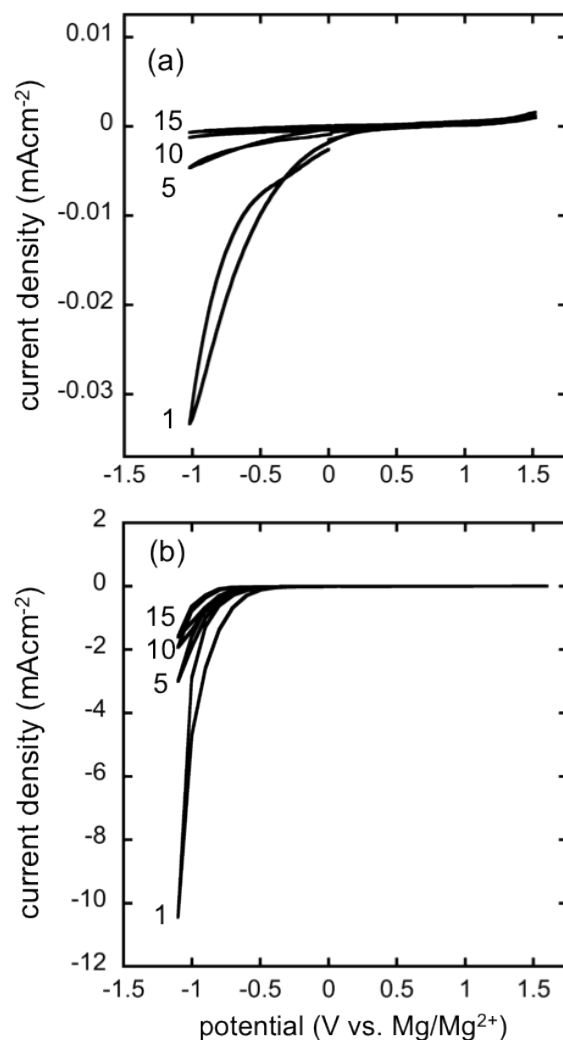
Figure 2.5 Cyclic voltammograms of (a) 100 mM Mg(Tf$_2$N)$_2$ in PP13-Tf$_2$N/DME and (b) 100 mM Mg(Tf$_2$N)$_2$ in PP13-Tf$_2$N/ACN on a 50 μm diameter Pt electrode. Measurements were performed with a scan rate of 20 mV s^{-1} at room temperature. Numbering adjacent to curves indicates the cycle number at which they were gathered.

The effect of co-solvent polarity was investigated by adding DME (dielectric constant 7.2, dipole moment 1.97D) or ACN (dielectric constant 36.6, dipole moment 3.92D) to a Mg(Tf$_2$N)$_2$/PP13-Tf$_2$N solution. The volume ratio (DME or ACN):PP13-Tf$_2$N was 4:1 on a neat-liquid basis and the Mg^{2+} concentration in the mixed co-solvent was 100mM, similar to the

previous study.[82] Figures 2.5(a) and 2.5(b) show CVs of $Mg(Tf_2N)_2$ in PP13-Tf_2N/DME and PP13-Tf_2N/ACN, respectively. No appreciable anodic current was observed up to 1.5 V *vs*. Mg/Mg^{2+}. Furthermore, the magnitude of the cathodic current decreased significantly with increasing cycle number. Because previous reports used Cu working electrodes, additional experiments were performed using Cu instead of Pt, but no change in the voltammetric response was detected. In summary, no evidence of reversible Mg plating and stripping was seen in solutions where DME or ACN co-solvents were added to binary solutions of $Mg(Tf_2N)_2$ in PP13-Tf_2N.

2.3.3 Electrolytes containing BF_4

An IL containing BF_4^- was also studied. Due to the unavailability of $Mg(BF_4)_2$, $Mg(BH_4)_2$ was used as the Mg salt on the basis of the similar structure of the anion. Figure 2.6 shows CVs of neat DEME-BF_4 and 100mM $Mg(BH_4)_2$ in DEME-BF_4 on Pt over two different voltage windows.

To produce Figure 2.6(a), the voltage sweep was extended to the outer boundaries of the solution's stability window – a range of 5.5 V. The anodic current above 1 V vs. Mg/Mg^{2+} has been attributed to oxidation of the BH_4^- anion.[48] The cathodic current observed below –1.5 V vs. Mg/Mg^{2+} likely arises from reductive decomposition of DEME-BF_4. Although the addition of the Mg salt manifests an anodic peak in the CV that does not appear for the neat IL, the observations appear to suggest that this anodic peak does not correspond to Mg stripping.

To produce Figure 2.6(b), the voltage sweep was constrained within –1 and 1 V vs. Mg/Mg^{2+}. Observe that this constraint of the voltage window leads to a voltammetric signature dissimilar from the signature observed in a scan over a wider voltage range – and one more like a typical plating/stripping voltammogram. Although it looks like a

plating/stripping voltammogram, the qualitative appearance of the CV in Figure 2.6(b) is misleading. First, note that the net charge transferred over the portions of the sweeps between 0 V to 1 V vs. Mg/Mg^{2+} for the Mg solution in Figure 2.6(b) is far greater than the charge transferred between –1 V and 0 V *vs.* Mg/Mg^{2+}. Thus the observed anodic current must involve an oxidation process other than Mg stripping, since it is not possible to strip more Mg than is plated. Second, the magnitudes of the currents during the downward sweeps and upward sweeps of voltage –indicated by arrows in Fig. 2.6(b) – appear to be the reverse of what would be expected in the region where Mg plating should occur. In particular, the cathodic current during the return plating sweep (–1 V to 0 V vs. Mg/Mg^{2+}) is lower in magnitude than the cathodic current observed during the forward plating sweep (0 V to –1 V vs. Mg/Mg^{2+}), an atypical characteristic for a plating process. Finally, comparison of the CVs with and without Mg in Figure 2.6(b) reveals that both show significant cathodic current in the 0 V to –1 V vs. Mg/Mg^{2+} range, suggesting that the observed cathodic current likely arises from a reduction event associated with the neat IL that is enhanced by the presence of $Mg(BH_4)_2$.
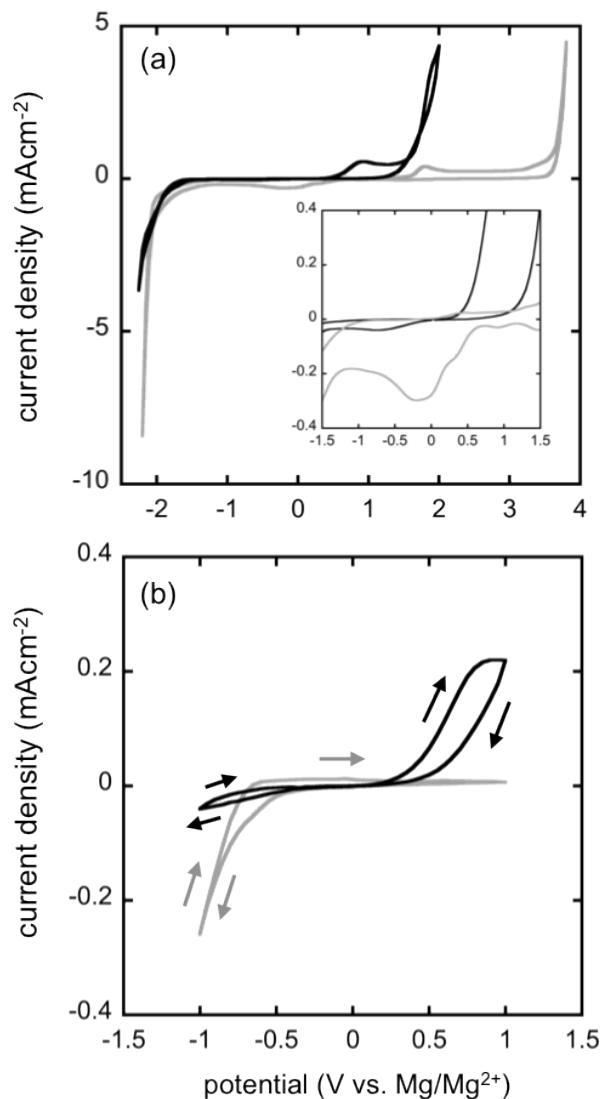
Figure 2.6 Cyclic voltammograms of neat DEME-BF$_4$ (light gray) and 100mM Mg(BH$_4$)$_2$ in DEME-BF$_4$ (black). (a) CV scan limits are chosen to represent electrochemical stability window. Inset shows voltage range restricted to –1.5 to 1.5 V vs. Mg/Mg^{2+}. (b) CV scan limits are constrained to –1 to 1 V vs. Mg/Mg^{2+}. Working electrode is 50 μm diameter Pt electrode; scan rate: 100 mV s^{-1}; measurements performed at room temperature.

The reduction peak (around 0V vs. Mg/Mg^{2+}) observed for neat DEME-BF$_4$ in Figure 2.6(a) is absent in Figure 2.6(b). Thus its appearance can be associated with an oxidation event that takes place above 1 V vs. Mg/Mg^{2+}.

Since it was confirmed that $Mg(BH_4)_2$ allows reversible Mg plating from ethereal solvents such as DME, the apparent absence of Mg plating/stripping in the DEME-BF_4/$Mg(BH_4)_2$ system suggests that solvent effects are highly important. In the DEME-BF_4 solvent case, the anion of the IL, can strongly associate with dissociated Mg^{2+} and hinder reversible Mg plating.

2.4 Conclusion

Cyclic voltammetry was used to investigate the electrochemistry of electrolytic solutions consisting of various Mg salts ($Mg(TfO)_2$, $Mg(Tf_2N)_2$, $Mg(BH_4)_2$), IL solvents (BMIM-Tf_2N, PP13-Tf_2N, DEME-BF_4) and organic co-solvents (DME, ACN) on Pt working electrodes. Contrary to some prior reports, reversible Mg plating was not observed for any of these salt/IL combinations. In some cases the disagreement with prior observations arises from different interpretations of the voltammograms, as suggested by more robust control experiments in which the identity of the IL cation was varied, as well as by exploration of wider voltage ranges during voltammetry.

The present results indicate that when evaluating a new Mg-containing IL solution it is imperative also to evaluate the redox activity associated with the neat IL. It was found that the anodic peak observed at ~0.8V *vs*. Mg/Mg^{2+} in the voltammetry of $Mg(TfO)_2$ dissolved in BMIM-BF_4, previously attributed to Mg stripping, likely originates from redox activity correlated to the presence of $BMIM^+$.

$Mg(TfO)_2$ dissolved in PP13-Tf_2N has been reported to exhibit reversible Mg plating, but voltammetry of three Mg salts in PP13-Tf_2N did not show evidence of reversible Mg plating in the current investigation. The addition of two organic solvents of varying polarity to $Mg(Tf_2N)_2$/PP13-Tf_2N also did not give rise to signatures of Mg plating or stripping.

$Mg(BH_4)_2$ in DEME-BF$_4$ was also considered, but, similar to the other systems, no evidence of Mg plating or stripping was observed. A voltammetric signature that looked qualitatively like a plating/stripping voltammogram could be obtained by constraining the voltage window, but the magnitudes of the cathodic currents during the downward and upward voltage sweeps were inconsistent with a plating process, and the net anodic charge transfer above 0 V vs. Mg/Mg^{2+} far outweighed the net cathodic charge transfer below 0 V vs. Mg/Mg^{2+}, suggesting an oxidation reaction besides stripping.

Taken together, these findings suggest that the failure of Mg to plate from electrolytes containing Tf$_2$N$^-$ and BF$_4^-$ may owe to their strong coulombic attraction to Mg^{2+}, which is a consequence of the extremely high charge density of the Mg^{2+} cation. The strong association of Tf$_2$N$^-$ and Mg^{2+} could not be overcome by attempts to lower the ion solvation energies by adding high-polarity co-solvents. It therefore seems unlikely that simple Mg salts can be used as the Mg source in IL-based electrolytes for secondary Mg batteries unless new measures are taken to foster dissociation of the Mg salt or lower ion solvation energies significantly. It can be foreseen that a Mg-containing IL cation with lower charge density than Mg^{2+}, or an anion shared by the salt and IL that is more readily solvated by the IL, could enable Mg plating. It is also possible that addition of strong Lewis acids to IL-based solutions could overcome the attraction between ions in simple Mg salts, favoring dissociation and enabling Mg plating from ILs. These approaches are suggested for future development of IL-based Mg electrolytes.

Chapter 3 Identifying the Discharge Product and Reaction Pathway for a Secondary

Mg/O$_2$ Battery

3.1 Introduction

Non-aqueous metal/oxygen batteries exhibit high theoretical specific energy capacities.[10] Chemistries based on alkali metals, such as Li/O$_2$, Na/O$_2$, and K/O$_2$, have become popular research topics because they also hold promise for rechargeability.[93-96] Multivalent battery systems involving alkaline earth metals, such as the Mg/O$_2$ chemistry, can achieve higher theoretical energy densities than some of their alkali-metal analogues but have received little research emphasis.[54-55] Although aqueous primary Mg/O$_2$ batteries have been demonstrated, their cell potentials are limited by the presence of water; moreover, corrosion of the Mg electrode likely precludes rechargeability.[20-22, 97] Non-aqueous electrolytes could enable a reversible Mg/O$_2$ cell, however. In this chapter, we demostrate a rechargeable non-aqueous Mg/O$_2$ cell and identify the discharge product chemistry.

3.2 Experimental Methods

3.2.1 Cell assembly and testing

Each Mg/O$_2$ cell consisted of a Mg negative electrode, a glass-fiber separator, and a porous carbon positive electrode, which were all discs with 18 mm diameters. The Mg electrode comprised 0.25 mm thick magnesium foil (Goodfellow, 99.9%, USA). The Mg surface was scraped with the edge of stainless-steel scissors (Vacuum Atmospheres) to expose a shiny

subsurface before cell assembly; the scraping was performed in an Omnilab glovebox (Vacuum Atmospheres, USA) with an Ar atmosphere (99.998%, Cryogenic Gases, USA) containing less than 1 ppm O_2 and less than 1 ppm H_2O. The glass-fiber separator (EL-CELL Gmbh, Germany) had a thickness of 0.55 mm. The positive electrode comprised carbon paper (SIGRACET GDL 24 BC, Ion Power, Inc., USA) with a porosity of 0.8 (per supplier), thickness of 235±20 mm (per supplier), and specific area of 13.3±0.2 m^2g^{-1} (measured by N_2 physisorption with a Micromeritics ASAP 2010 analyzer employing the Brunauer-Emmett-Teller isotherm).[98] The average positive-electrode weight was 0.0265 g. The separator and the carbon electrode were vacuum dried at 110°C for at least 8 hours before being transferred to an Ar atmosphere for cell fabrication.

ECC-AIR metal-oxygen electrochemical test cells were purchased from EL-CELL GmbH (Germany). Cells were assembled under Ar in the glovebox. Before cell assembly, the separator and positive electrode were immersed in the electrolytic solution to ensure that the pores were filled. The cell was assembled by placing the electrolyte-soaked positive electrode on top of the Pt-coated current collector. Then, the electrolyte-soaked separator was placed on the carbon electrode. Finally, the Mg electrode was placed on the separator, as shown in Figure 3.1. The electrode sandwich was slid into a cylindrical poly ether ether ketone sleeve with 18 mm inner diameter, which was inserted into a stainless steel cup that acted as the negative current collector.
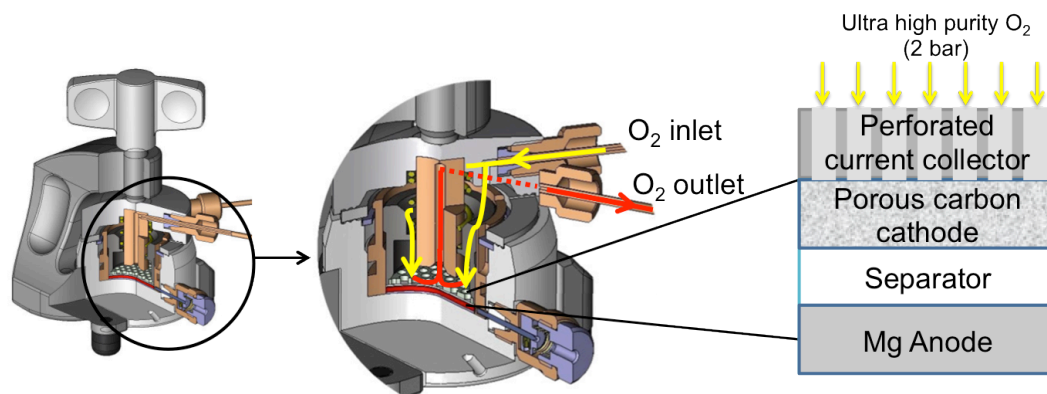
Figure 3.1 Schematics of the ECC-Air cell from EL-CELL.[99]

After completion of assembly and sealing with a threaded cap that acted as the positive current collector, the cell was removed from the glovebox and the O_2 inlet was connected to a high purity O_2 tank (99.993%, Cryogenic Gases, USA) at a pressure of 2 bar absolute. The O_2 outlet is sealed throughout the discharge and recharge experiments to maintain a static absolute pressure of 2 bar.

The Mg/O_2 cells held under pressurized O_2 were connected to a Series 4000 battery tester (Maccor, USA). The open-circuit voltage was recorded until the rate of voltage change was observed to fall below 2 mVh^{-1}, following the procedure suggested by Griffith *et al.*[98] After voltage equilibration, discharge tests were initiated by applying a constant current.

Cell discharge rates are reported as superficial quantities, which were determined using the cross-sectional area of the 18mm-diameter positive electrode. Thus, for example, a 5 µAcm^{-2} rate corresponds to a galvanostatic discharge at 12.7 µA. Discharge tests were terminated when the voltage dropped below a cutoff voltage of 0.6V.

Before initiating recharge, cells were rested for 30 min to allow equilibration of oxygen. During these rests, the voltage was observed to relax to the open-circuit potential that had been reached before first discharge. Recharges were always performed using the same rate as the preceding discharge. Recharge steps were terminated when the discharge capacity for the

corresponding discharge/charge cycle was reached. Cells were also rested for 30 min between each discharge/recharge cycle.

After the conclusion of each test, the Mg/O$_2$ cell was flushed with high purity Ar gas via a three-way valve. The gas lines were then sealed, disconnected from the gas manifold, and returned to the glovebox for post-mortem analysis.

Control experiments for first discharge were run with the same fabrication steps (cell assembly, O$_2$ pressure, and Ar purge). These cells were held at zero current for the same period over which the other cells were discharged. A typical response is shown in Figure 3.4. Further control experiments were done by discharging under Ar gas, without exposing the cell assembly to O$_2$. Representative data are presented in Figures 3.2 and 3.3. These cells were assembled in the glovebox and kept inside the glovebox and connected to the battery tester; the open-circuit voltage was recorded until equilibration. Discharge tests were initiated by applying a constant current corresponding to 5 μAcm^{-2} (superficial).
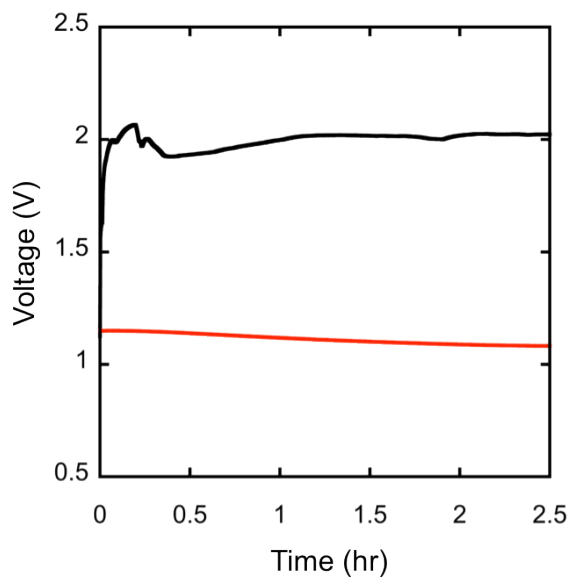
Figure 3.2 Zero-current holds for a Mg/O_2 cells with (black line) and without O_2 exposure (red line) prior to start of discharge experiment.
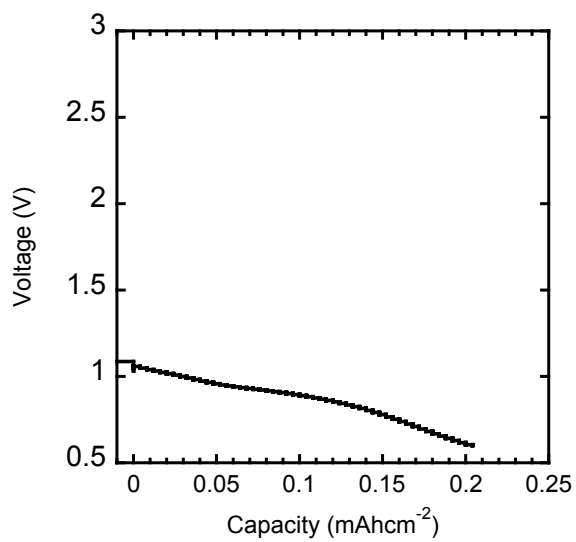
Figure 3.3 Discharge curve for a cell assembly that was never exposed to O_2. Discharge rate is 5 μAcm^{-2} (superficial).

Constant current constant voltage (CCCV) control experiments were run with the same fabrication steps (cell assembly, O_2 pressure, and Ar purge). These cells were held at open circuit (current = ~0 A) until the voltage equilibrated. Then, the voltage was kept constant at the equilibrated open circuit voltage, and current was measured. Figure 3.4 shows a typical response.
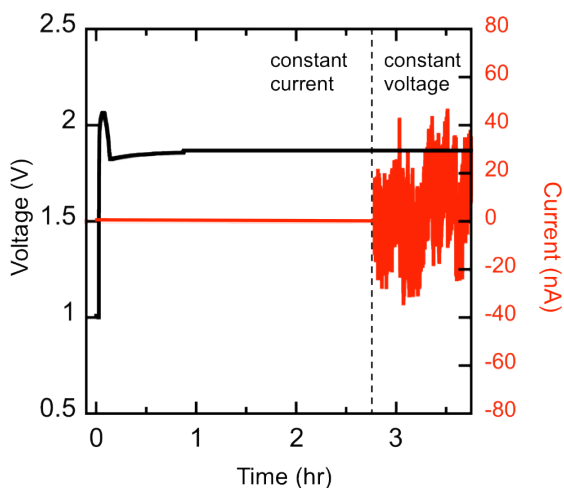
Figure 3.4 CCCV control experiment for a Mg/O_2 cell. Dashed line indicates transition from constant current (current = ~0 A) to constant voltage (voltage = open circuit voltage).

3.2.2 Electrolyte synthesis and characterization

The electrolyte used in this study was developed by the University of Michigan Chemistry Department and was synthesized following the procedure described by Nelson *et al.*[53] The oxidative stability of the electrolyte on Pt electrodes was confirmed to be above 4 V *vs.* Mg/Mg^{2+}, as shown in Figure 3.5. Voltammetry was also repeated using glassy carbon, which yielded a similar response, as shown in Figure 3.6.
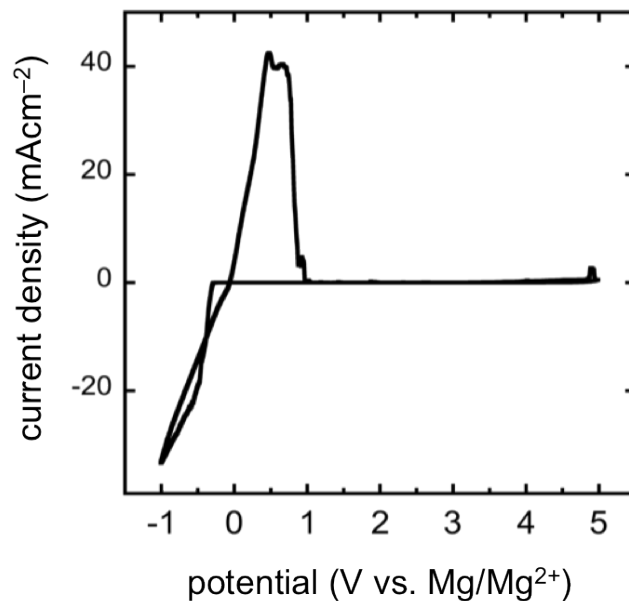
Figure 3.5 Cyclic voltammogram at 100 mVs^{-1} for 4:1 PhMgCl:Al(OPh)$_3$/THF on a 50 μm radius Pt working electrode at room temperature. The counter and reference electrodes were polished Mg foil and polished Mg wire, respectively.
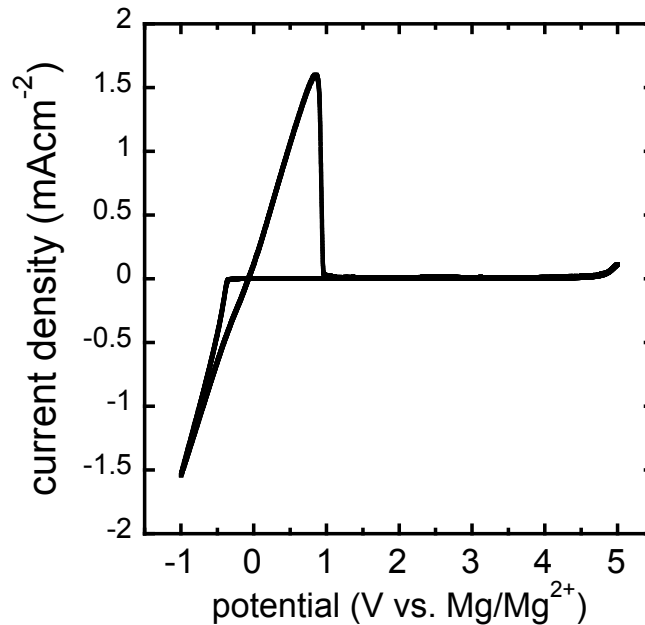
Figure 3.6 Cyclic voltammogram at 100 mVs^{-1} for 4:1 PhMgCl:Al(OPh)$_3$/THF on a 1.5 mm radius glassy carbon working electrode at room temperature. The counter and reference electrodes were polished Mg foil and polished Mg wire, respectively.

3.2.3 Scanning Electron Microscopy (SEM)

SEM was performed with a FEI Nova NanoLab microscope (5 kV accelerating voltage, 98 pA), using the airtight sample holder described earlier by Griffith *et al.*[98] Samples were transferred to the SEM chamber following Griffith *et al.*'s procedure. The holder is designed to be opened under vacuum in the microscope chamber, avoiding exposure to ambient air during sample transfer. In preparation for imaging by SEM, the positive electrodes were rinsed with THF in an Ar-atmosphere glovebox to remove residual electrolyte.

3.2.4 Energy Dispersive Spectroscopy (EDS)

EDS was performed in conjunction with SEM using a FEI Nova NanoLab microscope (5 kV accelerating voltage, 98 pA) and EDAX XEDS software. The spectra were collected in spot mode.

3.2.5 Raman Spectroscopy (RS)

Samples for RS were placed in a sample holder consisting of two parallel quartz slides sealed with silicone sealant (GE510, General Electric) on all four sides of the gap between them. After placement between the slides and sealing in the glovebox, the holder was rested for 24 hours to allow the sealant to harden. Raman spectra were collected by a Renishaw inVia spectrometer. The laser wavelength was 532 nm and the laser power was kept at 5% in order to avoid damaging the carbon in the sample. The maximum power for the laser was 300mW and the Raman spectra were collected in extended mode from 0 to 1700 cm^{-1}. An automated XYZ stage was used to focus the beam and move to different areas of the sample.

Density functional perturbation theory[100-101] was used to calculate Raman activities in MgO_2. Calculations were performed using the VASP code.[102-105] The generalized gradient approximation (GGA) expressed using the formulation of Perdew-Burke-Ernzerhof (PBE) was used for the exchange-correlation energy.[106] A kinetic-energy cutoff of 520 eV was used for the planewave basis, and the Brillouin zone was sampled with a regular, Γ-centered grid with a density of 16×16×16, corresponding to 24 k-points per Å. All ion positions were relaxed to a force tolerance less than 10^{-5} eVÅ^{-1}. Born effective-charge tensors and dielectric tensors were calculated for each atom according to the method of Gajdos.[107] The Hellmann–Feynman forces were used in combination with the supplemented direct method[108] to evaluate the interatomic force constants of a 2×2×2 supercell. To calculate the phonon frequencies in the long wavelength limit, the macroscopic electric field that follows from the collective displacement of ions was treated separately using the non-analytical form[100, 109] of the dynamical matrix. The derivatives of the polarizability tensor with respect to atomic displacements were calculated by a finite-difference approach in which ions were displaced ±0.06 Å in each Cartesian direction. The Raman susceptibility tensor was then constructed and applied to the differential cross section for nonresonant first-order Raman scattering. The calculation was performed for a polycrystal using 532 nm unpolarized light at 300 K. Density functional perturbation theory calculations were performed and analyzed by Jeff Smith.

3.2.6 Auger Electron Spectroscopy (AES)

AES was performed with a Physical Electronics Auger Nanoprobe 680 instrument using a beam voltage of 3kV and a beam current of 10 nA. The positive-electrode sample was exposed to air before being placed in transfer chamber and drawn to 1.0 μTorr vacuum. Then the sample

was transferred to the analysis chamber (~1.5 nTorr). Auger spectra were collected in the range of 0 to 2 keV. Since the sample was exposed to air during transfer, the sample surface was sputtered with Ar at a rate of 2.5 $nm\,min^{-1}$ and Auger spectra were collected after each layer was removed to see if the elemental composition varied as a function of depth.

3.2.7 X-ray Diffraction

XRD samples were placed in an air-tight sample holder with a Be window (2455-SH-001, Rigaku, Japan). Diffraction patterns were gathered by a Rotaflex (40 kV, 100 mA) diffractometer (Rigaku, Japan) with a Cu Kα source at 0.75° min^{-1} and at 0.02° step size.

3.3 Results and Discussion

3.3.1 Discharge Voltage and Electrochemical Testing

In a Mg/O_2 cell, the half-reactions

$Mg^{2+} + O_2 + 2e^- \rightleftharpoons MgO_2$ (2.91 *vs*. $Mg^{2+/0}$)   [1]

$2Mg^{2+} + O_2 + 4e^- \rightleftharpoons 2MgO$ (2.95 *vs*. $Mg^{2+/0}$)   [2]
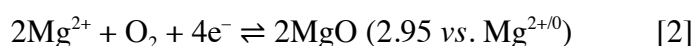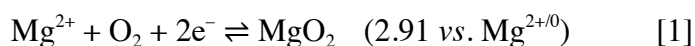
might be anticipated at the gas electrode. Both involve Mg^{2+} ions and dissolved O_2 from the liquid electrolyte, and both promise moderately high cell potentials of ~2.9 V. A Mg/O_2 cell with a MgO discharge product formed by half-reactions 1 or 2 would exhibit theoretical maximum volumetric and gravimetric energy densities of approximately 14 $kWhL^{-1}$ and 3.9 $kWhkg^{-1}$, respectively, surpassing Li/O_2 cells that discharge to Li_2O_2 (8.0 $kWhL^{-1}$ and 3.4 $kWhkg^{-1}$).[10]

Each Mg/O_2 cell in this study was held at open circuit under O_2 until the measured voltage equilibrated, typically yielding an open-circuit potential (OCP) of 2.0 ± 0.1 V. (see Fig. 3.4). This OCP is low compared to the theoretical potentials expected from half-reactions 1 or 2.
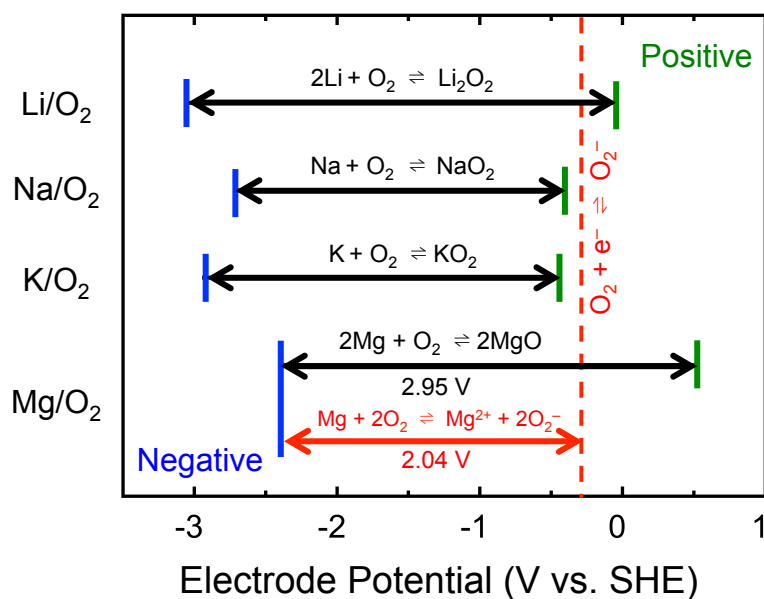
Figure 3.7 Cell potentials and half-reaction potentials for several metal/O_2 battery chemistries. The dashed red line corresponds to the potential at which O_2 reduces to superoxide.

Figure 3.7 compares the half-reaction potentials for the Mg/O_2 system with the accepted half-reaction potentials of various alkali-metal/O_2 chemistries. In all cases, cells based on alkali metals exhibit OCPs close to the theoretical potentials expected for positive-electrode half-reactions involving the direct electrochemical formation of M_xO_y compounds from metal cations and O_2.[94-95, 110] As Fig. 3.7 shows, however, the potential associated with superoxide formation ($O_2 + e^- \rightleftharpoons O_2^-$, –0.33 V vs. SHE) in the alkali chemistries *also* closely matches the potentials for direct electrochemical M_xO_y formation from Li, Na, and K, making identification of the reaction pathway more challenging. In contrast, for Mg/O_2, superoxide forms from O_2 well (~0.9 V) below the potential for direct electrochemical MgO formation.

In light of the thermodynamic data summarized on Fig. 3.7, the OCP in the Mg/O_2 system suggests a reaction pathway where oxygen reduction (*i.e.*, O_2^- formation) occurs as an initial electrochemical step: superoxide formation precedes a chemical reaction with Mg^{2+} that forms MgO_2 and liberates molecular O_2, after which MgO_2 disproportionation occurs:

38

$$O_2 + e^- \rightleftharpoons O_2^- \quad (2.04 \text{ V } vs. \text{ Mg}^{2+/0}) \qquad [3a]$$

$$2\,O_2^- + Mg^{2+} \rightleftharpoons MgO_2 + O_2 \qquad [3b]$$

$$2\,MgO_2 \rightleftharpoons 2\,MgO + O_2 \qquad [3c]$$
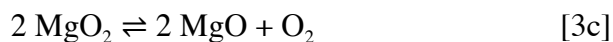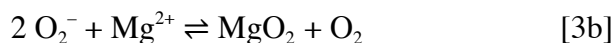
This hypothesized pathway is an ECC ("electrochemical-chemical-chemical") mechanism similar to those proposed for Li/O$_2$ and other alkali-metal-based systems.[111-114] Below, the results of several characterization techniques confirm that the discharge-product composition is also consistent with this ECC mechanism.

Unlike alkali-metal/O$_2$ systems, superoxide formation in Mg/O$_2$ cells occurs at a low enough potential to distinguish step 3a from direct electrochemical formation of MgO$_x$ (reactions 1 and 2). The subsequent chemical steps that form MgO$_2$ and MgO do not contribute to the electrical work delivered by the cell. Materials that select against the superoxide pathway and support direct electrochemical formation of MgO$_x$ will be needed to realize the promise that the Mg/O$_2$ chemistry holds for higher energy density.
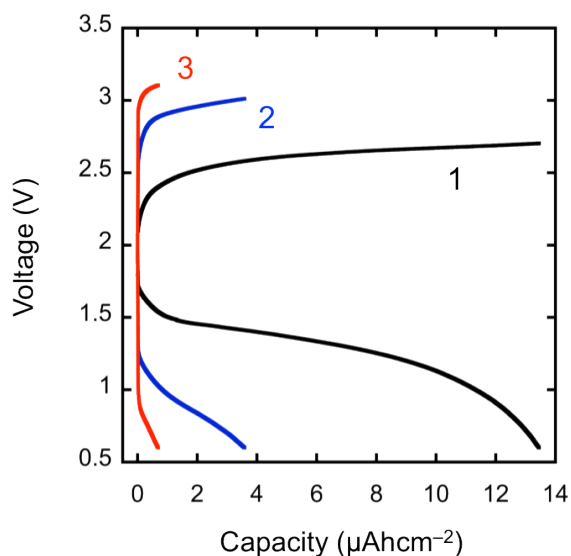
Figure 3.8 Discharge/recharge cycles for a room-temperature Mg/O$_2$ cell using 4:1 PhMgCl:Al(OPh)$_3$/THF at 5 μAcm^{-2} (superficial). Curves are labeled with the corresponding cycle numbers.

Figure 3.8 shows discharge/recharge cycles for a typical Mg/O_2 cell. During discharge, the voltage decreases monotonically until reaching the 0.6 V cutoff. At the end of discharge the cell is allowed to equilibrate for 30 min before recharging. Once a charging current is applied, the voltage quickly jumps to 2.5 V, and then rises monotonically until the discharge capacity is recovered. The energy efficiency for the first cycle is 42% – low compared to the energy efficiencies reported for non-aqueous Li/O_2, K/O_2 and Na/O_2 chemistries, but comparable to those for elevated-temperature Mg/O_2 cells.[54, 94-95, 115] Still, the overpotentials during the discharge and recharge processes are similar, suggesting that the electrochemical steps involved in the forward and reverse cell reactions have similar activation energies. Upon cycling, the capacity fade compares with other reported non-aqueous Mg/O_2 systems.[54-55] The cell capacity is low, probably owing to the low solubility and diffusivity of O_2 in the electrolyte.[116] The solubility of O_2 in THF is about 5 times lower than in DME, a common metal/O_2 battery solvent.[117-118] The measured conductivity of the present electrolyte was reported by Nelson *et al*. to be 1.24 mScm$^-$^{1},[53] which is comparable to other Mg electrolytes[40, 44, 46, 119] but almost an order of magnitude smaller than typical lithium-battery electrolytes.[24, 120] Development of an electrolyte with higher O_2 solubility and ionic conductivity could facilitate improvements in both the capacity and rate capability of Mg/O_2 chemistry.
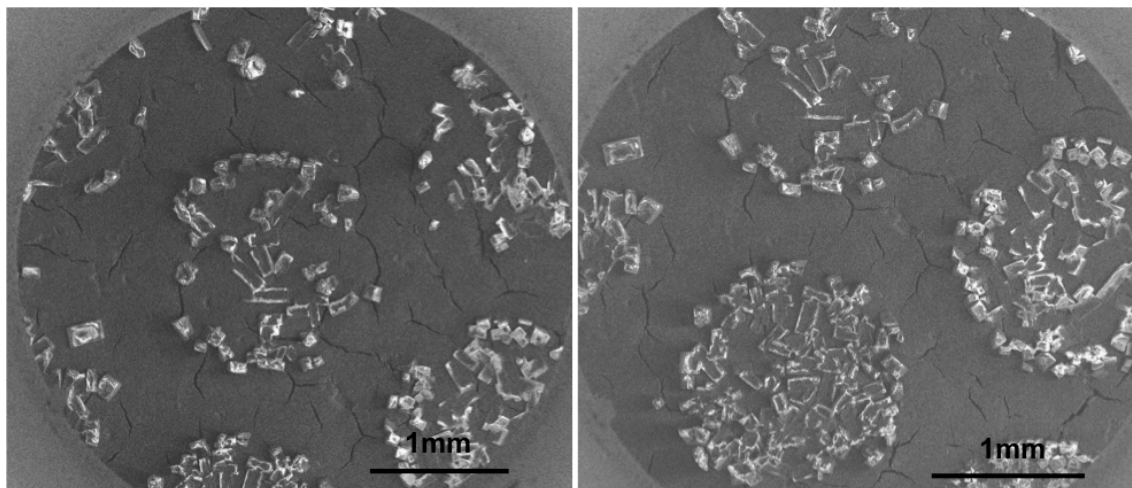
Figure 3.9 SEM images of positive electrode at the end of first discharge for Mg/O_2 cell using 4:1 PhMgCl:Al(OPh)$_3$/THF electrolyte.

Assuming that the discharge product comprises MgO particles with similar sizes and surface density to those depicted in Figure 3.9, the measured charge capacity is within an order of magnitude of the amount expected from the amount of discharge product. It is important to emphasize that a capacity estimate based on the discharge-product dimensions is at best qualitative; such an estimate is presented here only to demonstrate consistency with the more accurate capacities determined by discharge experiments. To probe possible side reactions, discharge was attempted in an Ar atmosphere (*i.e.*, in a cell containing no O_2). In this case the measured OCP was roughly half that of the O_2-containing cell, 1.0 ± 0.1 V (Fig. 3.3). Upon discharge the voltage monotonically decreased (Fig. 3.4), suggesting that there is a side-reaction below 1V that may arise from solvent degradation. Side reactions at low voltages are also observed in the Li/O_2 system.[121]
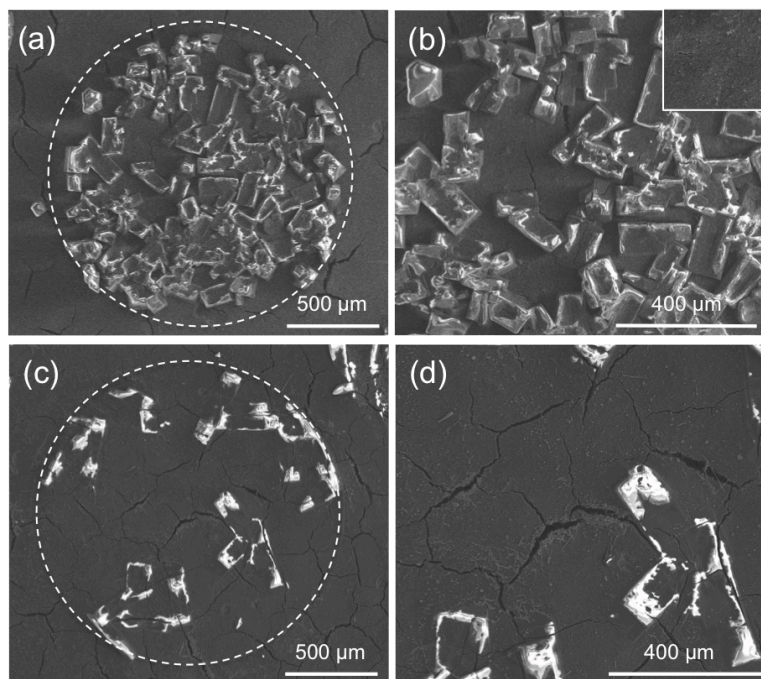
Figure 3.10 SEM images of the positive-electrode surface on the side closest to the O_2 gas inlet for Mg/O_2 cell using 4:1 PhMgCl:Al(OPh)$_3$/THF electrolyte. The dashed circles represent boundaries of the regions that were directly exposed to O_2 through perforations in the Pt-coated current collector. (a) An electrode after first discharge. (b) Higher magnification of the first-discharge product, with an inset image of a control electrode exposed to O_2 in a cell held at open circuit. (c) An electrode at the end of first recharge. (d) Higher magnification of the residual product after first recharge.

Figures 3.10(a) and 3.10(b) show SEM images of the oxygen-electrode surface after discharge. Discharge product is concentrated within areas of the electrode that were in direct contact with O_2 through the perforations in the current collector. The product comprises large, faceted, transparent particles, which have characteristic dimensions of 100-200 μm. These particles were only observed on the side of the positive electrode exposed to O_2. Absence of the discharge product in areas further from the O_2 supply indicates that O_2 permeation through the liquid electrolyte limits capacity. A control image [Fig. 3.10(b) inset] was generated by holding a similar cell at open circuit under O_2 for the same duration as the discharge experiment (a larger area is shown in Fig. 3.9). No particles were observed on the control electrode. Figures 3.10(c)

and 3.10(d) show that a majority of the particles have been decomposed at the end of first recharge. The incomplete disappearance of the discharge product suggests the presence of side reactions, which may rationalize both the low energy efficiency and the capacity fade upon cycling.

3.3.2 Discharge Product Characterization

The composition of the discharge product was characterized using EDS, AES, XRD, RS.
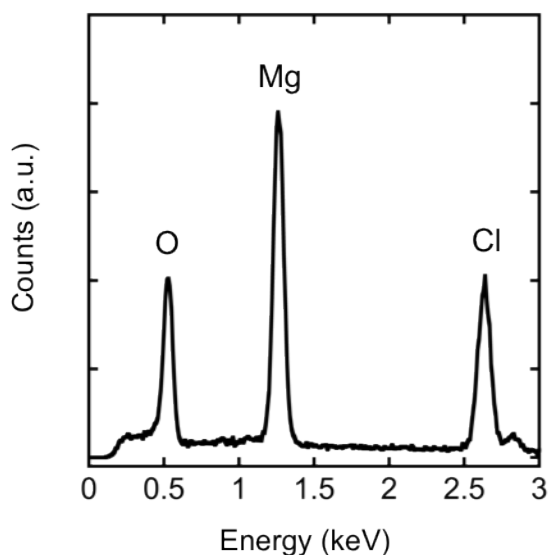
Figure 3.11 Energy Dispersive Spectroscopy (EDS) spectrum collected with a beam focused on the discharge phase for Mg/O$_2$ cell using 4:1 PhMgCl:Al(OPh)$_3$/THF electrolyte.
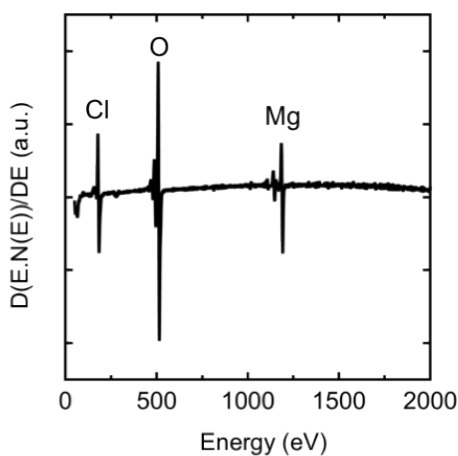
Figure 3.12 AES spectrum of the discharge phase for Mg/O$_2$ cell using 4:1 PhMgCl:Al(OPh)$_3$/THF electrolyte.

43

As seen in Figure 3.11, EDS suggested the presence of Mg, O, and Cl in the discharge product. In agreement with the EDS results, AES also showed signals for only Mg, O, and Cl. (Figure 3.12). The Mg peak is located at 1181.5 eV, in agreement with the Mg $KL_{2,3}L_{3,3}$ Auger energy of Mg in MgO.[122] In contrast to the EDS measurement, samples analyzed by AES were briefly exposed to air during sample transfer. Therefore, AES was performed in conjunction with Ar sputtering to remove the exterior surface of the discharge product.
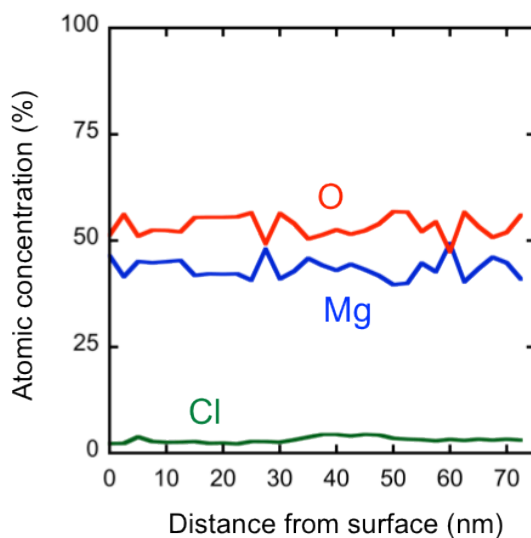
Figure 3.13 AES depth profile of the discharge product for Mg/O$_2$ cell using 4:1 PhMgCl:Al(OPh)$_3$/THF electrolyte; Mg (Blue), O (red) and Cl (green) atomic concentrations are plotted as functions of sputtering depth.

Figure 3.13 shows the atomic-composition percentages with respect to the distance from the surface yielded by an AES depth profile. The results suggest MgO$_x$ stoichiometry with $x > 1$. Furthermore, AES reveals that the quantity of Cl in the discharge product is small (average ~3.1 at.%), and presumably owes to reaction with the electrolyte. It is noteworthy that the proportions of Mg, O and Cl remain relatively constant with respect to depth. The excess of O can be explained by the presence of domains of MgO$_2$ within the predominantly MgO material. The

Mg-O phase diagram indicates that MgO is a line compound, and is the only stable Mg-O compound at ambient conditions.[123] Based on the theoretical potentials from Eqs. 1 and 2, MgO_2 has a higher formation energy than MgO (by ~0.08 eV/formula unit); it is therefore weakly metastable and does not appear in the equilibrium phase diagram. Thus presence of MgO_2 in the discharge product likely owes to a kinetic effect.

If the discharge product is assumed to be a physical mixture of crystalline, solid MgO and MgO_2, one can calculate the volumetric ratios of the two compounds by comparing the AES signals associated with oxygen and magnesium. The density values needed for this calculation are listed in Table 3.1.

Table 3.1 Densities and Molar Masses for MgO and MgO_2

	MgO	MgO_2
Density (g/cm^3)	3.58	3.00
Molar mass (g/mol)	40	56

The ratio of oxygen signal to the magnesium signal as measured by AES is 1.04 on average for the discharged positive electrode. Relating these values through the equation

$$\frac{\frac{32}{56}\left(\text{Volume}_{MgO_2} \times \text{Density}_{MgO_2}\right)+\frac{16}{40}\left(\text{Volume}_{MgO} \times \text{Density}_{MgO}\right)}{\frac{24}{56}\left(\text{Volume}_{MgO_2} \times \text{Density}_{MgO_2}\right)+\frac{24}{40}\left(\text{Volume}_{MgO} \times \text{Density}_{MgO}\right)}=\frac{\text{Oxygen AES}}{\text{Magnesium AES}} \approx 1.04$$

the $\text{Volume}_{MgO2}/\text{Volume}_{MgO}$ is found to be ~0.5. Therefore, ~30% of the volume probed by AES is occupied by MgO_2.
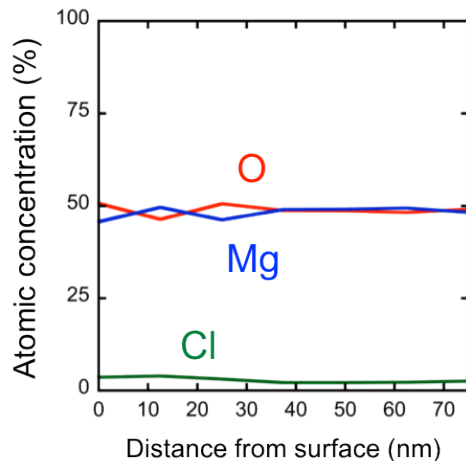
Figure 3.14 AES depth profile of the recharged discharge product for Mg/O$_2$ cell using 4:1 PhMgCl:Al(OPh)$_3$/THF electrolyte; Mg (Blue), O (red) and Cl (green) atomic concentrations are plotted as functions of sputtering depth.

In contrast to the oxygen-rich composition of the discharge product, particles remaining on the positive electrode after recharge exhibit a 1:1 Mg:O ratio in AES (Figure 3.14). This suggests that MgO$_2$ decomposes preferentially during charging.
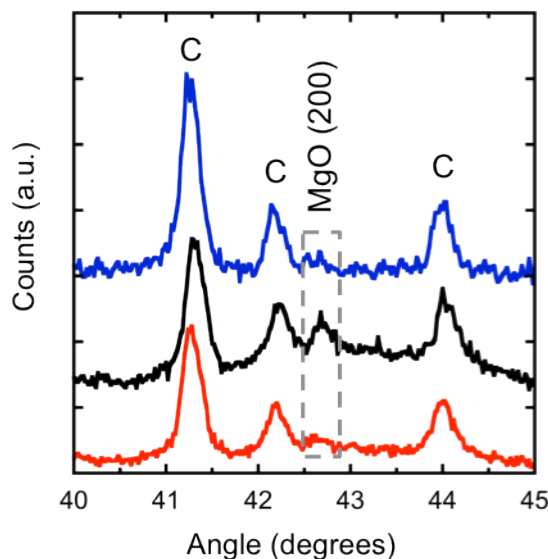
Figure 3.15 XRD pattern of control (red), discharged (black) and recharged (blue) carbon electrodes for Mg/O$_2$ cell using 4:1 PhMgCl:Al(OPh)$_3$/THF electrolyte.

Figure 3.15 shows X-ray diffraction patterns collected from discharged, recharged, and control electrodes. Patterns were collected without exposure to air using an airtight sample holder. The MgO (200) peak appears in the XRD patterns of the discharged and recharged electrodes, but this peak is absent from the control-electrode XRD pattern, confirming that no discharge product forms when the cell is held at open circuit. In the recharged positive electrode, the peak attributed to crystalline MgO is significantly diminished, suggesting substantial, but not complete, dissolution of MgO during charging. No peaks corresponding to crystalline MgO_2 were observed in any electrode.
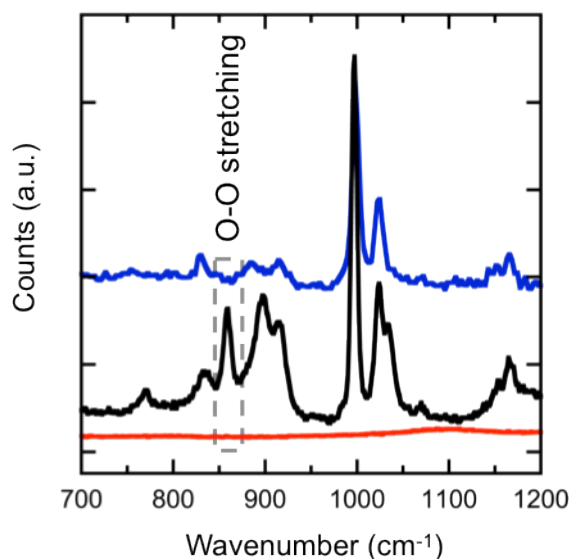
Figure 3.16 Raman spectra collected from control (red), discharged (black) and recharged (blue) carbon electrodes for Mg/O_2 cell using 4:1 $PhMgCl:Al(OPh)_3/THF$ electrolyte.

Absence from the XRD patterns does not preclude the presence of amorphous MgO_2, however. Figure 3.16 shows Raman spectra collected from the discharge product, the product remaining after recharge, and the control electrode. The oxygen electrodes were placed in an airtight RS sample holder with quartz windows. Several spectra were collected from reference

samples to identify the peaks in the discharge-product spectrum. Representative Raman spectra for isolated discharged and control electrodes, electrolyte, MgO_2 ($MgO_2 \bullet xMgO$, x = 24-28%, Sigma-Aldrich, USA) and MgO (STREM, USA) powders are presented in Figure 3.17. Simple background removal has been performed on the spectra to minimize artifacts arising from fluorescence.
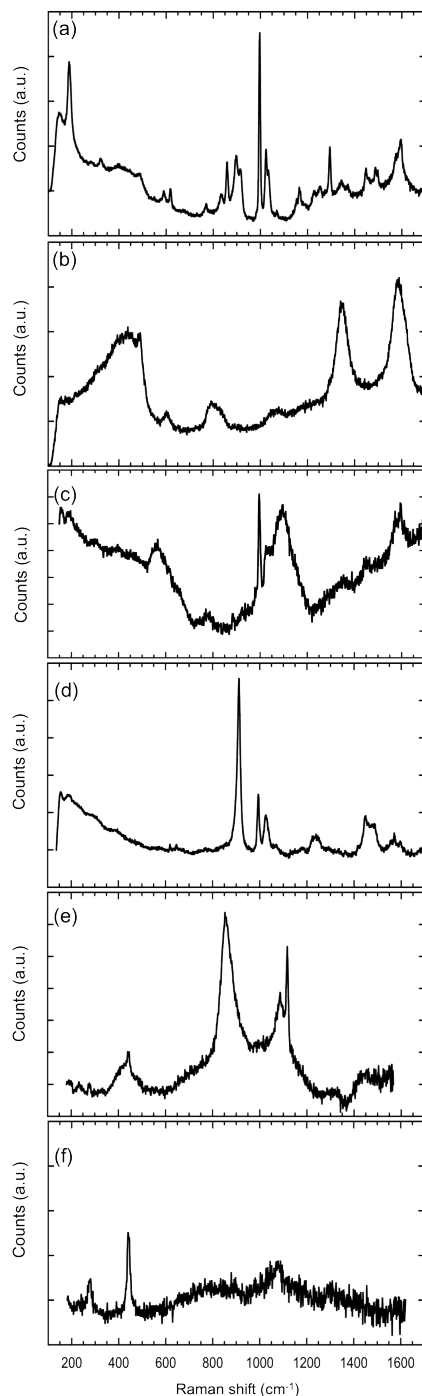
Figure 3.17 Raman spectrum collected from discharge phase. (b) Raman spectrum collected from a positive electrode without discharge phase. (c) Raman spectrum collected a carbon electrode soaked in electrolyte and dried without a THF rinse. (d) Raman spectrum collected from liquid electrolyte sample. (e) Raman spectrum collected from MgO_2 powder. (f) Raman spectrum collected from MgO powder. Peaks observed in MgO and MgO_2 powder are indexed to $Mg(OH)_2$, which forms when MgO is exposed to moisture.[124]

The sharp peaks between 870 and 1100 cm^{-1} all can be assigned to residual electrolyte with THF solvent.[125] The peak around 200 cm^{-1} can be attributed to Mg-Cl stretching.[126]
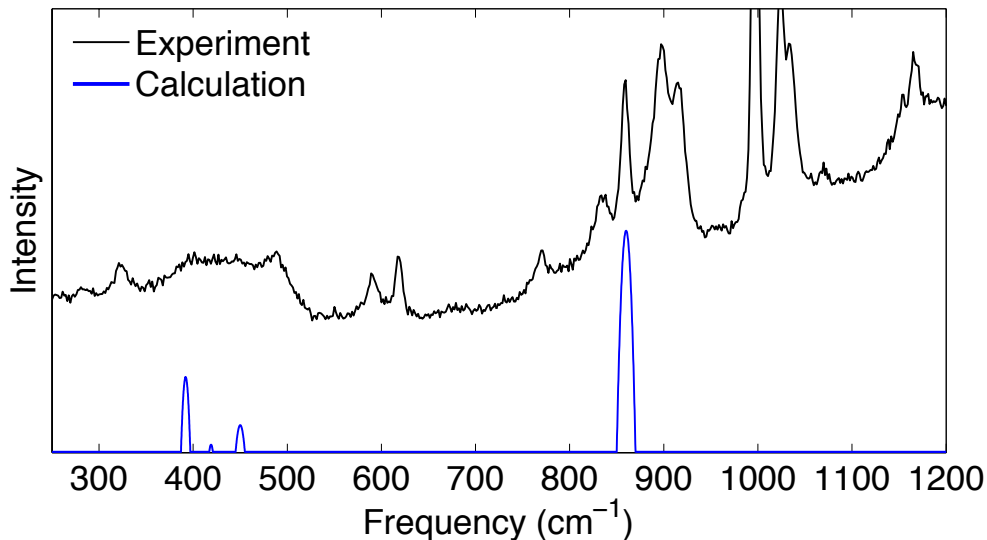
Figure 3.18 Calculated Raman spectrum (blue line) and comparison to measurements (black line) performed on the positive electrode of a discharged Mg/O$_2$ cell using 4:1 PhMgCl:Al(OPh)$_3$/THF electrolyte.

In particular, the peak near 860 cm^{-1} was confirmed to correspond to O-O stretching in MgO$_2$ by density-functional-theory calculations (Fig. 3.18), and has been attributed to O-O stretching in other peroxide compounds.[127] (MgO does not yield a first-order Raman signal and therefore cannot not be detected by RS.[128]) The observation of a MgO$_2$ peak in the Raman spectrum confirms the presence of amorphous MgO$_2$ in the discharge product and is consistent with the excess oxygen observed by AES. In the recharged positive electrode the peak attributed to O-O stretching is not observed, supporting the notion that MgO$_2$ decomposes preferentially during recharge, in agreement with the 1:1 Mg:O stoichiometry measured by AES (Fig. 3.14).

In summary, the present study has probed the reaction pathway and characterized the discharge product in a reversible Mg/O$_2$ cell. The cell produces a mixed-phase product that comprises crystalline MgO with domains of amorphous MgO$_2$; this product forms after

electrochemical superoxide formation from O_2, through chemical precipitation and disproportionation steps. Importantly, several aspects of Mg/O_2 electrochemistry appear to differ fundamentally from alkali-metal/O_2 systems. A discharge product comprising large, faceted particles was observed, but was seen only in areas of the electrode that were in close proximity to gas, suggesting that O_2 transport limits cell capacity. Several techniques probed the discharge-product composition, revealing that the product comprises roughly 70% MgO and 30% amorphous MgO_2 on a volumetric basis. The recharged positive electrode contained a small amount of residual MgO, suggesting that MgO_2 decomposes first during charging, followed by more limited MgO decomposition.

3.4 Conclusion

The combination of a multi-valent metal with an air-breathing positive electrode portends a secondary battery system with extremely high energy density. The superoxide-controlled discharge voltage, low capacity, and limited cycle life observed for the Mg/O_2 cell presented here suggest that additional development is needed to realize these advantages. Further electrolyte development could increase apparent capacity and rate performance. In addition, circumventing the multi-step discharge mechanism in favor of direct electrochemical MgO_x formation would lead to cells with far higher energy density.

Chapter 4 A Magnesium/Oxygen Battery Based on the MACC Electrolyte

4.1 Introduction

Prior to the invention of the all-inorganic Mg electrolytes in 2013, Grignard-reagent-based electrolytes were thought to be the only class of non-aqueous solutions capable of reversible Mg deposition.[26] But Grignard solutions exhibit low conductivity (< 1 mS/cm) and need to be supported by Lewis acids to achieve oxidative stability above 1V vs. Mg/Mg^{2+}.[79, 129-130] Also, Grignard reagents are generally pyrophoric,[131] so an electrolyte without them could have practical advantages. Simple Mg salts are known to dissociate poorly in organic solvents, possibly due to the high charge density on the Mg ion.[132-134] Undissociated Mg salts cannot enable reversible Mg deposition and are therefore unsuitable as electrolytes.

In 2013, a fully inorganic electrolyte that does not contain any Grignard reagents was realized by reacting $MgCl_2$ with $AlCl_3$ (Magnesium Aluminum Chloride Complex, MACC) and the oxidative stability was found to be 3V vs. Mg/Mg^{2+},[135] comparable to previously developed electrolytes. Complicated conditioning procedures were needed to achieve high coulombic efficiency, and were discussed separately.[136] The reported conditioning method consists of repated voltage cycling at low scan rates (5 mV/s) across a voltage window from –1.2 to 2.1V vs.

Mg/Mg^{2+}.[137] For a 1.5mL sample of 30mM MACC/DME electrolyte, many (> 100) cycles were needed to achieve > 99% coulombic efficiency for Mg plating and stripping. At these low scan rates, the cycling methods requires very long conditioning times (at 5 mV/s, the 3300 mV window takes about 20 minutes to cycle around just once, so 100 cycles requires at least a day and a half of conditioning). In this chapter, we present a scalable electrolysis method that is able to condition MACC/DME electrolyte in bulk quantities (> 20mL) very rapidly.

The conditioning method merits study since it is not clear why it is needed in the first place. Barile *et al*. reported that the Mg:Al ratio (as measured by elemental analysis) increases with conditioning. Irreversible co-deposition of Mg and Al was observed on the working electrode of the conditioning apparatus.[136] Furthermore, changing the electrodes was found not to change the properties of the conditioned electrolyte, suggesting that the conditioning process does not affect the electrode/electrolyte interface.[136] Recently, it was reported that conditioning MACC/THF increases the concentration of free Cl$^-$ in the solution, and that this increased Cl$^-$ might aid in depassivating the Mg surface. [137] Theoretical studies have focused on identifying the stable electroactive species in the electrolyte and speculated that conditioning stabilizes charged species in solution.[138]

The same all-inorganic salt electrolyte concept has been demonstrated with other Mg salts such as $MgCl_2$-$Mg(HMDS)_2$ and $MgCl_2$-$Mg(Tf_2N)$.[139-141] Similar conditioning steps were applied in order to achieve high coulombic efficiency (>99%) for these solutions.

In this chapter, the synthesis and bulk conditioning of the MACC/DME electrolyte and Mg/O$_2$ cells using the MACC/DME electrolyte are discussed. We report a high-capacity Mg/O$_2$ battery that uses the MACC electrolyte in DME.[135-137, 142] Room-temperature Mg/O$_2$ cells using MACC/DME electrolyte exhibit capacities that are similar to previously reported high-temperature Mg/O$_2$ cells using Mg salt electrolytes[54-55] and much higher than the capacities

observed using a modified Grignard electrolyte.[143] A wide range of discharge rates (0.02-1 $mAcm^{-2}$) is explored. The rechargeability of the battery is discussed in relation to the surface films that form on the anode and cathode as a function of time and applied current. The discharge product is identified as consisting of $Mg(ClO_4)_2$ and $MgCl_2$. The effect of discharge rate on capacity and discharge voltage are reported.

4.2 Experimental Methods

Experimental methods similar to those described in Chapter 3 were used to assemble and test Mg/O_2 cell performance and identify the discharge product chemistry. In addition to the previously discussed methods, Electrochemical Impedance Spectroscopy (EIS) and X-ray Photoelectron Spectroscopy (XPS) experiments were performed.

4.2.1 Electrochemical Impedance Spectroscopy (EIS)

EIS was performed with a BioLogic SP-200 potentiostat using a voltage amplitude of 10mV around the open-circuit potential in the frequency range 100 mHz – 7 MHz. During the OC hold, EIS measurements take 2 minutes to run for the frequency range stated. Then, the cell is rested at open circuit (zero current) for 8 minutes. Then, another EIS measurement is taken. Therefore, during the OC hold phase EIS spectra is recorded every 10 min. The full duration of the OC hold was 3 hours (18 cycles of EIS).

4.2.2 X-ray Photoelectron Spectroscopy (XPS)

XPS was performed with a Kratos Axis Ultra using the monochromated Al source. The beam size was 2 mm x 1 mm, and the source voltage and emission current were 14 kV and 8mA, respectively. Survey spectra were collected in the range of 0 – 1200 eV with a step size of 1 eV. Mg 2p spectra were collected in the range of 42 – 58 eV with a step size of 0.1 eV and 20 sweeps

were collected in the same range to improve the signal-to-noise ratio. The charge compensator was turned on for all measurements to inhibit charging effects. Samples were exposed to air briefly (< 2 min) during sample loading.

4.2.3 Electrolyte Synthesis and Conditioning

The MACC electrolyte was prepared using $MgCl_2$ (99.99%, Sigma Aldrich, USA) and $AlCl_3$ (99.999%, Sigma Aldrich) powders, and DME (99.5%, anhydrous, Sigma Aldrich, USA) in the glovebox. $MgCl_2$ powder (0.9521g) was added into the reaction vessel. 40mL of DME was added to the $MgCl_2$ powder in the reaction vessel and stirring was started at 300 rpm. The resulting solution is 0.25M on a Mg basis and 0.125M on a Al basis. The $AlCl_3$ powder (0.6667g) was added to the $MgCl_2$/DME solution as it was being stirred. The solution was then capped and heated to 50 °C for 2 hours or until the solution turned completely translucent. The resulting solution is 0.25M on a Mg basis and 0.125M on a Al basis. The liquid temperature was measured using a thermometer every 30 min. Once the solution was clear in appearance, the heat was turned off and the solution was stirred overnight at room temperature. The resulting solution was then filtered with a disposable filter with an average pore size of 0.5 μm. The filtered residue presumably consists of a mixture of $MgCl_2$ and $AlCl_3$. The weight of the residue was not measured. The concentrations reported for the electrolyte assume that all of the salts stayed in solution.

The conditioning cell for the MACC electrolyte is a 20mL beaker cell with three electrode openings in the cap. Counter and reference electrodes were Mg strips (99%, Goodfellow, U.S.), and two working electrodes were incorporated: a Pt wire (99.997%, Alfa

Aesar, U.S.) for cyclic voltammetry measurements and a Mg strip for the electrolytic conditioning steps.

Cyclic voltammetry was performed by starting at 1V vs. Mg/Mg^{2+} and sweeping to lower voltages at a rate of 10mV/s. The low-voltage cutoff for the window was extended until a sharp increase in the current indicated Mg deposition. For a freshly-prepared electrolyte, the initial deposition overpotential could be as high as 2V.

4.3 Results and Discussion

4.3.1 Electrolyte Conditioning and Characterization

The CV for the as-prepared MACC/DME electrolyte can be seen in Figure 4.1. The overpotential for deposition is around –1V vs. Mg/Mg^{2+} and the coulombic efficiency is below 10%.
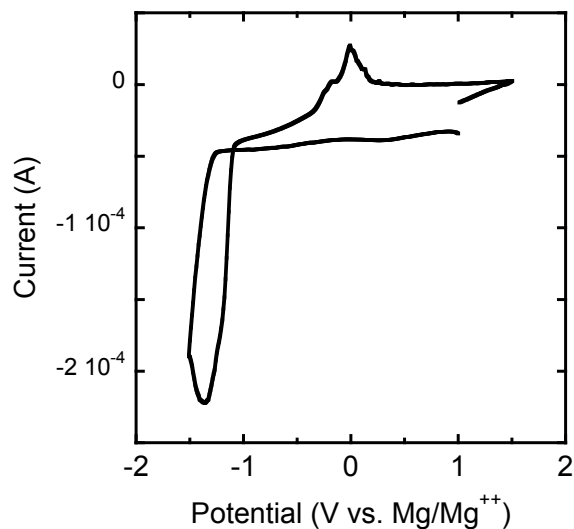
Figure 4.1 CV of as-prepared 0.25M MACC in DME, on a Pt wire working electrode at room temperature. Counter and reference electrodes are Mg.

After recording the CV for the as-prepared MACC/DME, electrolysis was performed after replacing the Pt wire working electrode by a Mg strip. The voltage was kept constant at a 0.5V below the deposition overpotential observed for the as-prepared material. For example, for the MACC/DME electrolyte whose voltammetric response is shown in Figure 4.1, the first conditioning step was performed at −1.5V vs. Mg/Mg^{2+}. A representative chronoamperometric curve for the first constant-voltage electrolysis of the material that produced the data in Figure 4.1 is presented in Figure 4.2.
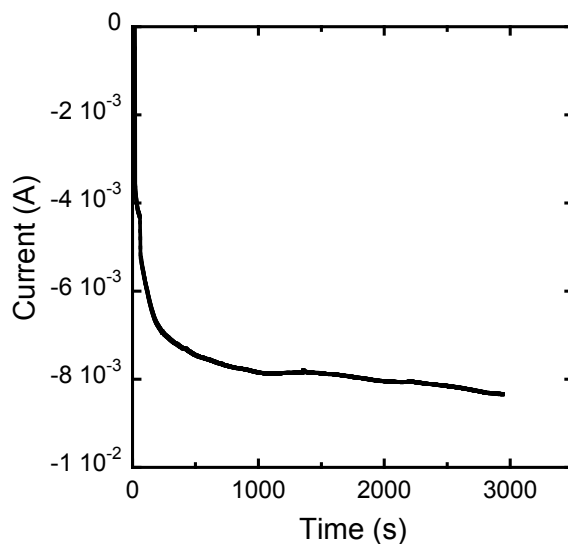
Figure 4.2 Representative current vs. time plot for the conditioning step of MACC/DME electrolyte. Counter, working and reference electrodes are Mg strips.

Constant-voltage electrolysis was stopped after 20 C of charge is passed, which was ~1 C/mL for the solutions prepared here. The Mg strip was removed and replaced with Pt wire for a cyclic voltammetry measurement, after which the Mg strip was returned to the cell. Conditioning steps were continued until the CV showed that the deposition overpotential was reduced to < 0.5 V and the coulombic efficiency was > 95%. The effect of conditioning by electrolysis is shown in Figure 4.3 as a function of the cumulative charge passed during the conditioning steps. Note that the deposition overpotential decreases significantly as electrolysis proceeds. The final CV after 120 C of conditioning (blue CV curve) exhibits a deposition overpotential of –0.5V vs. Mg/Mg^{2+} and a coulombic efficiency of 96.5%. This electrolyte is then stored in a clean container to be used in Mg/O_2 cell testing experiments.

The conductivity of the conditioned MACC/DME electrolyte was measured using a Mettler Toledo SevenMulti conductivity meter at room temperature. The electrolyte was exposed to air for a very short period of time (< 10 seconds) while taking the conductivity measurement.

The conductivity of the conditioned MACC/DME electrolyte was measured as 2.21 mS/cm, about twice that of 4:1 PhMgCl:Al(OPh)$_3$/THF, which was reported as 1.24 mS/cm.[53]
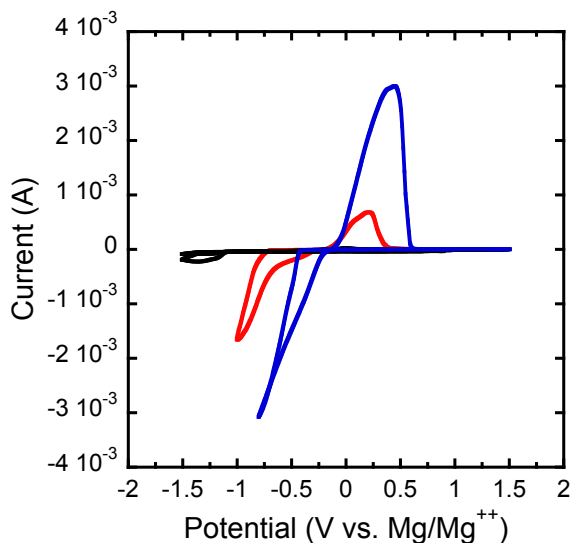
Figure 4.3 CV of 0.25M MACC/DME electrolyte, as-prepared (black), after 60C of conditioning (red) and after 120C of conditioning (blue). Counter and reference electrodes are Mg strips. Working electrode is Pt wire.

4.3.2 Electrochemical Testing

Conditioned MACC electrolyte was used in Mg/O$_2$ cell discharge experiments. To compare the modified Grignard electrolyte from Chapter 3 and the conditioned MACC electrolyte, a discharge experiment was performed at a superficial discharge rate of 5μA/cm^2. Figure 4.4 shows a comparison of the two electrolytes under the same experimental conditions. The Mg/O$_2$ cells using MACC reach similar OCVs of 2.0 ± 0.1 V. The discharge-voltage plateau for the MACC electrolyte is much higher and discharge is sustained for a longer time period, confirming a much higher capacity. Eventually, the discharge experiment for the MACC electrolyte using the discharge rate of 5 μAcm^{-2} was stopped because the discharge time

exceeded the experimental controls. (Figure 4.4) The reason for the large difference in discharge capacities observed for the two electrolytes could be due to higher conductivity of the MACC/DME electrolyte or the higher solubility of O_2 in DME compared to THF. [117-118]
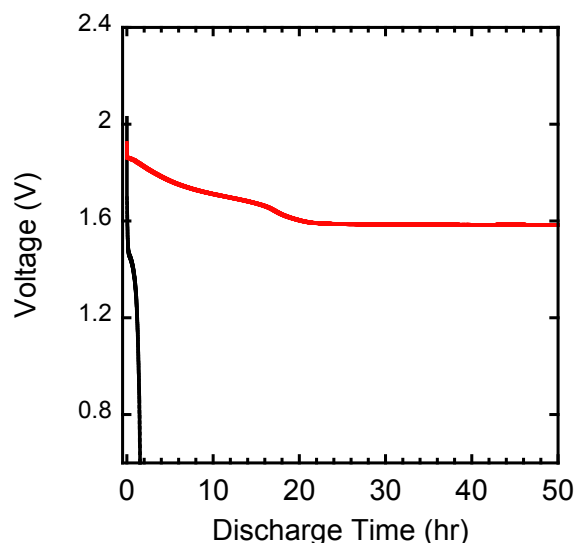
Figure 4.4 Voltage vs. discharge time for Mg/O_2 cells using 4:1 PhMgCl:Al(OPh)$_3$/THF electrolyte (black) and MACC/DME electrolyte (red). Discharge rate is 5 μAcm^{-2} (superficial).

To check that the discharge capacity arises from reaction with O_2, a control cell was assembled in which the cell was not exposed to O_2. Figure 4.5 compares the discharge capacities of cells with and without O_2 exposure. The cell potential for the cell with no O_2 exposure decreases very sharply upon initiation of discharge, whereas the Mg/O_2 cell exhibits a discharge plateau before a gradual decrease in voltage.
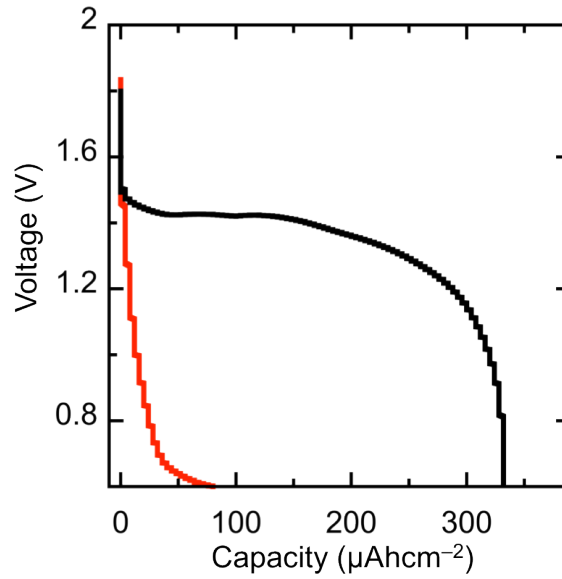
Figure 4.5 Discharge curves for for Mg/O$_2$ cells using MACC/DME electrolyte with (black) and without (red) O$_2$ exposure.
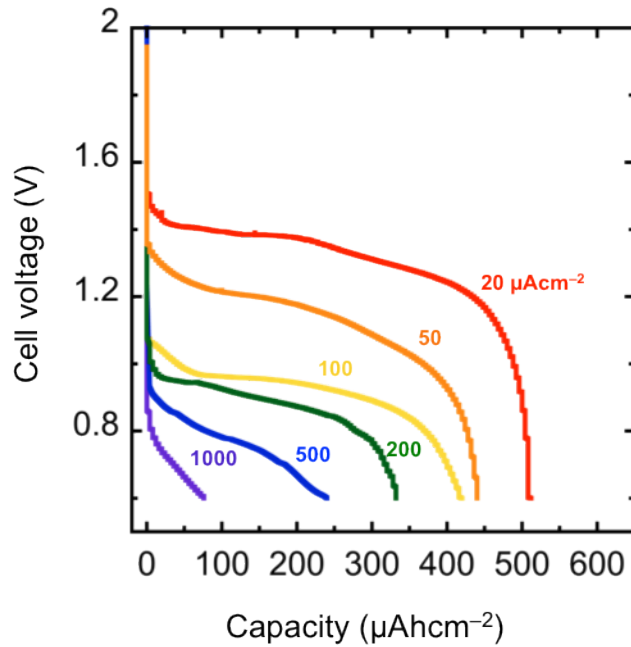
Figure 4.6 Representative discharge curves for Mg/O$_2$ cells using MACC/DME electrolyte over a range of discharge rates (20-1000 μAhcm^{-2}).

The rate capability of a battery is important when deciding whether it can be incorporated into a vehicular application. Using the MACC/DME electrolyte has allowed us to discharge Mg/O$_2$ cells at a wide range of discharge rates (0.02–1 mAhcm^{-2}). These rates are comparable to rates at which Li/O$_2$ cells are tested so it offers the possibility of a direct comparison to the rate capability of Li/O$_2$ chemistry. Figure 4.6 shows representative discharge curves for discharge rates of 20–1000 µAcm^{-2}. The slowest discharge rate was chosen to complete the measurement within 24 hours. As expected, the discharge voltage plateau is higher for slower rates (smaller current) and the capacity decreases with increasing rate. Several experiments were performed at each discharge rate to gather information about the rate performance of Mg/O$_2$ cells. Figure 4.7(a) and 4.7(b) show discharge capacity and cell voltage at 50% depth-of-discharge as a function of discharge rate and include data collected from 28 independent Mg/O$_2$ cells.
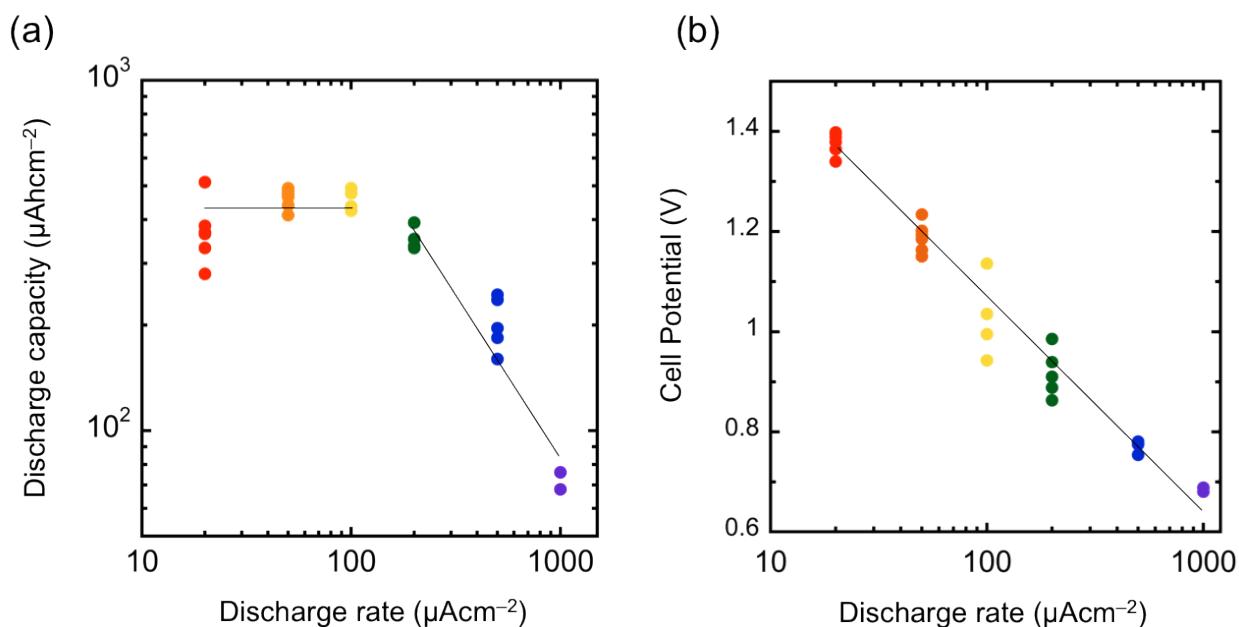
Figure 4.7 (a) Capacity per geometric electrode achieved at the 0.6V cutoff potential as a function of discharge rate. **(b)** Cell potential at 50% depth-of-discharge as a function of discharge rate.

Figure 4.7 (a) shows that discharge rate does not significantly affect capacity at rates below 0.01 mAcm^{-2}. Capacity decreases with increasing discharge rate at rates above 0.02 mAcm^{-2}.

Peukert's law is an empirical relation that relates the capacity of a cell with the discharge current.[98] The Peukert coefficient (k) can be compared across different battery chemistries to inform the capability of the cell to retain its capacity with increasing rate An ideal battery would have a k of 1, meaning that the capacity of the cell would remain the same at each discharge rate, but the second law of thermodynamics requires k to be larger than 1. The capacities observed above 0.02 mAcm^{-2} for Mg/O$_2$ cells using MACC/DME electro   lytes   follow   a   power-law dependence on the discharge current. The calculated Peukert coefficient is 1.9 with a reference capacity of 91 μAhcm^{-2} at 1 mAcm^{-2}. Compared to Li/O$_2$ (k=1.6)[98] chemistry, Mg/O$_2$ chemistry shows low rate capability. The transition from k=1 (below 0.01 mAcm^{-2}) to k>1 (above 0.02 mAcm^{-2}) is commonly observed for metal/O$_2$ batteries.[110] Figure 4(b) shows the cell potential at 50% depth-of-discharge (DOD) vs. discharge rate for Mg/O$_2$ cells. Following an analysis similar to that of Griffith et al.,[98] data reveals a Tafel slope of 4.9 V^{-1} and an exchange-current density of 1.6 μAcm^{-2}(superficial).

4.3.3 Rechargeability and Impedance Measurements

Experiments with Mg/O$_2$ cells using MACC/DME electrolyte showed that the cells did not exhibit any appreciable recharge capacity. Figure 4.8 shows the discharge and recharge behavior for a Mg/O$_2$ cell run at 50 μAcm^{-2}. While the cell exhibits a considerable discharge capacity, recharge at the same rate is not possible.
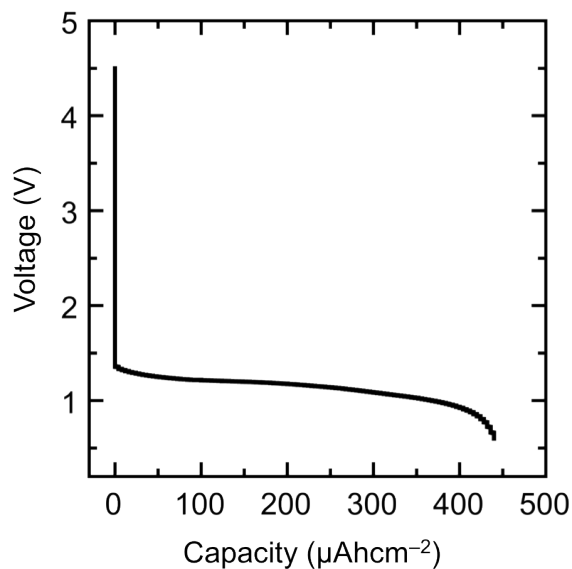
Figure 4.8 Discharge and recharge curve for a Mg/O$_2$ cell using MACC/DME electrolyte. Rate is 50 μAcm^{-2} (superficial).

To understand the reason for the lack of recharge capacity in the MACC/DME electrolyte, the evolution of interfacial resistances as a function of time and applied current was studied with the help of electrochemical impedance spectroscopy (EIS).
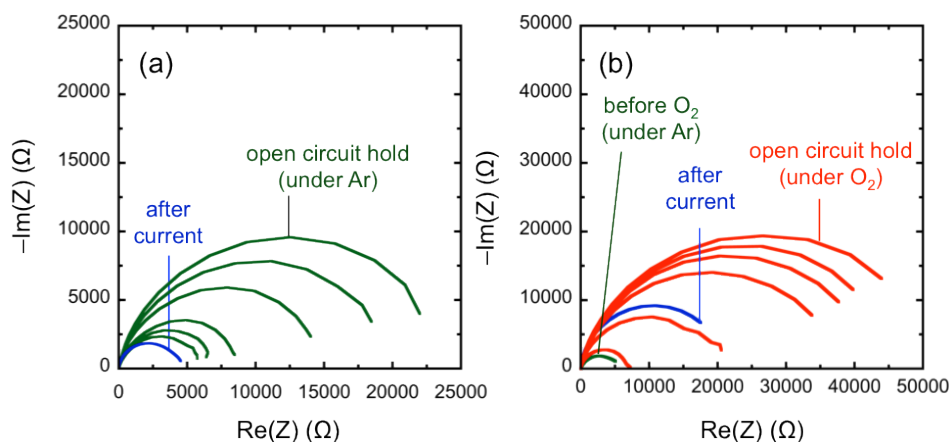
Figure 4.9 (a) EIS spectra for a Mg/Mg cell using MACC/DME electrolyte under Ar during OC hold (green) and after passing 1.4C through cell (blue). (b) EIS spectra for a Mg/Mg cell using MACC/DME electrolyte before O$_2$ exposure (green), under O$_2$ during OC hold (red), and after passing 1.4C through cell (blue). (c) Equivalent circuit model fit for R$_{SEI}$ during OC

64

holds for Mg/Mg cells under Ar (green circles) and under O_2 (red squares). The EIS spectra during OC holds were taken every 10 minutes for a total of 3 hours. In Fig. 2(a) and 2(b), EIS data taken at 10, 20, 50,100, 150 and 180 minutes are plotted.

A series of experiments was devised to identify the effects of OC holds and applied currents on Mg anode surfaces. Figure 4.9(a) shows Nyquist plots gathered from a symmetric Mg/Mg cell under Ar. The cell is kept at OC and an EIS measurement is taken every 10 minutes to identify how impedance changes as a function of time. The increase in the impedance of the Mg/Mg cell over time could be associated with the formation of a non-passivating solid electrolyte interface (SEI) film. After the OC hold, 1.4C of charge was passed through the cell and another EIS data set was recorded (blue curve). The decrease in the impedance after applied current could be explained by the dissolution of the SEI film on the Mg anode. Figure 4.9(b) presents a similar experiment to Figure 4.9(a), but with exposure of the cell to O_2 gas throughout the OC hold interval. The green curve shows EIS data collected before O_2 exposure and, again, impedance grows as a function of time during the OC hold under O_2 (red curves). After 1.4C charge was passed through the cell, the impedance again decreased (blue curve).

An equivalent circuit model (ECM) was used to fit the EIS data in Figures 4.9(a) and 4.9(b) to identify and isolate the effect of O_2 exposure for a Mg surface. The initial equivalent circuit model (ECM) was chosen to represent the symmetric Mg/Mg cells using the formulation of Huggins.[144]

Model I
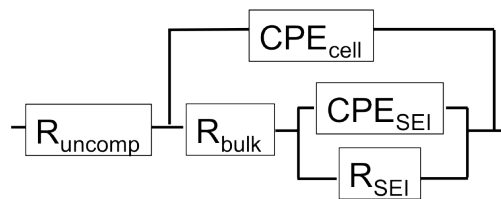
In the ECM, R_{uncomp}, R_{bulk}, R_{SEI} represent the uncompensated resistance of the cell setup, the resistance associated with the electrolyte and the resistance associated with the electrode/electrolyte interface, respectively. Constant phase elements (CPEs) were used since EIS curves are not perfect semicircles. The non-ideal capacitance could be explained by a dispersion of the time constants associated with the processes or porous structure of the interfacial layers.

The EIS data collected from Mg/Mg cells was then modeled using a simplified ECM (model II) that includes a R_{bulk} element in series with a parallel CPE-R circuit that can be used to model the semicircles observed. In this model, the contribution of the uncompensated resistance and the cell capacitance are ignored since they are small compared to the rest of the components in model I. The extra complexity of model I does not improve the interpretation of the data.
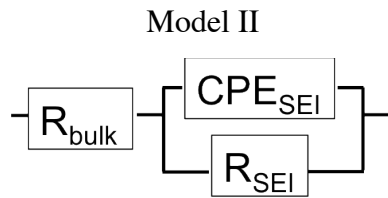
Model II

The ECM fits for R_{SEI} (using model I) and R_{SEI} (using model II) are plotted in Figure 4.10 and Figure 4.11. The evolution of R_{SEI} (from model I) and R_{SEI} (from model II) with time closely resemble one another. Furthermore, ECM fits using model I reveal that R_{bulk} (~1000Ω) and R_{uncomp} (~20Ω) are an order of magnitude lower than R_{SEI} (5000–50000Ω, varies with time), confirming that SEI formation dominates the cell impedance. CPE_{cell} (< 10^{-6} F/cm^2) fit from model I is also negligible. Therefore simplifying model I and using model II is justified.
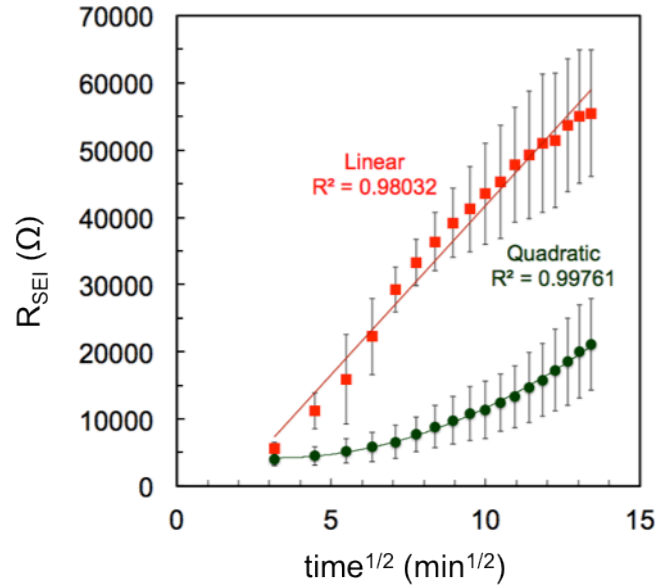
Figure 4.10 Trendline fits for R_{SEI} during open circuit holds for Mg/Mg cells using MACC/DME under Ar (green circles) and under O_2 (red squares) as a function of time$^{1/2}$. The O_2 data was fit with a linear fit, indicating diffusion limited film growth. The Ar data was fit with a quadratic equation but since the x-axis is square root of time, the fit indicates a linear growth rate for the SEI film on the Mg anode during hold under Ar. This figure was generated using model I.
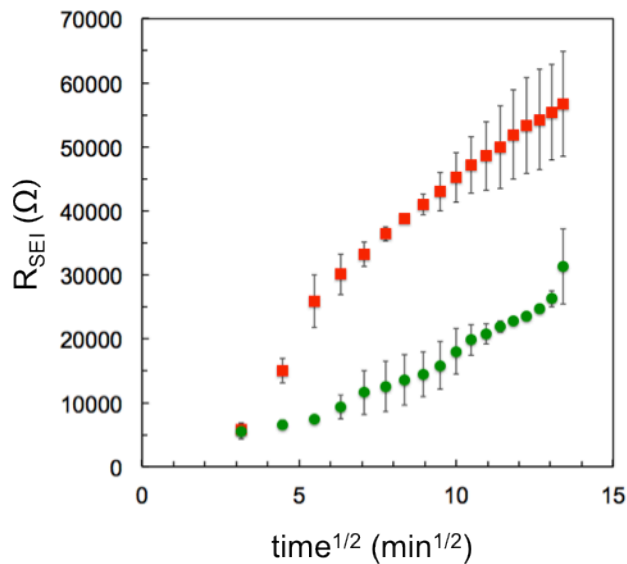
Figure 4.11 ECM fits for R_{SEI} during open circuit holds for Mg/Mg cells using MACC/DME under Ar (green circles) and under O_2 (red squares) as a function of time$^{1/2}$. This figure was generated using model II.

Figure 4.10 summarizes the increase in the resistance associated with the SEI as a function of time. R_{SEI} increases linearly with respect to the square root of time for Mg surfaces exposed to O_2, indicating that there might be a diffusion-limited film growth. There is SEI film formation under both Ar and O_2 atmospheres, but the presence of oxygen appears to induce more rapid film formation on the Mg surface.

Taking into account the ideality factor (α) of CPE_{SEI}, one can approximate the pseudo-capacitance associated with the CPE element. The capacitance value for CPE_{SEI} is on the order of 10^{-6} F/cm^2, a magnitude consistent with an interfacial layer at the electrode/electrolyte interface.[145]
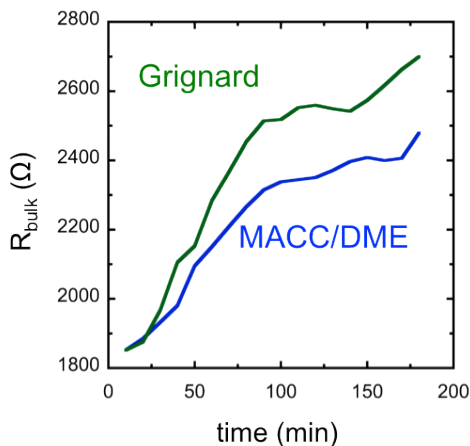
Figure 4.12 Normalized R_{bulk} for a Mg/Mg cell that is exposed to O_2 as a function of time for MACC/ DME(blue) and modified Grignard (green) electrolyte.

The evolution of R_{bulk} (resistance element associated with electrolyte) could give insight into the chemical stability of the electrolyte in the presence of O_2 exposure. Symmetric Mg/Mg cell experiments were run with the modified Grignard electrolyte previously used for Mg/O_2 discharge experiments[53, 143] in addition to the MACC/DME electrolyte studied here. The rate of

increase for R_{bulk} is larger for the modified Grignard electrolyte than MACC/DME. (Figure 4.12)

Therefore, MACC/DME is a more stable electrolyte than Grignard electrolytes when exposed to

O_2. More experiments, such as cyclic voltammetry with O_2-saturated electrolytes, are needed to

confirm the chemical stability of Mg electrolytes in the presence of O_2.
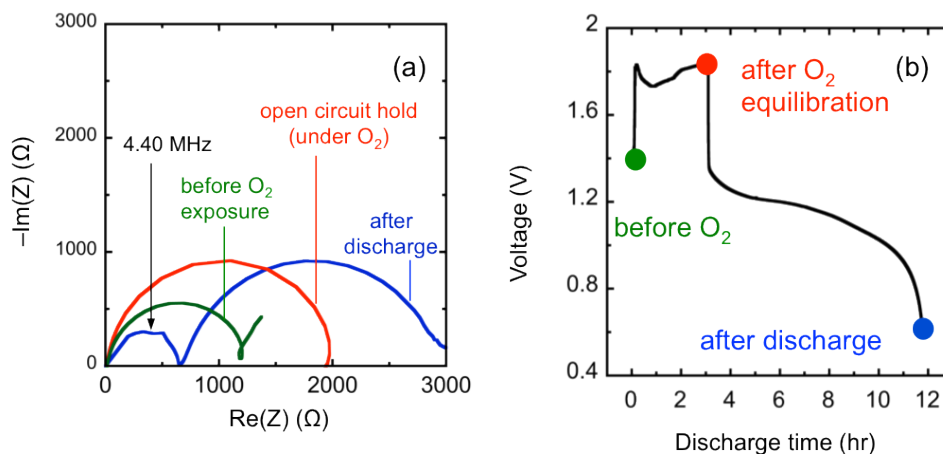
Figure 4.13 (a) EIS spectra for a Mg/O2 cell using MACC/DME electrolyte before O_2 exposure (green), after OC hold under O_2, and after discharge (blue.) (b) A representative discharge curve showing the stage in the experiment that the EIS spectra in Figure 4.13(a) correspond to.

The experiment depicted in Figure 4.13 builds on the previous symmetric Mg/Mg cell

EIS experiments to isolate the effect of the porous-carbon positive electrode in a full Mg/O_2 cell.

Similar to the symmetric Mg/Mg cells, the exposure of O_2 induces an increase in impedance of

the cell, likely caused by an SEI film formation on the Mg anode. After the cell is discharged

(blue curve), there is a new interface formed in the cell, indicated by a new semicircle

characterized by a frequency of 4.40MHz and with a capacitance value on the order of 10^{-12} F.

The emergence of this semicircle can be tracked by partial discharge experiments and the

semicircle appears to grow as discharge progresses. (Figure 4.14)
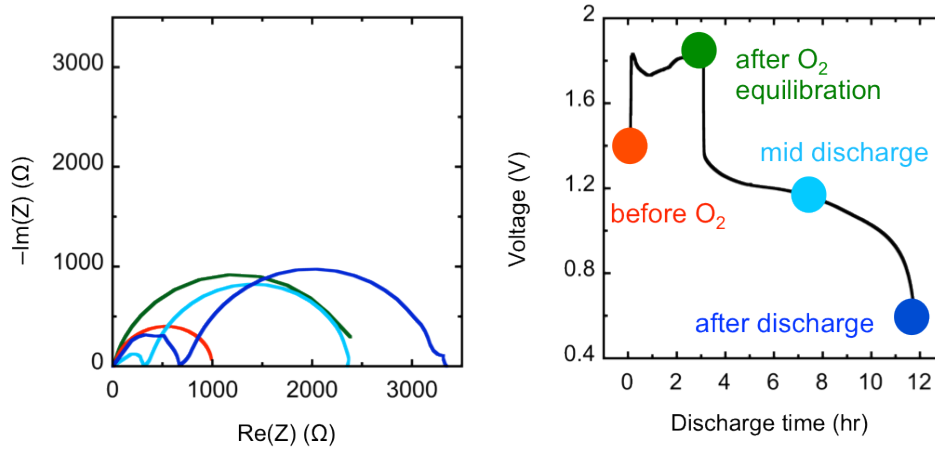
Figure 4.14 EIS measurements for a Mg/O$_2$ cell using MACC/DME electrolyte before O$_2$ exposure (red), after O$_2$ equilibration (green), middle of discharge (light blue) and end of discharge (blue). The measurement points are labeled in the right figure depicting a representative Mg/O$_2$ discharge experiment.

Model III
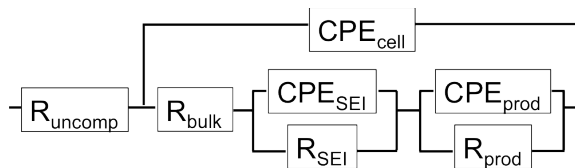
In non-symmetric Mg/O$_2$ cells, a new semicircle appears at the end of discharge which should be accounted for with another parallel CPE$_{prod}$-R$_{prod}$ circuit in series with the previous model I . Fitting the data with model III, R$_{comp}$ and CPE$_{cell}$ are again small and negligible compared to other cell components. Therefore, model III is simplified to model IV.

Model IV
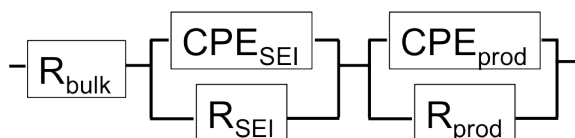
This new parallel CPE_{prod}-R_{prod} circuit accounts for the interface created as the discharge product gets deposited onto the carbon cathode surface. When the CPE_{prod} value is analyzed, it is on the order of 10^{-12} F/cm^2 which confirms that this new semicircle is assciated with a bulk discharge product layer.[145] R_{prod} is on the order of 600Ω which is significant when the entire cell impedance value is on the order of 3000Ω.

The EIS data for Mg/O$_2$ cells were also fit using the Huggins model (model III) and the simplified model IV. The CPE_{prod} and R_{prod} values were within 20% for both cases. Therefore the simplified model III is a suitable circuit to model the EIS data.

Overall, symmetric Mg/Mg cell EIS measurements show that SEI film formation is the largest contributor to impedance at the Mg/electrolyte interface. The presence of O$_2$ accelerates the formation of the SEI film, similar to the "cross-over effect" observed in metal/O$_2$ chemistries. The EIS spectra for the Mg/O$_2$ cell show that the discharge product formation significantly increases the impedance of the cell and introduces a new interface. The impedance associated with this new interface could be another reason that the rechargeability of the cell is limited.

4.3.4 Discharge Product Characterization

The chemistry of the discharge product is another factor in the rechargeability of the Mg/O$_2$ cell. The discharge product of Mg/O$_2$ cells using MACC/DME electrolyte had been analyzed using the same methods described in Chapter 3 and additional characterization tools.
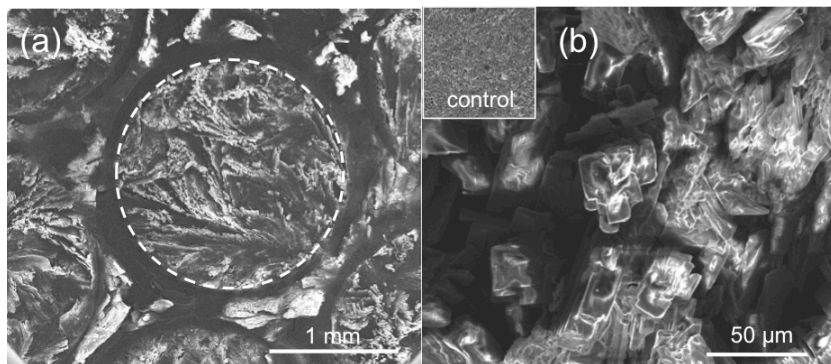
Figure 4.15 SEM images of positive electrode at the end of first discharge for Mg/O$_2$ cell using MACC/DME electrolyte at (a) low magnification and (b) high magnification. The inset image in (b) shows a control electrode exposed to O$_2$ in a cell held at open circuit. Discharge rate is 50 μAcm^{-2} (superficial). The dashed circles represent boundaries of the regions that were directly exposed to O$_2$ through perforations in the Pt-coated current collector.
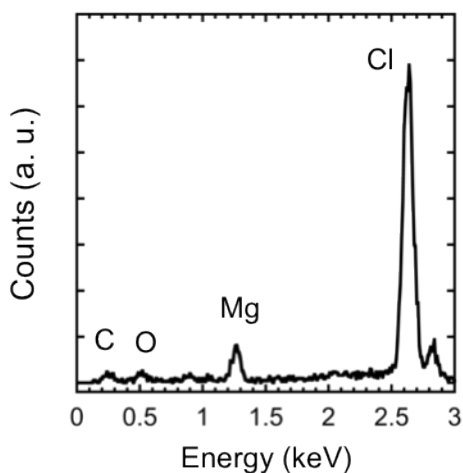
Figure 4.16 EDS spectra of discharge product for Mg/O$_2$ cell using MACC/DME electrolyte.

Figure 4.15 shows SEM images of the discharged cathode in a Mg/O$_2$ cell using MACC/DME electrolyte. In comparison to the SEM images of the discharged cathode with PhMgCl:Al(OPh)$_3$/THF electrolyte, it can be observed that the surface coverage of the discharge product is increased. This observation is in agreement with the increased capacity observed with MACC/DME electrolyte. Figure 4.15(b) shows that particles are faceted and seem to be stacked

on top of one another. Figure 4.16 shows the EDS spectra collected from the discharge product. There is a strong signal for Cl and weaker signals for Mg, O, and C.

In first step, XRD was used to analyze the composition of the discharge product. Figure 4.17 shows the XRD spectra for discharged and control carbon electrodes. Peaks for $MgCl_2$ and $Mg(ClO_4)_2$ can be observed in the discharged cathode whereas the peaks for these compounds are absent in the control cathode. The anhydrous $Mg(ClO_4)_2$ compound is known to be unstable and could decomposes into $MgCl_2$ and O_2.[146] So the inhomogenous discharge product at room temperature could be explained by formation $Mg(ClO_4)_2$ followed by decomposition into $MgCl_2$.
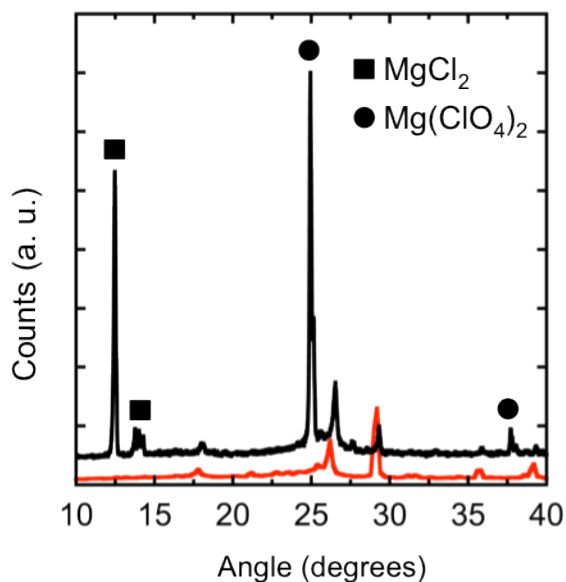
Figure 4.17 XRD pattern of control (red), discharged (black) carbon electrodes.

Figure 4.18 shows the Raman spectra for the discharged and control carbon electrodes. There are many peaks in the discharge product that are also observed in the electrolyte despite holding the carbon cathode under vacuum for 30 min. Most of the peaks in the electrolyte can be attributed to the solvent (DME). In addition, peaks that are attributed to $MgCl_2$ (212 cm^{-1}) and

AlCl$_3$ (330 cm^{-1}) can be observed in the discharge product. However, the peak for ClO$_4$ vibration is only observed in the discharge product, indicating that discharge process results in formation of Mg(ClO$_4$)$_2$. However, it is important to note that the Raman spectra collected from the discharge product indicate that the discharge product is not homogenous. For example, figure 4.19 shows Raman spectra collected from different locations on the discharge product. It can be observed that the ClO$_4$ peak is absent from some of these spectra and there is a stronger MgCl$_2$ peak in some spectra. This leads to conclusion that location-specific measurements are not ideal to identify the discharge product.
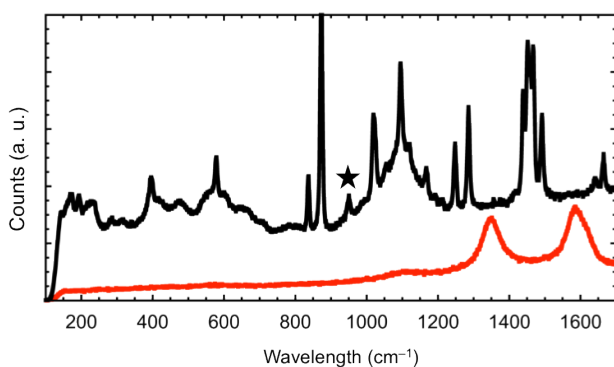
Figure 4.18 Raman spectra collected from control (red) and discharged (black) carbon electrodes. Star symbol indicates the peak for perchlorate vibration.
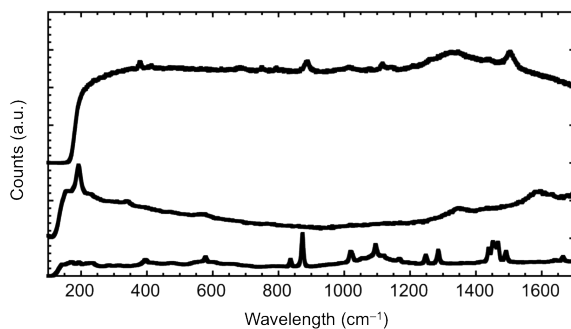
Figure 4.19 Raman spectra collected from discharged carbon electrodes.

Similar to Raman measurements, AES measurements also showed that the discharge product is spatially inhomogeneous. Figure 4.20 shows AES spectra from 4 different locations on the sample. The relative instensities of the Mg, O and Cl peaks change dramatically by changing the data collection spot. Also, the Cl and O peaks are shifted slightly by changing location, indicating that the binding environments change with location as well.
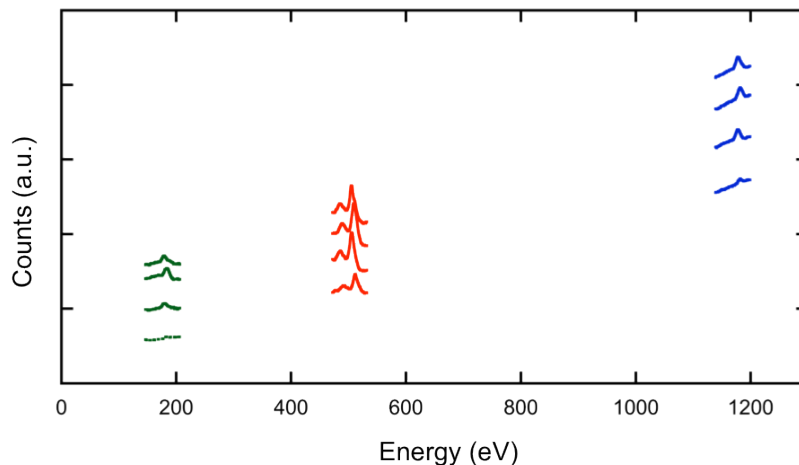
Figure 4.20 AES spectra collected from discharged carbon electrodes in four different locations. Mg (blue), O (red) and Cl (green) spectra are plotted.

Since the AES sample loading exposes the sample to air, we performed sputtering measurements on the sample in conjunction with AES measurements. Figure 4.21 shows the atomic composition of the three elements as a function of depth. The Cl content in this sample is ~9% which is higher than found in the discharge product with PhMgCl:Al(OPh)$_3$/THF electrolyte but significantly lower than expected for a discharge product that consists of MgCl$_2$ and Mg(ClO$_4$)$_2$. The layers closer to surface show an unusually high Mg concentration. In the region that is 20 to 50 nm from the top surface, the Mg and O ratio indicates a MgO layer. Further sputtering (50-80nm) reveals a stronger O signal relative to Mg. Therefore, the discharge product is inhomogeneous in the plane of the cathode as well as along the surface of the cathode.

This inhomogeneity makes it difficult to conclude the chemistry of the discharge product using RS and AES.
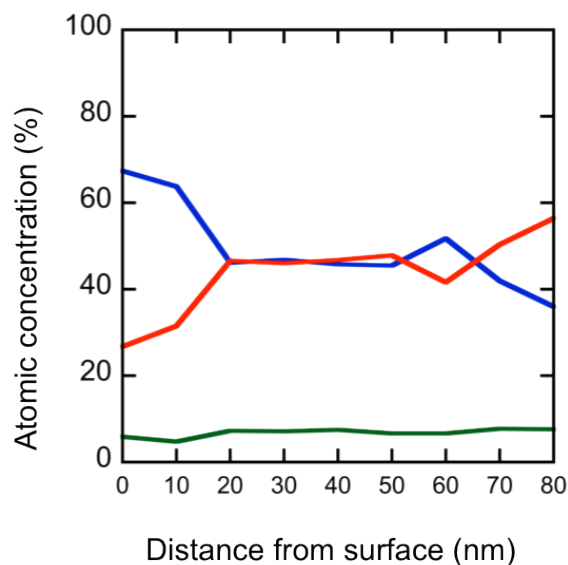
Figure 4.21 AES depth profile of discharge product. Mg (blue), O (red) and Cl (green) atomic concentrations are plotted.

XPS was also employed in order to characterize the discharge product. Figure 4.22 shows the XPS survey spectra that were collected from the sample in 4 different locations. Since the beam size is 1 x 2 mm, peaks attributed to C and F are present because the x-ray beam is sampling the carbon cathode (F is present in the binder of the cathode). C 1s peak was monitored to ensure that there are no charging effects that would result in a shift in the XPS spectra. The inset shows that there are no significant charging effects as evidenced by a stable C1s peak at 284.8 eV. Figure 4.23 shows Mg 2p spectra collected from the sample in 4 different locations. The binding energies for Mg vary significantly depending on the location the data was collected. Mg 2p peak for MgO is found at 49.6 eV,[147-148] whereas $MgCl_2$ introduces peaks at 51.5 eV and 53.0 eV.[149] It was not possible to find data on Mg 2p peak for $Mg(ClO_4)_2$. The variety of higher-

energy peaks that are present in the spectra suggests that Mg has more than two binding environments in the sample and therefore bulk analysis tools such as XRD are most reliable when analyzing the sample.
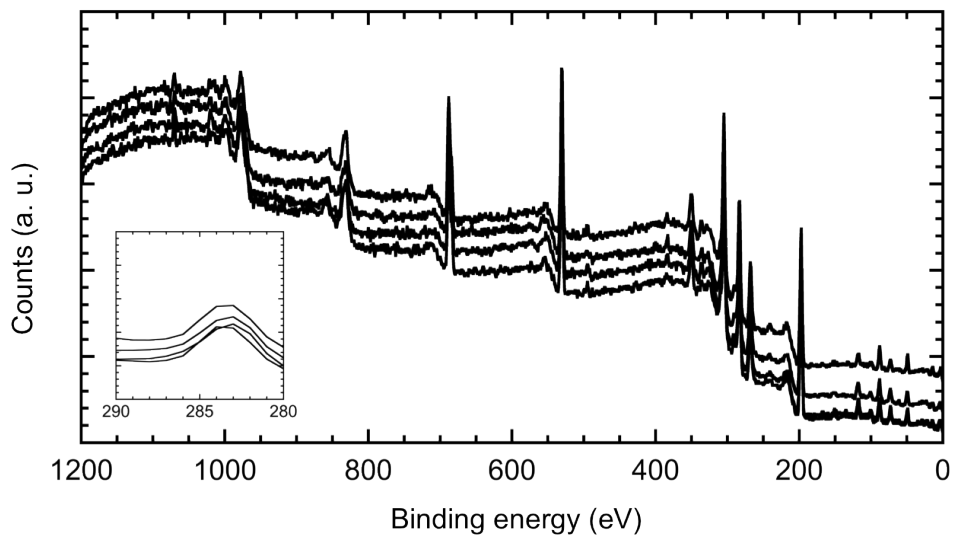
Figure 4.22 XPS spectra of discharged cathode using MACC/DME electrolyte.
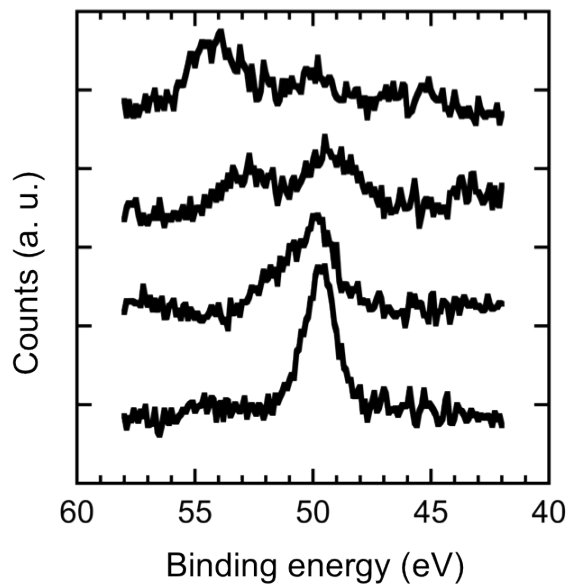
Figure 4.23 Mg 2p XPS spectra of discharged cathode using MACC/DME electrolyte.

4.4 Conclusion

MACC electrolyte in DME solvent is prepared and conditioned by bulk electrolysis. The

conditioned electrolyte shows excellent coulombic efficiency and the conductivity is higher than other reported Mg electrolytes. Mg/O$_2$ cells using conditioned MACC/DME electrolyte exhibit high capacity compared to Mg/O$_2$ cells using previously discussed PhMgCl:Al(OPh)$_3$/THF electrolyte. The observed capacity (for 50 μA/cm^2 discharge rate) is 400 μAh/cm^2, which is comparable to previously reported Mg/O$_2$ cells.[54] The rechargeability of the Mg/O$_2$ cells using MACC/DME electrolyte is limited. EIS measurements show SEI formation on the Mg anode significantly increases Mg/electrolyte interface impedance in the presence of O$_2$. With EIS, we have tracked the formation of the interface associated with discharge product and shown that discharge product formation increases cell impedance considerably. The discharge product is inhomogeneous as deduced from RS, AES, and XPS measurements. XRD measurements suggest formation of Mg(ClO$_4$)$_2$ and MgCl$_2$ on the cathode. It is predicted that Mg(ClO$_4$)$_2$ decomposes into MgCl$_2$. The limited rechargeability of Mg/O$_2$ cells using MACC/DME electrolyte presumably makes this electrolyte an unlikely candidate for future research. Further work is needed to discover electrolytes with low-Cl content. It is also possible to use redox mediators in the electrolyte to promote rechargeability in Mg/O$_2$ cells using MACC/DME electrolyte.

Chapter 5 Conclusions and Next Steps

Widespread electrification of vehicles could lead to a significant reduction of GHG emissions.[5] While Li-ion technology has revolutionized portable electronics, battery chemistries with high energy densities are needed to realize a fully-electric vehicle fleet.[150] In addition to high energy density, it is desirable for next-generation batteries to cost less and have enhanced safety. Mg/O_2 batteries have one of the highest theoretical energy densities.[10] Mg costs less than Li and studies show that Mg metal anodes are less prone to dendrite formation,[13] thus less prone to catastrophic failure of the battery pack. This thesis explores the feasibility of Mg/O_2 batteries as a future energy storage technology.

One of the most challenging aspects of Mg battery development has been the electrolyte[34-35, 74, 151-152], which shuttles Mg^{2+} ions between the cathode and the anode. Ideally the electrolyte should have high ionic conductivity, wide electrochemical window and low flammability and volatility. Ionic liquids satisfy all of these criteria, and for this reason we have used cyclic voltammetry to screen Mg electrolytes in ionic liquid solvents that could potentially be used in a Mg/O_2 battery.[132] Through a systematic screening process, presence of BF_4 and Tf_2N anions were found to inhibit reversible Mg deposition due to the strong attraction between the Mg^{2+} cation and these anions. It was proposed that addition of strong Lewis acids could be utilized to enhance dissociation of Mg from BF_4 and Tf_2N anions and allow for use of ionic liquids in Mg/O_2 batteries.

Although our study of IL-based electrolytes did not identify a promising composition, we subsequently identified and synthesized two electrolytes that enable highly efficient reversible Mg deposition: a modified Grignard reagent electrolyte[53] and an all-inorganic Mg salt electrolyte[135]. We used these two electrolytes in Mg/O_2 cells; Significant differences in Mg/O_2 battery performance were observed based on the electrolyte used.

Mg/O_2 cells using the modified Grignard electrolyte exhibited low capacities ($\sim 10 \mu Ahcm^{-2}$) at a discharge rate of $0.005 mAhcm^{-2}$.[143] The open-circuit voltage was 2.0 V, lower than the ~ 2.9 V expected for direct electrochemical formation of MgO_x. Fair cycling performance was observed up to 3 cycles. The discharge product was identified as a mixture of crystalline MgO and amorphous MgO_2. The low voltage and two-phase product are consistent with a multi-step discharge reaction in which a superoxide-ion (O_2^-) intermediate forms at ~ 2 V vs. Mg/Mg^{2+}. Chemical precipitation and disproportionation subsequently produce MgO_2 and MgO, but do not contribute to the cell's electrical energy output. During charging, MgO_2 decomposes preferentially. Bypassing the multi-step mechanism in favor of direct electrochemical MgO_x formation would raise the discharge potential and, consequently, the energy density.

In contrast to the modified-Grignard-based system, Mg/O_2 cells using MACC/DME electrolyte exhibited very high capacities ($\sim 400 \mu Ahcm^{-2}$ at a discharge rate of $0.05 mAhcm^{-2}$). A wide range of discharge rates were explored to characterize rate performance. The discharge product was identified to be a mixture of $MgCl_2$ and $Mg(ClO_4)_2$. The origins of limited rechargeability was explored using electrochemical impedance spectroscopy. The SEI film forming on the Mg anode in the presence of O_2 and discharge product formation were found to be the main sources of impedance in the Mg/O_2 cell. In Mg/Mg cells held under O_2, the resistance element associated with electrolyte grows faster as a function of time for Grignard

electrolyte when compared to MACC/DME electrolyte, indicating that the MACC/DME electrolyte is more stable in the presence of O_2. It is proposed that addition of redox mediators to the MACC/DME electrolyte could enable a high-capacity *and* rechargeable Mg/O_2 cell.

Major accomplishments of this thesis include: (1) Identification of anions that inhibit reversible Mg deposition/dissolution in IL-based electrolytes, (2) Description for a discharge mechanism explaining the relatively low working potential of an Mg/O_2 battery, (3) Detailed characterization of the Mg/O_2 discharge product for two different types of Mg electrolytes, (4) Confirmation that O_2 exposure can play a large role in the impedance behavior of Mg/O_2 cells.

Unlike in Li-ion batteries, Mg battery technology remains in an early stage of development, and has not yet settled on an optimized electrolyte.[153] Improving the characteristics of the electrolyte by, for example, eliminating corrosive halogens remains an active area of research.[47-48, 50] In order to realize a high-efficiency Mg/O_2 battery that could be a candidate for commercialization, we need to understand the battery performance as a function of different electrolyte compositions and the effects of O_2 on the electrolyte and the electrode/electrolyte interface.[113] While this thesis serves as a starting point for understanding these aspects, several challenges remain.

Rechargeability and round-trip efficiency are common challenges for 'beyond-Li-ion' batteries. Recent developments on metal/O_2 chemistries such as Li/O_2 could provide a path forward for Mg/O_2 battery research in terms of understanding the limitations on rechargeability.[18, 93, 154] For example, a 3-electrode electrochemical cell exposed to O_2 can provide insight into the electrochemical reactions that take place at the separate electrodes and their impact on reversibility.[154] Moreover, the chemical stability of candidate Mg electrolytes in the presence of O_2 can be confirmed with this setup. It is recommended that next phase of Mg/O_2 battery research examine the effect of O_2 exposure on electrolyte stability and delve more deeply

into oxygen interactions with the negative electrode. Furthermore, the addition of metal nanoparticles and modification of the cathode's composition have shown some promise for reducing the charging voltages in Li/O_2 batteries.[18, 155] Similar strategies could be undertaken in Mg/O_2 batteries.

Overall, Mg/O_2 batteries remain at a very early stage of development. Nevertheless, their high theoretical energy densities suggest that further research into improving their rechargeability could pay enourmous dividends. To our knowledge, the present study is the first thesis to examine this system in detail. It is clear that more fundemental research needs to be undertaken to understand the reaction mechanisms as a function of the cell's active and inactive materials. We speculate here that electrolyte development is the most critical aspect to be pursued. If the "right" electrolyte can be engineered, Mg/O_2 batteries could be poised to make exciting contributions to a future energy storage system.

Bibliography

1.   *Annual Energy Review 2011*; US Department of Energy: 2011.

2.   *U.S. Climate Action Report 2014*; US Department of State: 2014.

3.   *Electrification of the Transportation System*; MIT Energy Initiative: 2010.

4.   *2017 and Later Model Year Light-Duty Vehicle Greenhouse Gas Emissions and Corporate Average Fuel Economy Standards*; Environmental Protection Agency: 2012.

5.   *EV Everywhere grand challenge blueprint*; U.S. Department of Energy: 2013.

6.   *Environmental Assessment of Plug-In Hybrid Electric Vehicles*; Electric Power Research Institute: 2007.

7.   Vetter, J.; Novák, P.; Wagner, M. R.; Veit, C.; Möller, K. C.; Besenhard, J. O.; Winter, M.; Wohlfahrt-Mehrens, M.; Vogler, C.; Hammouche, A., Ageing mechanisms in lithium-ion batteries. *Journal of Power Sources* 2005, *147*, 269-281.

8.   Van Noorden, R., A better battery. *Nature* 2014, *507*, 26-28.

9.   *Plug-In Electric Vehicle Handbook for Public Charging*; U.S. Department of Energy: 2012.

10.   Zu, C.-X.; Li, H., Thermodynamic Analysis on Energy Densities of Batteries. *Energy Environ. Sci.* 2011, *4*, 2614-2624.

11.   Rahman, M. A.; Wang, X.; Wen, C., High Energy Density Metal-Air Batteries: A Review. *Journal of the Electrochemical Society* 2013, *160*, A1759-A1771.

12.   Goldstein, J.; Brown, I.; Koretz, B., New developments in the Electric Fuel Ltd . zinc air system. 1999.

13.   Matsui, M., Study on electrochemically deposited Mg metal. *J. Power Sources* 2011, *196*, 7048-7055.

14.   http://www.alibaba.com/ (accessed Dec 15 2015).

15.   Abraham, K. M., A Brief History of Non-aqueous Metal-Air Batteries. *ECS Trans.* 2008, *2008*, 67-71.

16.   Chakkaravarthy, C.; Waheed, A. K. A.; Udupa, H. V. K., Zinc—air alkaline batteries — A review. *Journal of Power Sources* 1981, *6*, 203-228.

17.   Caramia, V.; Bozzini, B., Materials science aspects of zinc–air batteries: a review. *Materials for Renewable and Sustainable Energy* 2014, *3*.

18.   Liu, T.; Leskes, M.; Yu, W.; Moore, A. J.; Zhou, L.; Bayley, P. M.; Kim, G.; Grey, C. P., Cycling Li-O2 batteries via LiOH formation and decomposition. *Science* 2015, *350*, 530-533.

19.   Hamlen, R. P.; Jerabek, E. C.; Ruzzo, J. C.; Siwek, E. G., Anodes for Refuelable Magnesium-Air Batteries. *Journal of The Electrochemical Society* 1969, *116*, 1588.

20.   Sathynarayana, S.; Munichandraiah, N., A New Magnesium-air Cell for Long-life Applications. *J. Appl. Electrochem.* 1981, *11*, 33-39.

21.   Ma, Y.; Li, N.; Li, D.; Zhang, M.; Huang, X., Performance of Mg–14Li–1Al–0.1Ce as Anode for Mg-air battery. *J. Power Sources* 2011, *196*, 2346-2350.

22.   Mayilvel Dinesh, M.; Saminathan, K.; Selvam, M.; Srither, S. R.; Rajendran, V.; Kaler, K. V. I. S., Water Soluble Graphene as Electrolyte Additive in Magnesium-air Battery System. *J. Power Sources* 2015, *276*, 32-38.

23.   Zhang, T.; Tao, Z.; Chen, J., Magnesium–air batteries: from principle to application. *Mater. Horiz.* 2014, *1*, 196-206.

24.   Xu, K., Nonaqueous liquid electrolytes for lithium-based rechargeable batteries. *Chemical Reviews* 2004, *104*, 4303-4417.

25.   Lu, Z.; Schechter, A.; Moshkovich, M.; Aurbach, D., On the electrochemical behavior of magnesium electrodes in polar aprotic electrolyte solutions. *J. Electroanal. Chem.* 1999, *466*, 203-217.

26.   Gregory, T. D.; Hoffman, R. J.; Winterton, R. C., Nonaqueous Electrochemistry of Magnesium. *J. Electrochem. Soc.* 1990, *137*, 775-780.

27.   Novák, P., Electrochemical Insertion of Magnesium in Metal Oxides and Sulfides from Aprotic Electrolytes. *Journal of The Electrochemical Society* 1993, *140*, 140.

28.   Novak, P.; Imhof, R.; Haas, O., Magnesium insertion electrodes for rechargeable nonaqueous batteries — a competitive alternative to lithium? *Electrochemica Acta* 1999, *45*, 351-367.

29.   Lossius, L. P.; Emmenegger, F., Plating Of magnesium from organic solvents_Lossius, Emmenegger. *Electrochemica Acta* 1996, *41*, 445-447.

30.   Liebenow, C., Reversibility of electrochemical magnesium deposition from Grignard solutions. *Journal of Applied Electrochemistry* 1997, *27*, 221-225.

31.   Liebenow, C.; Yang, Z.; Lobitz, P., The electrodeposition of magnesium using solutions of organomagnesium halides , amidomagnesium halides and magnesium organoborates. *Electrochemistry Communications* 2000, *2*, 641-645.

32.   Aurbach, D.; Moshkovich, M.; Schechter, A.; Turgeman, R., Magnesium Deposition and Dissolution Processes in Ethereal Grignard Salt Solutions Using Simultaneous EQCM-EIS and In Situ FTIR Spectroscopy. *Electrochemical and Solid-State Letters* 1999, *3*, 31.

33.   Aurbach, D.; Lu, Z.; Schechter, A.; Gofer, Y.; H., G.; Turgeman, R.; Cohen, Y.; Moshkovich, M.; Levi, E., Prototype systems for rechargeable magnesium batteries. *Nature* 2000, *407*, 724-727.

34.   Aurbach, D.; Schechter, A.; Moshkovich, M.; Cohen, Y., On the Mechanisms of Reversible Magnesium Deposition Processes. *Journal of the Electrochemical Society* 2001, *148*, A1004.

35.   Aurbach, D.; Cohen, Y.; Moshkovich, M., The Study of Reversible Magnesium Deposition by In Situ Scanning Tunneling Microscopy. *Electrochemical and Solid-State Letters* 2001, *4*, A113.

36.   Aurbach, D.; Gizbar, H.; Schechter, A.; Chusid, O.; Gottlieb, H. E.; Gofer, Y.; Goldberg, I., Electrolyte Solutions for Rechargeable Magnesium Batteries Based on Organomagnesium Chloroaluminate Complexes. *J. Electrochem. Soc.* 2002, *149*, A115-A121.

37.   Aurbach, D.; Weissman, I.; Gofer, Y.; Levi, E., Nonaqueous magnesium electrochemistry and its application in secondary batteries. *Chem Rec* 2003, *3*, 61-73.

38.   Viestfrid, Y.; Levi, M. D.; Gofer, Y.; Aurbach, D., Microelectrode studies of reversible Mg deposition in THF solutions containing complexes of alkylaluminum chlorides and dialkylmagnesium. *Journal of Electroanalytical Chemistry* 2005, *576*, 183-195.

39.   Aurbach, D.; Suresh, G. S.; Levi, E.; Mitelman, A.; Mizrahi, O.; Chusid, O.; Brunelli, M., Progress in Rechargeable Magnesium Battery Technology. *Advanced Materials* 2007, *19*, 4260-4267.

40.   Mizrahi, O.; Amir, N.; Pollak, E.; Chusid, O.; Marks, V.; Gottlieb, H.; Larush, L.; Zinigrad, E.; Aurbach, D., Electrolyte Solutions with a Wide Electrochemical Window for Rechargeable Magnesium Batteries. *J. Electrochem. Soc.* 2008, *155*, A103-A109.

41.   Nakayama, Y.; Kudo, Y.; Oki, H.; Yamamoto, K.; Kitajima, Y.; Noda, K., Complex Structures and Electrochemical Properties of Magnesium Electrolytes. *Journal of The Electrochemical Society* 2008, *155*, A754.

42.   Gummow, R. J.; He, Y., Morphology and Preferred Orientation of Pulse Electrodeposited Magnesium. *Journal of the Electrochemical Society* 2010, *157*, E45.

43.   Kim, H. S.; Arthur, T. S.; Allred, G. D.; Zajicek, J.; Newman, J. G.; Rodnyansky, A. E.; Oliver, A. G.; Boggess, W. C.; Muldoon, J., Structure and compatibility of a magnesium electrolyte with a sulphur cathode. *Nat Commun* 2011, *2*, 427.

44.   Zhao-Karger, Z.; Zhao, X.; Fuhr, O.; Fichtner, M., Bisamide based non-nucleophilic electrolytes for rechargeable magnesium batteries. *RSC Adv.* 2013, *3*, 16330-16335.

45.   Guo, Y.-S.; Zhang, F.; Yang, J.; Wang, F.-F.; NuLi, Y.; Hirano, S.-I., Boron-based electrolyte solutions with wide electrochemical windows for rechargeable magnesium batteries. *Energy Environ. Sci.* 2012, *5*, 9100-9106.

46.   Guo, Y.; Zhang, F.; Yang, J.; Wang, F., Electrochemical performance of novel electrolyte solutions based on organoboron magnesium salts. *Electrochemistry Communications* 2012, *18*, 24-27.

47.   Zhu, J.; Guo, Y.; Yang, J.; Nuli, Y.; Zhang, F.; Wang, J.; Hirano, S.-I., Halogen-free boron based electrolyte solution for rechargeable magnesium batteries. *J. Power Sources* 2014, *248*, 690-694.

48.   Mohtadi, R.; Matsui, M.; Arthur, T. S.; Hwang, S. J., Magnesium borohydride: from hydrogen storage to magnesium battery. *Angew. Chem., Int. Ed. Engl.* 2012, *51*, 9780-9783.

49.   Shao, Y.; Liu, T.; Li, G.; Gu, M.; Nie, Z.; Engelhard, M.; Xiao, J.; Lv, D.; Wang, C.; Zhang, J. G.; Liu, J., Coordination chemistry in magnesium battery electrolytes: how ligands affect their performance. *Scientific reports* 2013, *3*, 3130.

50.   Carter, T. J.; Mohtadi, R.; Arthur, T. S.; Mizuno, F.; Zhang, R.; Shirai, S.; Kampf, J. W., Boron clusters as highly stable magnesium-battery electrolytes. *Angew. Chem., Int. Ed. Engl.* 2014, *53*, 3173-3177.

51.   Nelson, E. G.; Kampf, J. W.; Bartlett, B. M., Enhanced oxidative stability of non-Grignard magnesium electrolytes through ligand modification. *Chem Commun (Camb)* 2014, *50*, 5193-5.

52.   Wang, F.-F.; Guo, Y.-S.; Yang, J.; Nuli, Y.; Hirano, S.-I., A novel electrolyte system without a Grignard reagent for rechargeable magnesium batteries. *Chemical communications (Cambridge, England)* 2012, *48*, 10763-5.

53.   Nelson, E. G.; Brody, S. I.; Kampf, J. F.; Bartlett, B. M., A Magnesium Tetraphenylaluminate Battery Electrolyte Exhibits a Wide Electrochemical Potential Window and Reduces Stainless Steel Corrosion. *J. Mater. Chem. A* 2014, *2*, 18194-18198.

54.   Shiga, T.; Hase, Y.; Kato, Y.; Inoue, M.; Takechi, K., A Rechargeable Non-aqueous Mg-O2 Battery. *Chem. Commun. (Camb)* 2013, *49*, 9152-9154.

55.   Shiga, T.; Hase, Y.; Yagi, Y.; Takahashi, N.; Takechi, K., Catalytic Cycle Employing a TEMPO–Anion Complex to Obtain a Secondary Mg–O2Battery. *J. Phys. Chem. Lett.* 2014, *5*, 1648-1652.

56.   MacFarlane, D. R.; Tachikawa, N.; Forsyth, M.; Pringle, J. M.; Howlett, P. C.; Elliott, G. D.; Davis, J. H.; Watanabe, M.; Simon, P.; Angell, C. A., Energy applications of ionic liquids. *Energy Environ. Sci.* 2014, *7*, 232-250.

57.   Kar, M.; Winther-Jensen, B.; Forsyth, M.; MacFarlane, D. R., Chelating ionic liquids for reversible zinc electrochemistry. *Phys Chem Chem Phys* 2013, *15*, 7191-7.

58.   Galiński, M.; Lewandowski, A.; Stępniak, I., Ionic liquids as electrolytes. *Electrochim. Acta* 2006, *51*, 5567-5580.

59.   Armand, M.; Endres, F.; MacFarlane, D. R.; Ohno, H.; Scrosati, B., Ionic-liquid materials for the electrochemical challenges of the future. *Nature materials* 2009, *8*, 621-629.

60.   Ohno, H., *Electrochemical Aspects of Ionic Liquids*. John Wiley & Sons: 2011.

61.   Brennecke, J. F.; Maginn, E. J., Ionic liquids Innovative fluids for chemical processing. *AIChE Journal* 2001, *47*, 2384-2389.

62.   Lewandowski, A.; Świderska-Mocek, A., Ionic liquids as electrolytes for Li-ion batteries—An overview of electrochemical studies. *Journal of Power Sources* 2009, *194*, 601-609.

63.   Ishikawa, M.; Sugimoto, T.; Kikuta, M.; Ishiko, E.; Kono, M., Pure ionic liquid electrolytes compatible with a graphitized carbon negative electrode in rechargeable lithium-ion batteries. *Journal of Power Sources* 2006, *162*, 658-662.

64.   Howlett, P. C.; MacFarlane, D. R.; Hollenkamp, A. F., High Lithium Metal Cycling Efficiency in a Room-Temperature Ionic Liquid. *Electrochemical and Solid-State Letters* 2004, *7*, A97.

65.   Cui, Z. H.; Fan, W. G.; Guo, X. X., Lithium–oxygen cells with ionic-liquid-based electrolytes and vertically aligned carbon nanotube cathodes. *Journal of Power Sources* 2013, *235*, 251-255.

66.   Yan, Y.; Yin, Y.-X.; Xin, S.; Su, J.; Guo, Y.-G.; Wan, L.-J., High-safety lithium-sulfur battery with prelithiated Si/C anode and ionic liquid electrolyte. *Electrochimica Acta* 2013, *91*, 58-61.

67.   Sun, X. G.; Wang, X.; Mayes, R. T.; Dai, S., Lithium-sulfur batteries based on nitrogen-doped carbon and an ionic-liquid electrolyte. *ChemSusChem* 2012, *5*, 2079-85.

68.   Yuan, L. X.; Feng, J. K.; Ai, X. P.; Cao, Y. L.; Chen, S. L.; Yang, H. X., Improved dischargeability and reversibility of sulfur cathode in a novel ionic liquid electrolyte. *Electrochemistry Communications* 2006, *8*, 610-614.

69.   NuLi, Y.; Yang, J.; Wu, R., Reversible deposition and dissolution of magnesium from BMIMBF$_4$ ionic liquid. *Electrochem. Commun.* 2005, *7*, 1105-1110.

70.   NuLi, Y.; Yang, J.; Wang, P., Electrodeposition of magnesium film from BMIMBF$_4$ ionic liquid. *Appl. Surf. Sci.* 2006, *252*, 8086-8090.

71.   Feng, Z.; NuLi, Y.; Wang, J.; Yang, J., Study of Key Factors Influencing Electrochemical Reversibility of Magnesium Deposition and Dissolution. *J. Electrochem. Soc.* 2006, *153*, C689-C693.

72.   NuLi, Y.; Yang, J.; Wang, J.; Xu, J.; Wang, P., Electrochemical Magnesium Deposition and Dissolution with High Efficiency in Ionic Liquid. *Electrochem. Solid-State Lett*. 2005, *8*, C166-C169.

73.   Wang, P.; NuLi, Y.; Yang, J.; Feng, Z., Mixed ionic liquids as electrolyte for reversible deposition and dissolution of magnesium. *Surf. Coat. Technol*. 2006, *201*, 3783-3787.

74.   Amir, N.; Vestfrid, Y.; Chusid, O.; Gofer, Y.; Aurbach, D., Progress in nonaqueous magnesium electrochemistry. *J. Power Sources* 2007, *174*, 1234-1240.

75.   Cheek, G. T.; O'Grady, W. E.; El Abedin, S. Z.; Moustafa, E. M.; Endres, F., Studies on the Electrodeposition of Magnesium in Ionic Liquids. *J. Electrochem. Soc*. 2008, *155*, D91-D95.

76.   Shimamura, O.; Yoshimoto, N.; Matsumoto, M.; Egashia, M.; Morita, M., Electrochemical co-deposition of magnesium with lithium from quaternary ammonium-based ionic liquid. *J. Power Sources* 2011, *196*, 1586-1588.

77.   Muldoon, J.; Bucur, C. B.; Oliver, A. G.; Sugimoto, T.; Matsui, M.; Kim, H. S.; Allred, G. D.; Zajicek, J.; Kotani, Y., Electrolyte roadblocks to a magnesium rechargeable battery. *Energy Environ. Sci*. 2012, *5*, 5941-5950.

78.   Liu, T.; Shao, Y.; Li, G.; Gu, M.; Hu, J.; Xu, S.; Nie, Z.; Chen, X.; Wang, C.; Liu, J., A Facile Approach Using $MgCl_2$ to Formulating High Performance Mg^{2+} Electrolytes for Rechargeable Mg Batteries. *J. Mater. Chem. A* 2013, *2*, 3430-3438.

79.   Yoshimoto, N.; Matsumoto, M.; Egashia, M.; Morita, M., Mixed electrolyte consisting of ethylmagnesiumbromide with ionic liquid for rechargeable magnesium electrode. *J. Power Sources* 2010, *195*, 2096-2098.

80.   Kakibe, T.; Hishii, J.-Y.; Yoshimoto, N.; Egashira, M.; Morita, M., Binary ionic liquid electrolytes containing organo-magnesium complex for rechargeable magnesium batteries. *J. Power Sources* 2012, *203*, 195-200.

81.   Kakibe, T.; Yoshimoto, N.; Egashira, M.; Morita, M., Optimization of cation structure of imidazolium-based ionic liquids as ionic solvents for rechargeable magnesium batteries. *Electrochem. Commun*. 2010, *12*, 1630-1633.

82.   Kitada, A.; Kang, Y.; Uchimoto, Y.; Murase, K., Room-Temperature Electrodeposition of Mg Metal from Amide Salts Dissolved in Glyme-Ionic Liquid Mixture. *J. Electrochem. Soc*. 2013, *161*, D102-D106.

83.   Bonhote, P.; Dias, A.-P.; Papageorgiou, N.; Kalyanasundaram, K.; Gratzel, M., Hydrophobic, Highly Conductive Ambient-Temperature Molten Salts. *Inorg. Chem*. 1996, *35*, 1168-1178.

84.   Zhang, Z.; Gao, X.; Yang, L., Electrochemical properties of room temperature ionic liquids incorporating BF_4^- and $TFSI^-$ anions as green electrolytes. *Chin. Sci. Bull*. 2005, *50*, 2005-2009.

85.   Sakaebe, H.; Matsumoto, H., N-Methyl-N-propylpiperidinium bis(trifluoromethanesulfonyl)imide (PP13–TFSI) – novel electrolyte base for Li battery. *Electrochem. Commun.* 2003, *5*, 594-598.

86.   Tachikawa, N.; Katayama, Y.; Miura, T., Electrode Kinetics of Ferrocenium/ferrocene in Room-temperature Ionic Liquids. *ECS Trans.* 2009.

87.   Sato, T.; Masuda, G.; Takagi, K., Electrochemical properties of novel ionic liquids for electric double layer capacitor applications. *Electrochim. Acta* 2004, *49*, 3603-3611.

88.   *CRC Handbook*. CRC Press: 2011.

89.   Zhao, Q.; NuLi, Y.; Nasiman, T.; Yang, J.; Wang, J., Reversible Deposition and Dissolution of Magnesium from Imidazolium-Based Ionic Liquids. *Int. J. Electrochem.* 2012, *2012*, 1-8.

90.   Forsyth, M.; Neil, W. C.; Howlett, P. C.; Macfarlane, D. R.; Hinton, B. R.; Rocher, N.; Kemp, T. F.; Smith, M. E., New insights into the fundamental chemical nature of ionic liquid film formation on magnesium alloy surfaces. *ACS Appl. Mater. Interfaces* 2009, *1*, 1045-1052.

91.   Giffin, G. A.; Moretti, A.; Jeong, S.; Passerini, S., Complex Nature of Ionic Coordination in Magnesium Ionic Liquid-Based Electrolytes: Solvates with Mobile Mg^{2+} Cations. *J. Phys. Chem. C* 2014, *118*, 9966-9973.

92.   Bakker, A.; Gejji, S.; Lindgren, J.; Hermansson, K.; Probst, M., Contact ion pair formation and ether oxygen coordination in the polymer electrolytes $M[N(CF_3SO_2)_2]_2PEO_n$ for M = Mg, Ca, Sr and Ba. *Polymer* 1995, *36*, 4371-4378.

93.   Peng, Z.; Freunberger, S. A.; Chen, Y.; Bruce, P. G., A Reversible and Higher-rate Li-O2 Battery. *Science* 2012, *337*, 563-566.

94.   Hartmann, P.; Bender, C. L.; Vračar, M.; Dürr, A. K.; Garsuch, A.; Janek, J.; Adelhelm, P., A Rechargeable Room-temperature Sodium Superoxide (NaO2) Battery. *Nat. Mater.* 2013, *12*, 228-232.

95.   Ren, X.; Wu, Y., A Low-overpotential Potassium-oxygen Battery based on Potassium Superoxide. *J. Am. Chem. Soc.* 2013, *135*, 2923-2926.

96.   Bender, C. L.; Hartmann, P.; Vračar, M.; Adelhelm, P.; Janek, J., On the Thermodynamics, the Role of the Carbon Cathode, and the Cycle Life of the Sodium Superoxide (NaO2) Battery. *Adv. Energy Mater.* 2014, *4*, 1301863.

97.   Khoo, T.; Howlett, P. C.; Tsagouria, M.; MacFarlane, D. R.; Forsyth, M., The Potential for Ionic Liquid Electrolytes to Stabilise the Magnesium Interface for Magnesium/air Batteries. *Electrochim. Acta* 2011, *58*, 583-588.

98.   Griffith, L. D.; Sleightholme, A. E.; Mansfield, J. F.; Siegel, D. J.; Monroe, C. W., Correlating Li/O2 Cell Capacity and Product Morphology with Discharge Current. *ACS Appl. Mater. Interfaces* 2015, *7*, 7670-7678.

99.   EL-Cell, Electrochemical test cell ECC-Air User Manual. 2014, *Release 1.7*.

100.   Gonze, X.; Lee, C., Dynamical matrices, Born effective charges, dielectric permittivity tensors, and interatomic force constants from density-functional perturbation theory. *Physical Review B* 1997, *55*, 10355-10368.

101.   Baroni, S.; de Gironcoli, S.; Dal Corso, A.; Giannozzi, P., Phonons and related crystal properties from density-functional perturbation theory. *Reviews of Modern Physics* 2001, *73*, 515-562.

102.   Kresse, G.; Furthmüller, J., Efficiency of ab-initio total energy calculations for metals and semiconductors using a plane-wave basis set *Computational Materials Science* 1996, *6*, 15-50.

103.   Kresse, G.; Hafner, J., Ab initio molecular dynamics for liquid metals. *Physical Review B* 1993, *47*, 558-561.

104.   Kresse, G.; Hafner, J., Ab initio molecular-dynamics simulation of the liquid-metal–amorphous-semiconductor transition in germanium. *Physical Review B* 1994, *49*, 14251-14269.

105.   Kresse, G.; Furthmüller, J., Efficient iterative schemes for ab initio total-energy calculations using a plane-wave basis set. *Physical Review B* 1996, *1996*, 11169-11186.

106.   Perdew, J. P.; Burke, K.; Ernzerhof, M., Generalized Gradient Approximation Made Simple. *Physical Review Letters* 1996, *77*, 3865-3868.

107.   Gajdoš, M.; Hummer, K.; Kresse, G.; Furthmüller, J.; Bechstedt, F., Linear optical properties in the projector-augmented wave methodology. *Physical Review B* 2006, *73*.

108.   Parlinski, K.; Li, Z.; Kawazoe, Y., First-Principles Determination of the Soft Mode in Cubic ZrO 2. *Physical Review Letters* 1997, *78*, 4063-4066.

109.   Parlinski, K., Software Phonon. 2013.

110.   Adams, B. D.; Radtke, C.; Black, R.; Trudeau, M. L.; Zaghib, K.; Nazar, L. F., Current Density Dependence of Peroxide Formation in the Li–O2 Battery and its Effect on Charge. *Energy Environ. Sci.* 2013, *6*, 1772-1778.

111.   Cheng, F.; Chen, J., Metal-air Batteries: From Oxygen Reduction Electrochemistry to Cathode Catalysts. *Chem. Soc. Rev.* 2012, *41*, 2172-2192.

112.   Torres, W.; Mozhzhukhina, N.; Tesio, A. Y.; Calvo, E. J., A Rotating Ring Disk Electrode Study of the Oxygen Reduction Reaction in Lithium Containing Dimethyl Sulfoxide Electrolyte: Role of Superoxide. *J. Electrochem. Soc.* 2014, *161*, A2204-A2209.

113.   Peng, Z.; Freunberger, S. A.; Hardwick, L. J.; Chen, Y.; Giordani, V.; Barde, F.; Novak, P.; Graham, D.; Tarascon, J. M.; Bruce, P. G., Oxygen Reactions in a Non-aqueous Li+ Electrolyte. *Angew. Chem., Int. Ed. Engl.* 2011, *50*, 6351-6355.

114.   Laoire, C. O.; Mukerjee, S.; Abraham, K. M.; Plichta, E. J.; Hendrickson, M. A., Influence of Nonaqueous Solvents on the Electrochemistry of Oxygen in the Rechargeable Lithium−Air Battery. *J. Phys. Chem. C* 2010, *114*, 9178-9186.

115.   Girishkumar, G.; McCloskey, B.; Luntz, A. C.; Swanson, S.; Wilcke, W., Lithium−Air Battery: Promise and Challenges. *J. Phys. Chem. Lett.* 2010, *1*, 2193-2203.

116.   Read, J.; Mutolo, K.; Ervin, M.; Behl, W.; Wolfenstine, J.; Driedger, A.; Foster, D., Oxygen Transport Properties of Organic Electrolytes and Performance of Lithium/Oxygen Battery. *J. Electrochem. Soc.* 2003, *150*, A1351-A1356.

117.   Lu, Y.-C.; Kwabi, D. G.; Yao, K. P. C.; Harding, J. R.; Zhou, J.; Zuin, L.; Shao-Horn, Y., The discharge rate capability of rechargeable Li–O2 batteries. *Energy & Environmental Science* 2011, *4*, 2999-3007.

118.   Quaranta, M.; Murkovic, M.; Klimant, I., A new method to measure oxygen solubility in organic solvents through optical oxygen sensing. *The Analyst* 2013, *138*, 6243-6245.

119.   Gizbar, H.; Vestfrid, Y.; Chusid, O.; Gofer, Y.; Gottlieb, H. E.; Marks, V.; Aurbach, D., Alkyl group transmetalation reactions in electrolytic solutions studied by multinuclear NMR. *Organometallics* 2004, *23*, 3826-3831.

120.   Park, M.; Zhang, X.; Chung, M.; Less, G. B.; Sastry, A. M., A review of conduction phenomena in Li-ion batteries. *Journal of Power Sources* 2010, *195*, 7904-7929.

121.   Zhang, S. S.; Foster, D.; Read, J., Discharge Characteristic of a Non-aqueous Electrolyte Li/O2 Battery. *J. Power Sources* 2010, *195*, 1235-1240.

122.   Seyama, H.; Soma, M., X-ray Photoelectron Spectroscopic Study of Montmorillonite Containing Exchangeable Divalent Cations. *J. Chem. Soc., Faraday Trans. 1* 1984, *80*, 237-248.

123.   Hallstedt, B., The Magnesium-Oxygen system. *Calphad* 1993, *17*, 281-286.

124.   Duffy, T. S.; Meade, C.; Fei, Y.; Mao, H.-k.; Hemley, R. J., High-pressure phase transition in brucite, Mg(OH)2. *American Minerologist* 1995, *80*, 222-230.

125.   Pour, N.; Gofer, Y.; Major, D. T.; Aurbach, D., Structural analysis of electrolyte solutions for rechargeable Mg batteries by stereoscopic means and DFT calculations. *Journal of the American Chemical Society* 2011, *133*, 6270-6278.

126.   Vestfried, Y.; Chusid, O.; Goffer, Y.; Aped, P.; Aurbach, D., Structural Analysis of Electrolyte Solutions Comprising Magnesium−Aluminate Chloro−Organic Complexes by Raman Spectroscopy. *Organometallics* 2007, *26*, 3130-3137.

127.   de Waal, D.; Range, K.-J.; Königstein, M.; Kiefer, W., Raman Spectra of the Barium Oxide Peroxide and Strontium Oxide Peroxide Series. *J. Raman Spectrosc.* 1998, *29*, 109-113.

128.   Born, M.; Huang, K., Dynamical Theory of Crystal Lattices. *Oxford Press* 1954, 367-373.

129.   Yagi, S.; Tanaka, A.; Ichikawa, Y.; Ichitsubo, T.; Matsubara, E., Electrochemical Stability of Magnesium Battery Current Collectors in a Grignard Reagent-Based Electrolyte. *Journal of the Electrochemical Society* 2013, *160*, C83-C88.

130.   Guo, Y.; Yang, J.; NuLi, Y.; Wang, J., Study of electronic effect of Grignard reagents on their electrochemical behavior. *Electrochemistry Communications* 2010, *12*, 1671-1673.

131.   Cooper, C., *Organic Chemist's Desk Reference*. 2nd ed.; Chapman and Hall/CRC: 2010.

132.   Vardar, G.; Sleightholme, A. E.; Naruse, J.; Hiramatsu, H.; Siegel, D. J.; Monroe, C. W., Electrochemistry of magnesium electrolytes in ionic liquids for secondary batteries. *ACS applied materials & interfaces* 2014, *6*, 18033-9.

133.   Lapidus, S. H.; Rajput, N. N.; Qu, X.; Chapman, K. W.; Persson, K. a.; Chupas, P. J., Solvation structure and energetics of electrolytes for multivalent energy storage. *Physical chemistry chemical physics : PCCP* 2014, *16*, 21941-5.

134.   Rajput, N. N.; Qu, X.; Sa, N.; Burrell, A. K.; Persson, K. A., The coupling between stability and ion pair formation in magnesium electrolytes from first-principles quantum mechanics and classical molecular dynamics. *Journal of the American Chemical Society* 2015, *137*, 3411-20.

135.   Doe, R. E.; Han, R.; Hwang, J.; Gmitter, A. J.; Shterenberg, I.; Yoo, H. D.; Pour, N.; Aurbach, D., Novel, electrolyte solutions comprising fully inorganic salts with high anodic stability for rechargeable magnesium batteries. *Chem Commun (Camb)* 2014, *50*, 243-5.

136.   Barile, C. J.; Barile, E. C.; Zavadil, K. R.; Nuzzo, R. G.; Gewirth, A. A., Electrolytic Conditioning of a Magnesium Aluminum Chloride Complex for Reversible Magnesium Deposition. *The Journal of Physical Chemistry C* 2014, *118*, 27623-27630.

137.   See, K. A.; Chapman, K. W.; Zhu, L.; Wiaderek, K. M.; Borkiewicz, O. J.; Barile, C. J.; Chupas, P. J.; Gewirth, A. A., The Interplay of Al and Mg Speciation in Advanced Mg Battery Electrolyte Solutions. *Journal of the American Chemical Society* 2015.

138.   Canepa, P.; Jayaraman, S.; Cheng, L.; Rajput, N. N.; Richards, W. D.; Gautam, G. S.; Curtiss, L. A.; Persson, K. A.; Ceder, G., Elucidating the structure of the magnesium aluminum chloride complex electrolyte for magnesium-ion batteries. *Energy Environ. Sci.* 2015, *8*, 3718-3730.

139.   Zhao-Karger, Z.; Mueller, J. E.; Zhao, X.; Fuhr, O.; Jacob, T.; Fichtner, M., Novel transmetalation reaction for electrolyte synthesis for rechargeable magnesium batteries. *RSC Adv.* 2014, *4*, 26924-26927.

140.   Liao, C.; Sa, N.; Key, B.; Burrell, A. K.; Cheng, L.; Curtiss, L. a.; Vaughey, J.; Hu, L.; Pan, B.; Zhang, Z.; Woo, J.-J., The Unexpected Discovery of Mg(HMDS)2MgCl2 Complex as Magnesium Electrolyte for Rechargeable Magnesium Batteries. *J. Mater. Chem. A* 2015, *3*, 6082-6087.

141.   Shterenberg, I.; Salama, M.; Yoo, H. D.; Gofer, Y.; Park, J.-B.; Sun, Y.-K.; Aurbach, D., Evaluation of (CF3SO2)2N–(TFSI) Based Electrolyte Solutions for Mg Batteries. *Journal of the Electrochemical Society* 2015, *162*, A7118-A7128.

142.   Barile, C. J.; Nuzzo, R. G.; Gewirth, A. A., Exploring Salt and Solvent Effects in Chloride-Based Electrolytes for Magnesium Electrodeposition and Dissolution. *The Journal of Physical Chemistry C* 2015, *119*, 13524-13534.

143.   Vardar, G.; Nelson, E. G.; Smith, J. G.; Naruse, J.; Hiramatsu, H.; Bartlett, B. M.; Sleightholme, A. E. S.; Siegel, D. J.; Monroe, C. W., Identifying the Discharge Product and Reaction Pathway for a Secondary Mg/O2Battery. *Chemistry of Materials* 2015, *27*, 7564-7568.

144.   Huggins, R. A., Simple Method to Determine Electronic and Ionic Components of the Conductivity in Mixed Conductors A Review. *Ionics* 2002, *8*, 300-313.

145.   Irvine, J. T. S.; Sinclair, D. C.; West, A. R., Electroceramics Characterization by Impedance Spectroscopy. *Advanced Materials* 1990, *2*, 132-138.

146.   Stern, K. H., High Temperature Properties and Decomposition of Inorganic Salts, Part 4. Oxy-Salts of the Halogens. *Journal of Physical and Chemical Reference Data* 1974, *3*, 481-526.

147.   Corneille, J. S.; He, J.-W.; Goodman, D. W., XPS characterization of ultra-thin MgO films on a Mo (100) surface. *Surf. Sci.* 1994, *306*, 269-278.

148.   Ardizzone, S.; Bianchi, C. L.; Fadoni, M.; Vercelli, B., Magnesium salts and oxide an XPS overview. *Applied Surface Science* 1997, *119*, 253-259.

149.   Siokou, A.; Kefalas, D.; Ntais, S., XPS study of hydrated MgCl2 impregnated on flat SiO2/Si(100) Mo and Au substrates. *Surface Science* 2003, *532-535*, 472-477.

150.   Evarts, E. C., Lithium batteries: To the limits of lithium. *Nature* 2015, *526*, S93-S95.

151.   Aurbach, D.; Markovsky, B.; D., L. M.; E., L.; Schechter, A.; Moshkovich, M.; Cohen, Y., New insights into the interactions between electrode materials and electrolyte solutions for advanced nonaqueous batteries. *Journal of Power Sources* 1999, *81-82*, 95-111.

152.   Aurbach, D.; Pour, N., Non-aqueous electrochemistry of magnesium (Mg). In *Corrosion of Magnesium Alloys*, Woodhead Publishing: 2011, pp 484-515.

153.   Aurbach, D.; Gofer, Y.; Schechter, A.; Chusid, O.; Gizbar, H.; Cohen, Y.; Moshkovich, M.; Turgeman, R., A comparison between the electrochemical behavior of reversible magnesium and lithium electrodes. *J. Power Sources* 2001, *97-98*, 269-273.

154.   Johnson, L.; Li, C.; Liu, Z.; Chen, Y.; Freunberger, S. a.; Tarascon, J.-M.; Ashok, P. C.; Praveen, B. B.; Dholakia, K.; Bruce, P. G., The Role of LiO2 Solubility in O2 Reduction in Aprotic Solvents and its Consequences for Li–O2 Batteries. *Nat. Chem.* 2014, *6*, 1091-1099.

155.   Lu, J.; Lee, Y. J.; Luo, X.; Lau, K. C.; Asadi, M.; Wang, H. H.; Brombosz, S.; Wen, J.; Zhai, D.; Chen, Z.; Miller, D. J.; Jeong, Y. S.; Park, J. B.; Fang, Z. Z.; Kumar, B.; Salehi-Khojin,

A.; Sun, Y. K.; Curtiss, L. A.; Amine, K., A lithium-oxygen battery based on lithium superoxide. *Nature* 2016, *529*, 377-82.